POLITECNICO DI MILANO
Dottorato di Ricerca in Bioingegneria
Ph.D. in Bioengineering

Alessio Meoli

A multiscale model of cardiac biomechanics to simulate surgical procedures in patients affected by hypoplastic heart syndrome

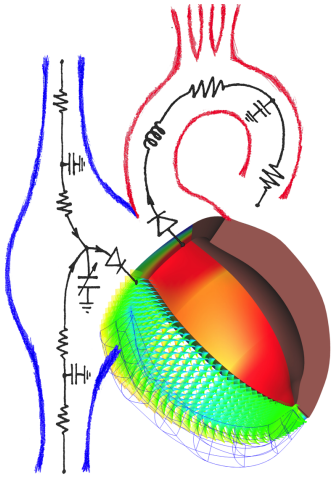

POLITECNICO DI MILANO
Dottorato di Ricerca in Bioingegneria
Ph.D. in Bioengineering

A multiscale model of cardiac biomechanics to simulate surgical procedures in patients affected by hypoplastic heart syndrome

Alessio Meoli

Supervisor:
Prof. Giancarlo Pennati

PhD Coordinator:
Prof. Andrea Aliverti

Advisor:
Prof. Francesco Migliavacca

XXVII Cycle
March 2015

"*Learn from yesterday, live for today, hope for tomorrow. The important thing is not to stop questioning.*"

Albert Einstein

Acknowledgements

First, I would like to express my sincere gratitude to my supervisor Prof. Giancarlo Pennati. Thank you for guiding my work in the last three years and a half, your exceptional scientific and technical expertise was fundamental to me in successfully developing my research skills. Thank you also for the trust you have always demonstrated in me.
I wish to acknowledge Prof. Francesco Migliavacca, director of the LaBS, where I spent my PhD, my work would not have been possible without the opportunity you gave to me. Thank you for the constant support and collaboration and to made possible my exchange period. I would like also to thank all the other professors and researchers working at LaBS for the shared knowledge and useful comments.
I am grateful to Fondation Leducq, Paris, for granting this work within the Transatlantic Networks of Excellence in Cardiovascular Research Program. The collaborative research risen from this project was challenging and exciting at the same time. A special thank goes to Prof. Alison Marsden who accepted me in his laboratory at UCSD where I lived an unforgettable experience.
I would like to thank Adarsh Krishnamurthy and Jeff Van Dorn from the Cardiac Mechanics Research Group at the UCSD, thank you for helping me with Continuity 6.4, for sharing your competencies and your precious scripts, this work would not have been fully complete without your support.
I would like to thank all the present and past students of LaBS for their sympathy and friendship and for sharing the good as well as the bad moments. Thank you for all the coffees, lunches, beers and most important for making LaBS a second home, I will never forget you.
A very huge thank goes to my family, Franco, Adele and my sister Deborah who support me during these years with love and encouragement. I thank all my Friends from Lecco, where I live, who brighten my life and are always present when I need. Lastly, but most importantly, I would like to thank Sara, an amazing woman who shared with me almost all my adult life, thank you for always supporting me, being inspiring and pushing me to obtain my best...Thank you!!

Alessio

Abstract

Single-ventricle (SV) defect is a complex congenital heart disease not compatible with life that could affect the left or the right ventricle with different grade of hypoplasia. Commonly, it is treated following a three-stage surgical procedure with the goal of restoring, in the last stage, a series of the systemic and pulmonary circulations. In the last decades great improvements in the surgical procedures have been achieved with significant increase in the outcomes for the treatment of SV defects. However, univentricular circulation still represents a critical and peculiar condition. Moreover, among different specialized centers a significant variation in the surgical options is still present and related to the expertise of the surgeons.

This study aims at developing a multiscale computational framework able to couple a patient-specific 3D finite-element (FE) model of the SV to a patient-specific lumped parameter (LP) model of the whole circulation, in a closed-loop fashion. A sequential approach was carried out: (i) cardiocirculatory parameters were estimated by using a fully LP model; (ii) ventricular material parameters and unloaded geometry were identified by means of the stand-alone, 3D model of the SV; and (iii) the 3D model of SV was coupled to the LP model of the circulation, thus closing the loop and creating a multiscale model. Once the patient-specific multiscale model was setup using pre-operative clinical data, virtual surgery was performed thus, the post-operative condition was simulated. This approach allows the analysis of local information on ventricular function as well as global parameters of the cardiovascular system. In this work two patient-specific cases were simulated demonstrating the goodness of the proposed methodology in simulating the macroscopic behaviour of each patient considered. The pre-operative state of the patients were successfully simulated with errors in replicating the main hemodynamic quantities lower then 5%. The regional myocardial results reported were in agreement with other FE works and showed that SV hearts are subjected to heavier working conditions in respect to normal heart. The simulation of the post-operative state showed that: i) stroke volume significantly decreases (about 20-40$\%$ depending on the considered patient); ii) the EDV decreases confirming the beneficial effect of the surgery; iii) aortic pressure increases in the mean value; iv) each patient presents specific response to the surgical procedure confirming the need for patient-specific modelling. To test the ability of the model in simulating SV circulation also in condition different form the clinical one, active condition and influence of fibre orientations were successfully simulated.

Glossary of Acronyms

0D	Zero-dimensional
3D	Three-dimensional
BDG	Bidirectional Glenn
BSA	Body surface area
BCPC	Bidirectional cavopulmonary connection
BT	Blalock-Taussig
CFD	Computational fluid dynamics
CHD	Congenital heart disease
CMR	Caridac magnetic resonance
CO	Cardiac output
CT	Computer tomography
ECG	Electrocardiogram
ED	End diastolic
EDV	End diastolic volume
ES	End systolic
FE	Finite element
FEM	Finite element method
FSI	Fluid-structure interaction
HFP	Hemi-Fontan procedure
HHS	Hypoplastic heart syndrome
HLHS	Hypoplastic left heart syndrome
HRHS	Hypoplastic right heart syndrome
LBSVR	Lower body systemic vascular resistances
LP	Lumped parameter
LPVR	Left pulmonary vascular resistances
LV	Left ventricle
MR	Magnetic resonance
MRI	Magnetic resonance images
PVL	Pressure volume loop

PVR	Pulmonary vascular resistance
RPVR	Right pulmonary vascular resistances
RV	Right ventricle
SA	Single atrium
SL	Sarcomere lenght
SV	Single ventricle
SVC	Superior vena cava
TCPC	Total cavopulmonary connection
UBSVR	Upper body systemic vascular resistances

Contents

Chapter 1

Hypoplastic heart syndrome: surgical and modelling considerations

Hypoplastic heart syndrome is a congenital heart disease that implies the absence or the underdevelopment of one ventricular chamber. This condition is invariably fatal during the first days of life, and normally is treated by consecutive palliative surgical procedures. In this chapter a brief introduction on the hypoplastic heart syndrome is reported highlighting the differences between the normal and the single ventricle circulations and describing the possible surgical procedures. Also a review of the modelling approaches used to study the univentricular circulation present in literature is described.

1.1 Hypoplastic heart syndrome

THE hypoplastic heart syndrome (HHS) is a complex congenital heart disease characterized by a variable degree of underdevelopment of one of the two ventricular chambers. The hypoplastic left heart syndrome (HLHS, Figure 1.1) is more common than the hypoplastic right heart syndrome (HRHS) with a reported incidence of HLHS ranges from 0.16 to 0.36 per 1000 live births with a male predominance (Clausen, 2015).

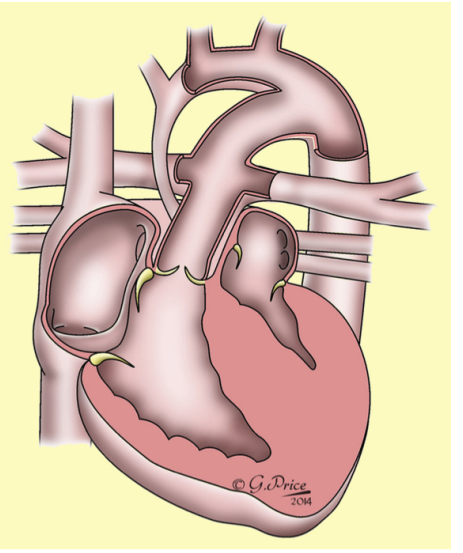

Figure 1.1 Four chamber view of an hypoplastic left heart. The left-sided heart structures are clearly hypoplastic and the arterial duct is maintained patent to sustain life in the immediate postnatal period [Reprinted from (Clausen, 2015) with permission by Elsevier].

As a consequence of the HHS, depending on which sides of the heart is interested by the pathology, also the related heart structures (left or right) are underdeveloped. The degree of underdevelopment differs from child to child and affect the ascending aorta, the mitral and the aortic valves in case of HLHS while the pulmonary artery, the tricuspid and the pulmonary valves in case of HRHS. In both cases, in the fetus the systemic and the pulmonary blood flow are fully, or mostly, provided by the only functional ventricle. This is possible because the ductus arteriosus is open allowing blood to continue flowing into both

systemic and pulmonary circulations simultaneously. As a consequence, the fetus is generally well and unaffected by the anatomical abnormality. However, with the natural changes from the fetal to the newborn physiology (i.e. closure of the ductus arteriosus and PVR falls) the HHS is invariably fatal within the first few weeks of life without intervention. Immediate management (few days prior the intervention) requires pharmacological maintenance of ductal patency as well as manipulation of patient ventilation to control pulmonary vascular resistance. Hence, the systemic and pulmonary circulations are in parallel, not in series as in the physiological condition.

At certain centers, cardiac transplantation may be the preferred choice. The transplant is advantageous since it is more physiologic than the palliative treatment and it is a single operation (Alsoufi et al., 2007; Bailey et al., 1986). However, several disadvantages are associated with transplant, including limited availability, need for immunosuppressive therapy and possible retransplantation due to rejection, making this a viable option only for a few number of patients.

Single ventricle (SV) defects is most commonly managed using a three-stage surgical repair, called the Fontan procedure (Khairy et al., 2007; Muthurangu et al., 2005). The goal of the surgical treatment is to obtain separated pulmonary and systemic circulations, thus restoring a physiological-like state (Figure 1.2). However, at birth the lungs are immature and the pulmonary vascular resistances(PVR) is naturally high, precluding a series circulation in the neonatal period (Norwood, 1991). Thus, multi-stage management is necessary. The technique involves subsequent changes in the circulatory layout, up to a final configuration where the venous return passively flows into the lungs without the need for a pumping chamber, and the functional SV provides the systemic blood flow (Algra et al., 2011; De Leval and Deanfield, 2010). Despite the current surgical strategies still remain palliative, recents improvements in the surgical treatment have increased the life expectations obtained in children with these malformation (Bardo et al., 2001).

1.2 The Fontan procedure

The Fontan procedure consists of three open heart surgeries to force the only functional ventricle to do the work normally done by the two ventricles. The goal of the surgeries is to obtain separate venous and systemic circulations. Since the PVR is subjected to significant changes over the first years of life, the surgery must be performed in subsequent stages. A successful Fontan procedure requires a sufficient drop in the PVR allowing the venous blood to

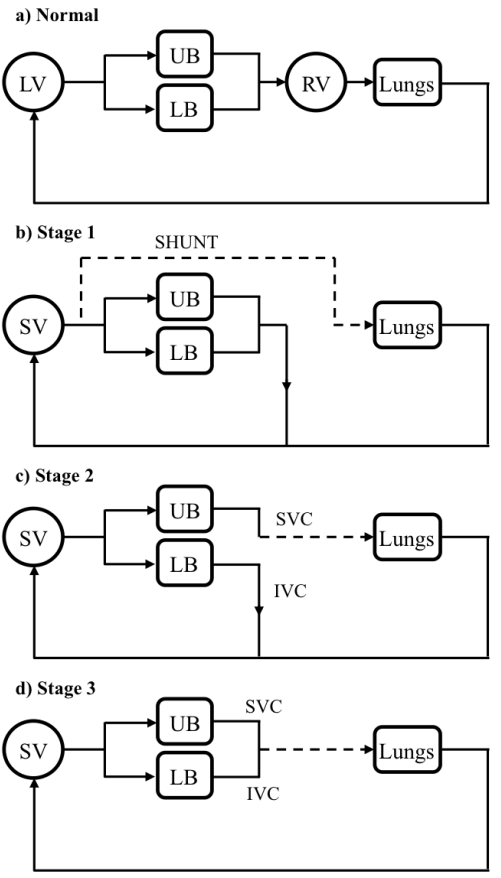

Figure 1.2 Sketches of the normal (a) and the pathological circulations (b-d). (b) parallel Norwood circulation (stage 1), with the interposition of a systemic-to-pulmonary shunt to deliver blood to the lungs; (c) stage 2 circulation with the upper systemic and pulmonary circulations in series; and (d) stage 3 Fontan circulation, with the systemic and pulmonary circulations in series. LB, lower body; LV, left ventricle; RV, right ventricle; SV, single ventricle; SVC, superior vena cava; IVC, inferior vena cava. UB, upper body.

passively flows into the lungs without the aid of a pumping chamber (as in the normal circulation). This change is not achievable during the first months of life, therefore two stages must be performed until the lungs are matured.

The Norwood procedure is the first stage employed in the surgical palliation of SV patients (Norwood et al., 1980, 1983). This procedure is usually performed during the very first days of life (Gaca et al., 2008; Khairy et al., 2007; Muthurangu et al., 2005). Figure 1.3 shows the procedure for a case of HLHS. The goals of the first stage of the Norwood procedure are: to establish a permanent, unobstructed connection between the right ventricle and the systemic arterial circulation; to ensure unobstructed pulmonary venous return with a satisfactory interatrial communication (atrial septectomy); and to provide stable but limited pulmonary blood flow via a systemic-to-pulmonary shunt. Hence, the main pulmonary artery is ligated and a portion is anastomosed to the aortic arch in order to create a neoaorta that can be augmented with a patch if required. A systemic-to-pulmonary shunt is inserted to provide blood flow to the lungs. Atrial sepetectomy is performed to allow systemic and pulmonary venous blood to flow via the right atrium (RA) into the right ventricle (RV) and out into the neo-aortic arch. As a result of the surgery, the SV provides a means of blood oxygenation through a system of parallel pulmonary and systemic circulations (Figure 1.2 b). In case of HRHS, the main goal of the surgical procedure is identical with the difference that the left structures of the heart are normally developed, hence the aortic arch reconstruction is not required. The hypoplastic pulmonary artery is ligated, a systemic-to-pulmonary shunt is inserted and atrial sepetectomy is performed to allow mixing of the systemic and pulmonary venous blood thus recreating the same condition as in the HLHS case (Figure 1.2 b).

Different options are currently available to deliver blood flow trough the systemic-to-pulmonary shunt to the pulmonary circulation (Clausen, 2015). These include the modified Blalock-Taussig (BT) shunt connecting the innominate artery to the right pulmonary artery (Yuan et al., 2009), the Central shunt connecting the ascending aorta to the pulmonary arteries (Alboliras et al., 1989) and the Sano modification, consisting in a right ventriculotomy with placement of a right ventricle-to-pulmonary artery valveless conduit (Sano et al., 2003). As a temporary alternative to the classic Norwood or Sano procedures, the so called 'hybrid approach' has been recently introduced. This technique involves a less invasive procedure combining the placement of a stent in the ductus arteriosus to maintain systemic perfusion and the banding of brunch pulmonary artery to limit pulmonary blood flow while promoting unobstructed pulmonary venous return (Galantowicz et al., 2008). This approach has been particularly favoured for babies presenting borderline hypoplasia of the left heart, to enable potential growth of these structures in early infancy with the aim of a biventricular repair rather than univentricular palliation (Clausen, 2015).

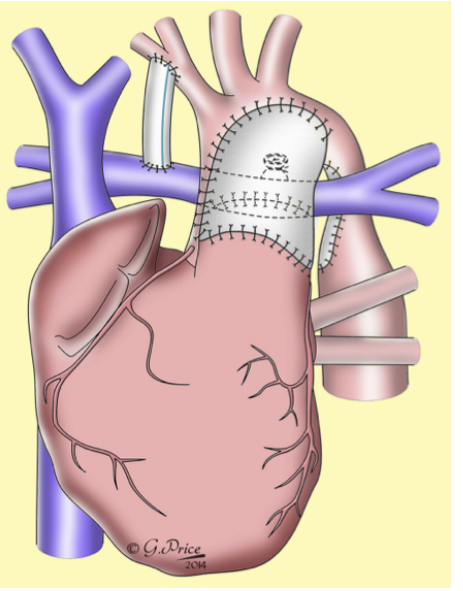

Figure 1.3 The Norwood procedure in case of HLHS. The pulmonary valve is disconnected from the pulmonary trunk and anastomosed to the proximal ascending aorta. The hypoplastic arch is augmented along its course and a modified Blalock-Taussig shunt fashioned to supply pulmonary blood supply. The arterial duct is ligated and the atrial septum resected where necessary to allow non-restrictive pulmonary venous blood flow to the right atrium. [Reprinted from (Clausen, 2015) with permission by Elsevier].

The second palliative stage (Figure 1.4) is usually performed between the third and ninth months of life, after PVR has decreased to normal levels and the SVC is large enough to provide adequate pulmonary blood flow. The goal at this stage is to begin to separate the systemic and pulmonary circulations. The surgical technique involves the redirection of the upper portion of the systemic venous return to the lungs bypassing the SV thus and resulting in the upper body (UB) systemic circulation being in series with the pulmonary circulation (Figure 1.2 c). This results in a decreased volume load on the single ventricle, thus helping to relieve ventricular overload occurred in the first stage circulation and in an increase of the total impedance seen by the SV.

Two surgical techniques are commonly utilized to perform the second stage: the hemi-Fontan procedure (HFP) and the bidirectional Glenn shunt (BDG). Both strategies implies the creation of a superior bidirectional cavopulmonary

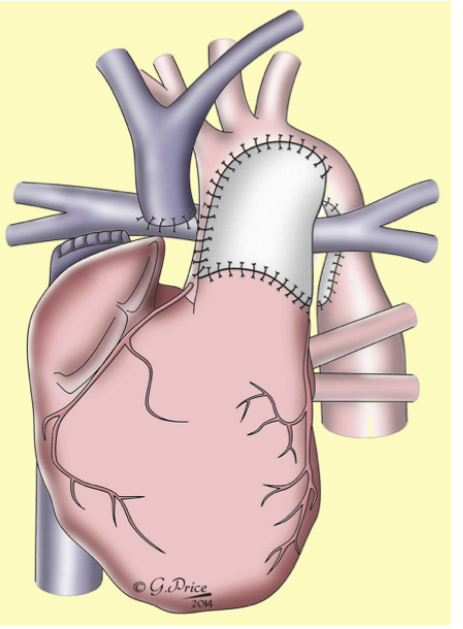

Figure 1.4 The Glenn procedure. The SVC is disconnected from the RA and anastomosed to to the central right pulmonary artery replacing the previously placed shunt [Reprinted from (Clausen, 2015) with permission by Elsevier].

connection (BCPC) in which the superior vena cava (SVC) is connected to the pulmonary arteries by means of an anastomosis. In the BDG procedure the SVC is connected to the right pulmonary artery, while in the HFP the SVC remains connected to the RA with a homograft patch redirecting its flow to the pulmonary arteries (Alsoufi et al., 2007; Dillman et al., 2010; Gaca et al., 2008). Finally, the systemic-to-pulmonary shunt is ligated.

The third and final surgical stage known as the Fontan operation (Figure 1.5) is usually performed between 18 and 48 months of life and represents the common endpoint for patient affected by SV defects (Alsoufi et al., 2007; Clausen, 2015; Khairy et al., 2007). The goal of the surgery is to complete the separation of the pulmonary and systemic circulations, thus placing the circulations back in series. In this stage a total cavopulmonary connection (TCPC) is created connecting the inferior vena cava (IVC) to the right pulmonary artery by means of either an intra-atrial or an extra cardiac conduit, thus bypassing the single func-

tional ventricle (Clausen, 2015; Gaca et al., 2008). As a results of the TCPC, all the systemic venous blood flow passively returns to the lungs without any direct ventricular assistance. This procedure allows for complete separation of the poorly oxygenated systemic venous blood from the highly oxygenated systemic arterial blood, thus alleviating cyanosis and ventricular volume overload (Bardo et al., 2001). Hence, the final univentricular configuration (Figure 1.2 d) restores the normal serial circulation occurring in normal subjects, where the heart pumps blood to the pulmonary and systemic districts in sequence by means of the two functional ventricles (Figure 1.2 a).

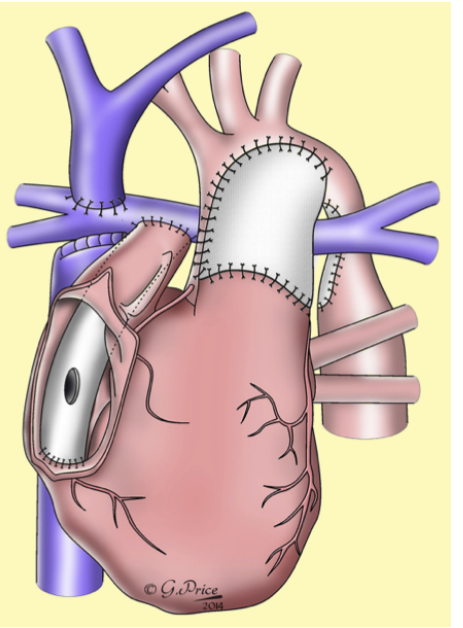

Figure 1.5 The Fontan circulation. The IVC is disconnected from the right atrium and reconnected with the central right pulmonary artery via an artificial vessel. The cavopulmonary connection may have an additional small fenestration, which acts as a pop-off valve by allowing blood to flow back to the heart before reaching the pulmonary circulation. This may be advantageous in the setting of temporarily elevated PVR and patients will have slightly lower than normal saturations as a consequence. The fenestration can later be closed interventionally with an atrial septal defect occluding device if necessary [Reprinted from (Clausen, 2015) with permission by Elsevier].

1.3 Modelling approaches to study SV circulation

Despite improvements in the surgical techniques have dramatically increased the outcomes for the treatment of SV defects, univentricular circulation represents a very critical and peculiar condition. Moreover, although the 3-stage treatment approach is now well founded, significant differences in the surgical options and among different specialized centers are still present. For this reason in the last decades, with the goal of an in-depth understanding of SV physiology, various engineering approach have been used to study the hemodynamics occuring in these patients. Depending on the purpose of the study, different models have been proposed which can be categorized into three main groups: experimental (*in vitro* set-ups), analytical (purely mathematical models), and computational (*in silico* simulations). The state of the art on experimental and analytical models applied to congenital heart diseases will not be illustrated in detail in the present work, instead more attention will be placed on the description of computational models applied on SV patients.

In general, the experimental approach can be of particular interest to test the efficiency of medical devices (Huber et al., 2004) or to produce reproducible data that can be useful for the validation of computatonal models (Babuska and Oden, 2004). The models usually consist of mock circulatory loop with a variable level of complexity depending on the objectives of the study. They range from very simple rigs with lumped resistive and compliant elements to full circulatory mock loops with all main vascular components including also some anatomical realistic elements.

In the contest of the SV circulation, different *in vitro* set-ups have been proposed to investigate the effect of variables that impact the hemodynamics at different stages of the treatment. In one experimental study focused on the Norwood circulation (Tacy et al., 1998), a range of BT shunt lengths and diameters have been tested to verify the relation between Doppler-predicted pressure gradient and pressure gradient measured in actual Gore-Tex® shunts placed in a circuit composed by a pulsatile flow generator and parallel systemic and pulmonary vasculatures. Another *in vitro* study (Dur et al., 2009) focused on the Fontan circulation evaluating the feasibility of supporting cardiopulmonary flow by means of different ventricular assistance devices. The adopted mock loop, showed in Figure 1.6, is composed by six different compartments including the venous and the systemic circulation and giving the possibility to account for anatomical model of the TCPC site.

The analytical approach implies the use of mathematical relations to calculate or to interpret indexes that could be of clinical interest. An example of

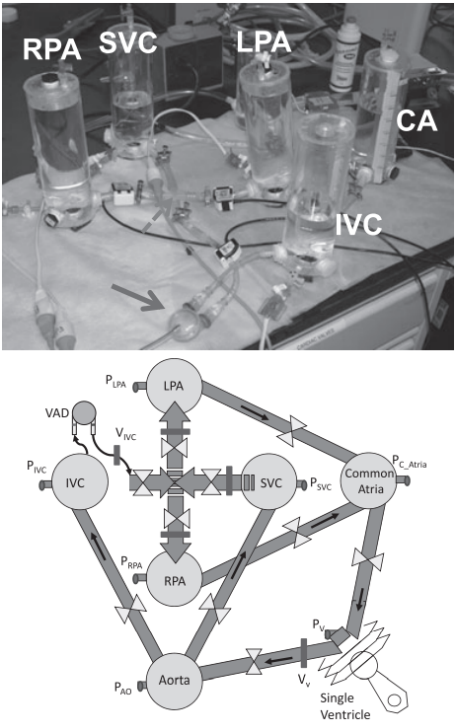

Figure 1.6 Schematic representation of the Fontan flow mock loop (bottom) with ventricle assist device attached to IVC and TCPC in series. The compliance chambers are represented by the circles. The double-triangles, slender rectangles, and small circles represent the needle pinch resistors, velocity, and pressure measurement ports, respectively. Medos VAD inserted in SVB configuration and TCPC model are marked by solid and dashed arrows on the flow loop picture (top), respectively [Reprinted from (Dur et al., 2009) with permission by John Wiley and Sons].

this approach used to investigate SV physiology is represented by the wave intensity analysis. The method consists in the evaluation of the wave intensity to evaluate the ventricular-arterial coupling comparing the working condition of the heart and the rest of the vasculature (Parker, 2009). Traditionally necessitating invasive pressure and velocity acquisitions, wave intensity analysis can nowadays be performed non-invasively, based on cardiac magnetic resonance (CMR) (Biglino et al., 2012b). This technique allows retrospective analysis

on routinely acquired phase-contrast CMR datasets, and it has been applied to HLHS patients to evaluate the effect of surgical arch reconstruction and shunt type on ventricular-arterial coupling (Biglino et al., 2014, 2012a).

Computational models have been proved to be a powerful tool to study a wide range of complex systems. They have the advantage of creating reproducible and controllable environments suitable for performing parametric studies and for acquiring data systematically. Moreover, they give the possibility to evaluate information that can be difficultly obtainable or cannot be directly measured otherwise. Concerning the study of SV defects, computational models have been explored and improved in the past 15 years focusing on the complex hemodynamics of the Fontan circulation. Computational fluid dynamics (CFD) can model the fluid dynamics at different geometrical scales from zero-dimensional (0D) to three-dimensional (3D) allowing easier quantification of hemodynamic variables such as flow rates, pressure, and distribution of shear stress, and inexpensive investigations of the effects of different geometric features and fluid quantities.

A 0D model or a lumped parameter (LP) model is a dynamic representation of the physics that neglects the spatial variation of parameters and variables, which are assumed to be uniform in each spatial compartment (i.e. 0D description). Therefore, an LP model gives rise to a set of ordinary differential equations describing the dynamics in time of the variables in each compartment. In the context of cardiovascular system modelling, the LP description is commonly applied to the major components of the system (e.g. cardiac chambers, heart valves and vascular compartments) to evaluate the global distributions of pressures, flows and blood volumes.

3D modelling of vascular hemodynamics implies to take in consideration a 3D domain, representing the region of interest, that is discretized in a number of smaller domains where the unknowns of the problem will be evaluated. This approach enable a local representation of the hemodynamic field in specific portions of the cardiovascular system, providing full fields of local fluid dynamics quantities (e.g. wall shear stress) while disregarding the global effects on the whole circulation. Nowadays, with the improvements in the imaging techniques it is easier to build 3D patient-specific models of portion of the cardiovascular system for both healthy and pathological patients (e.g. for the treatment of congenital heart diseases).

In earlier computational studies both the 0D and the 3D approach has been employed to investigate the fluid dynamics of SV physiology. Pre- and post-operative (stage 1 to stage 2) were compared with a 0D model (Figure 1.7) describing univentricular circulation to predict the hemodynaimcs in the bidi-

rectional cavopulmonary anastomosis (Pennati et al., 1997, 2000).

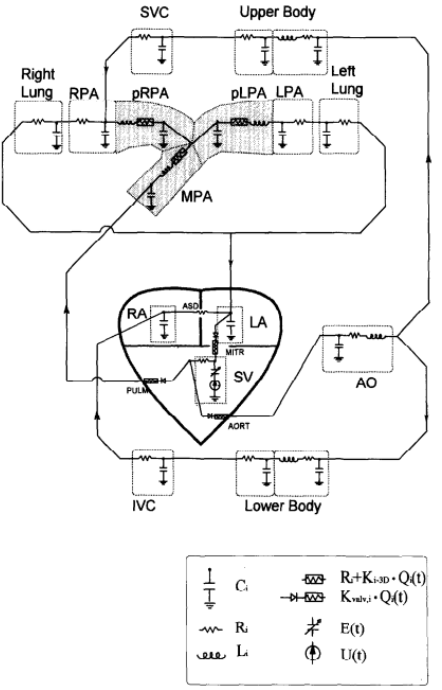

Figure 1.7 Hydraulic network of the post-operative model with the bidirectional cavopulmonary anastomosis. Arrows indicate the normal direction of flow. MPA: main pulmonary artery; pLPA and pRPA proximal left and right pulmonary artery; LPA and RPA left and right pulmonary artery; AO: ascending aorta; IVC and SVC: inferior and superior vena cava; RA and LA: right and left atrium; SV: single ventricle; ASD: atria1 septal defect; PULM: pulmonary valve; AORT: aortic valve; MITE mitral valve [Reprinted from (Pennati et al., 1997) with permission by Elsevier].

Later on, other LP models investigated also the Norwoord (Barnea et al., 1998; Migliavacca et al., 2001) and the Fontan (Pekkan et al., 2005; Pittaccio et al., 2005; Sundareswaran et al., 2008) circulations. However, these models focused on the global fluid dynamics and oxygen transport, do not allow the description of local information such as wall shear stresses or velocity fields occurring in the surgical sites.

Several 3D models were developed, mostly reproducing only the local hemodynamics in a region of interest. In such studies, boundary conditions

for the 3D model (flow and/or pressure) were enforced without feed back from the remainder of the circulatory network. These studies investigated mainly the effects of geometry and blood flow conditions on the fluid dynamics and energy efficiency of SV circulations. Various works investigated the Norwood circulation simulating the local fluid dynamics in realistic geometries of the systemic-to-pulmonary shunt. Some of them were focused on the influence on the local fluid dynamics of geometrical features such as the shunt diameter (Sant'Anna et al., 2003; Song et al., 2001; Waniewski et al., 2005), the shunt shape (Migliavacca et al., 2000a; Waniewski et al., 2005) and the angle of the anastomoses (Migliavacca et al., 2000a; Sant'Anna et al., 2003). Another study (Migliavacca et al., 2000b) used a 3D model to investigate the estimation by means of Doppler measurements of the flow rate across the shunt. Other works focused on the Glenn circulation investigating different type of cavopulmonary connection (Bove et al., 2003; De Zélicourt et al., 2006; Guadagni et al., 2001; Pekkan et al., 2009). Greater attention was placed on the last stage of the surgery (Fontan circulation). The geometry configurations and parameters that have been investigated include, atrio-pulmonary connections versus TCPC procedures (Van Haesdonck et al., 1995), comparison between different types of TCPC procedures (Hsia et al., 2004; Marsden et al., 2009; Migliavacca et al., 1999), the size and shape of the TCPC vessels and their anastomosis (Hsia et al., 2004; Migliavacca et al., 2003; Ryu et al., 2001), the caval anastomosis offset angle of the anastomosis and the planarity of the TCPC vessels (Khunatorn et al., 2002; Migliavacca et al., 1999; Ryu et al., 2001). As an example, Figure 1.8 depicts the velocity field in a novel Y-shaped extracardiac Fontan baffle taking into account also the effect of the respiration.

These models, which describe the vascular area subjected to a surgical treatment in detail, suffer from a severe limitation owing to the inability to account for the interaction with the rest of the circulation. To overcome this important drawback, multiscale models were proposed that couple the 3D representation of the surgical site to a LP model of the circulatory system. These so called multiscale models incorporate 3D and 0D models in an integrated approach aimed at giving detailed analysis at both levels. Generally, the 3D model describes the region of clinical interest (e.g. the shunt or a cavopulmonary connection), while the LP model describes the circulatory system and imposes realistic boundary conditions at the 3D outlets. This multiscale approach could be open loop or closed-loop. In the first case, only outlet boundary conditions are imposed by the 0D network, while inlet boundary conditions are imposed a priori. In the closed-loop approach, instead, the 0D network calculates and imposes both inlet and outlet boundary conditions. Several patient-specific multiscale models in a

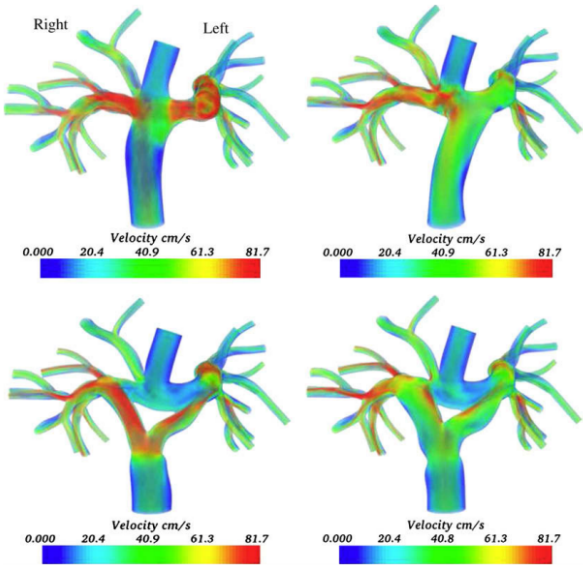

Figure 1.8 Volume rendered velocity magnitude from moderate exercise simulations. The Y-graft design results in reduced unsteadiness in the flow, especially during exercise. Velocities shown correspond to the peak of inspiration when velocity is maximum. [Reprinted from (Marsden et al., 2009) with permission by Elsevier].

closed-loop fashion have been developed to investigate SV physiology (Baker et al., 2013; Baretta et al., 2011; Laganà et al., 2005; Migliavacca et al., 2006). Others simulated conditions different from the one of the clinical acquisition, such as changes across those surgeries, exercise and active conditions (Baretta et al., 2012; Corsini et al., 2014; Kung et al., 2013). Figure 1.9 shows an example of a multiscale model in which the effect of the shunt type on the fluid dynamics of the Norwood operation was investigated. This allowed to compare the models in presence of the same boundary conditions, highlighting the benefits of a multiscale approach in a surgical planning context.

Despite the ventricular functionality plays a fundamental role in determining the efficiency of the univentricular circulation, the ventricular chamber has been always considered with very simplified models considering only the global behaviour of the ventricle. Only recently few computational studies investigated more in detail this aspect. Patient-specific simulations of HLHS cases have been recently performed to investigate the efficiency of the filling (De

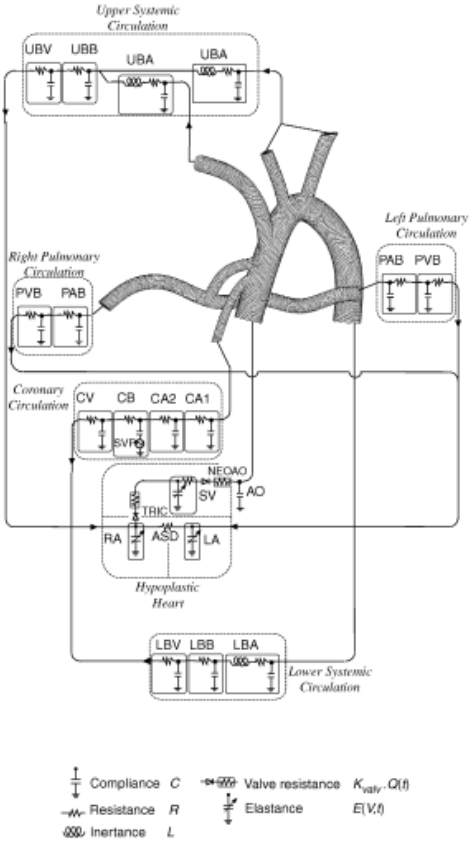

Figure 1.9 Multiscale model of the Norwood circulation. The lumped parameter model is linked to the 3-D model of the central shunt. [Reprinted from (Laganà et al., 2005) with permission by Elsevier].

Vecchi et al., 2012) and to evaluate the reliability of kinetic and viscous energy as clinical markers (De Vecchi et al., 2014). Moreover the diastolic function in HLHS patient models has been further investigated using personalized ventricular models by means of a fluid-structure interaction (FSI) analysis (De Vecchi et al., 2013). More specifically, the effect of ventricular cavity shape and tricuspid inflow topology were evaluated in four patients anatomies, with regard to filling dynamics and assessment of diastolic function in patients post Stage

1 surgery. However, clinically measured ventricular inflow and outflow rates were used to prescribe the corresponding velocity boundary conditions in all these works. Hence, such 3D models of SV cannot be applied to investigate the effect of different surgical procedures, because different unknown boundary conditions have to be prescribed in the post-operative conditions.

1.4 Motivation of the work

The hypoplastic heart syndrome is a complex congenital heart disease that could affect both the left and the right ventricle with different grade of hypoplasia and is not compatible with life. Commonly, it is treated following a three-stage surgical procedure that implies changes in the circulatory layout with the goal of restoring, in the third and last stage, a series of the systemic and pulmonary circulations. In the last decades great improvements in the surgical procedures have been achieved with significant increase in the outcomes for the treatment of SV defects. However, univentricular circulation still represents a critical and peculiar condition. Moreover, among different specialized centers a significant variation in the surgical options is still present and related to the expertise of the surgeons.

With the motivation of an in-depth understanding of SV physiology and to develop engineering tools that may help the surgeon in the decision making process, various approaches to investigate the hemodynamics occurring in these patients have been proposed. Depending on the purpose of the study, the models presented in literature can be categorized into three main groups: *in vitro*, analytical and *in silico*. With the improvements of both 3D imaging techniques and computational resources, in the last 10 years greater attention have been placed on developing CFD models to study patient-specific cases with main objective of planning surgical treatments. Indeed, the present work is part of the international project funded by the Fondation Leducq (Paris), entitled ”Multi-scale modelling of single ventricle hearts for clinical decision support”. This research project, handles the modelling of surgical procedures for the treatment of single ventricle congenital heart diseases. The concept of multiscale models that couple 3D model of vascular region of interest with 0D models that represent the whole circulation in a closed-loop fashion, allows for a better description of the univentricular circulation. The importance of the closed-loop approach is related to the changes occurring in the circulatory layout across the surgical procedure in SV patients. These changes are associated with big modifications in the global hemodynamic of the patient. Usually, the hemodynamic boundary conditions are enforced a priori to a 3D model without feed back from the

remainder of the circulatory network. However, post-operative clinical data are not available due to the invasiveness of clinical exams that are not required after the surgery. Thus, the hemodynamic post operative hemodynamic conditions are unknown. To prescribe appropriate and realistic boundary conditions for the 3D model starting from the pre-operative state the adoption of a closed-loop approach is mandatory. The LP circulatory model can be modified to account for the changes occurring in the circulatory layout of the patient, thus providing new boundary conditions for the 3D model that otherwise are unknown. In the closed-loop approach, indeed, the 0D network calculates and imposes automatically proper hemodynamic boundary conditions to the 3D model according to the global changes of the circulation. Indeed, the 3D model and 0D model mutually interact and after changes in some parameters the multiscale model react until a new steady state condition is reached.

When investigating the efficiency of fluid dynamics in univentricular circulation, the functional ventricular chamber is commonly described by means of simplified lumped parameter models. Only in the very last years, a FSI study placed attention also on the ventricular mechanics. However, this study was focused only on the diastolic phase and disregarded the influence of the circulation highlighting the lack of multiscale models accounting for both the mechanics of the SV and the fluid dynamics description of the circulatory system. Indeed, to the best of my knowledge a multiscale model of SV cardiovascular system accounting for both the 3D anatomy and structure of the ventricle has not been proposed yet. Since the ventricular mechanics plays a fundamental role in determining the behaviour of the whole cardiocirculatory system, the principal aim of this work is to adopt a simulation framework that allows to account in a multiscale and closed-loop fashion for a patient-specific 3D finite element model of the SV to patient-specific LP models of the pre- and post-operative circulations. In this way, in addition to hemodynamic information (flows and pressures) through the circulatory system, the modelling of the 3D structure of the SV allows the evaluation of local parameters as the myocardial stress and strain distributions, which are fundamental in the evaluation of the performance of the ventricle. Furthermore, global parameters such as pressure-volume tracings and cardiac performance (i.e. cardiac output (CO) and ejection fraction) can also be calculated.

1.5 Objectives

The present Ph.D. thesis was developed in the context of a large international project funded by the Fondation Leducq (Paris), entitled 'Multi-scale

modelling of single ventricle hearts for clinical decision support'. In this project a computational multiscale closed-loop model aimed at studying the cardiac mechanics of SV circulation was proposed. The specific target of this work was to predict global hemodynamics and mechanics of the transition between the stage 1 and the stage 2 surgery in patient-specific cases. A key issue in the development of the multiscale model is the estimation of the patient-specific parameters of the different parts of the model. To this aim, a sequential approach involving multiple steps was adopted in this study.

In summary the main objectives of the Ph.D. thesis were:

- to develop a patient-specific multiscale closed-loop model coupling a 3D FE model of SV mechanics to a lumped parameter model able to describe the whole circulatory system;
- to define a sequential approach, based on the clinical data available for the patients involved in the study and literature data, to identify patient-specific parameters of both the circulatory and the FE models;
- to simulates the pre-operative state of the two patients considered in this study;
- to predict the changes in both hemodynamics and mechanics of the patients after the surgical procedure is simulated;
- to simulate additional scenarios as the active state and the investigation of the effect of the fibre orientation.

1.6 General description of the work

In Chapter 1, a brief description of the hypoplastic heart syndrome and the three stage palliative surgery for the treatment of single-ventricle defects is presented. Then, a review of the modelling approaches presented in literature to study the univentricular circulation is reported. Main attention was placed on the computational methods proposed to model such complex cardiocirculatory layout and the techniques adopted so far for the simulation of surgical procedures, highlighting the lack of multiscale models accounting for both the 3D mechanics of the SV and the fluid dynamics of the circulatory system.

In Chapter 2 special attention was posed on the mechanical function of the cardiac tissue. The behaviour of the myocardium was described focusing on the myocardial fibre architecture, the resting and the active mechanical properties

of the ventricular wall. Later on, the different approaches used to model the ventricular mechanics was proposed. At first, a description of the lumped parameter models was given discussing main advantages and disadvantages of this simplified approach. Then the literature FE models of cardiac biomechanics were described, highlighting the validity of FEM as a tool to assess the ventricular functionality of both the normal and pathological heart. With the improvement of imaging and computational techniques FE models could be incorporated in more comprehensive patient-specific multiscale models accounting also for the rest of the circulation in a closed-loop fashion. Finally for sake of completeness, the FSI and the electromechanical approaches was discussed.

In Chapter 3 the clinical data available for the patients considered in this study are presented focusing on the data that are useful in the modelling process. Then, the multiscale closed-loop model adopted to model patient-specific cases of univentricular circulation is discussed. The model is composed by four main parts: a 3D anatomic model of the SV, a passive constitutive model, an active contractile model, and a closed-loop circulatory model that prescribe proper hemodynamic boundary conditions to the 3D model. This model is aimed at simulating both the pre- and post-operative state of SV patients. After each part of the model is described in detail the strategy adopted to tune the patient-specific parameters is described. The strategy involves subsequent steps involving at first the use of both circulatory model and 3D SV model stand alone and then the two are coupled to create the multiscale closed-loop model.

In Chapter 4 the three clinical cases taken in consideration in this work are presented focusing on the specific features peculiar of each patient. The main steps necessary to set-up the pre-operative multiscale models are also reported discussing the obtained results. Then, realistic 3D-0D models were assembled to study pre-operative state and demonstrating the proposed simulation strategy allows the description of the macroscopic behaviour of each patient considered. The obtained results are presented in terms of both global hemodynamic quantities and regional kinematics and mechanics of the single ventricle.

Finally in Chapter 5 the circulatory model was modified to predict both hemodynamics and mechanics occurring in the patients after the simulation of the surgery. The results provided by the post-operative simulations were compared to those obtained from the pre-operative models. Then, additional scenarios are considered to test the ability of the model to replicate conditions different from the clinical states. In particular, active state conditions and influence of the fibre orientation are investigated and discussed.

Chapter 2

Models of cardiac biomechanics

The heart is a complex organ that provides blood flow to the body. His mechanical behaviour is determined by a number of physical phenomena. In this chapter a description of the myocardial structures and mechanical properties of the cardiac tissue is reported. A brief review of the mathematical approaches used in literature to investigate the ventricular function is also presented.

2.1 Introduction

THE human heart is a mechanical pump that drives blood flow through the cardiovascular system and his mechanical behaviour is modulated by a number of physical phenomena spanning across spatial and time scales. This complex function is the result of the interplay between many aspects such as electrical propagation, contraction of cardiac cells, arrangement of the cells in the cardiac wall, the pressure by which the heart is filled and the pressure against which the heart must eject. The behaviour of the myocardial tissue has been a major research focus for clinicians, physiologists, engineers and physical scientists who have sought to develop mathematical models to characterize cardiac mechanics. Indeed, mathematical modelling represents a powerful research tool to understand such a complex phenomenon under both the physiological and the pathological states. A key foundation of these models is the continuum mechanical description of the heart, providing a system of partial differential equations that may be solved to simulate tissue motion and blood flow. In Figure 2.1 an example of a mathematical model that account for both mechanics and electrophysiology is reported, highlighting the main components.

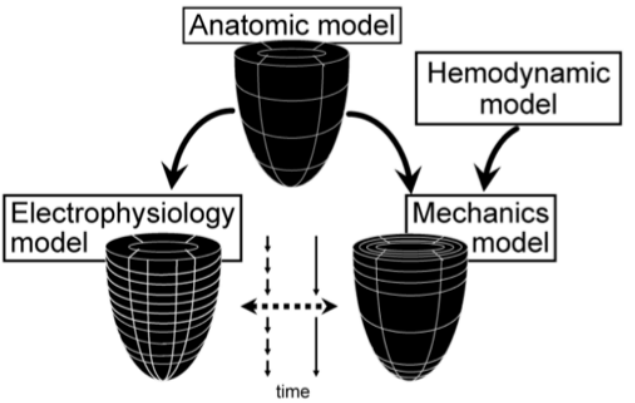

Figure 2.1 The four most important components to model cardiac electromechanics: anatomy, electrophysiology, mechanics, and hemodynamics. Ventricular anatomy is fitted to morphological measurements. The anatomical representation is then appropriately refined in space and time to reflect the physics of the specific part of the problem. [Reprinted from (Kerckhoffs et al., 2006) ©2006 IEEE].

In this example the model is composed by four main parts: an anatomical model accounting of the geometry of the ventricle, an electrical model that describes the electrical propagation, a mechanical model accounting for passive and active behaviour of the myocardium and a hemodynamic model to prescribe hemodynamic boundary condition.

Several studies has been proposed in literature that investigate the cardiac mechanics of both animals and humans. With the advent of improved numerical algorithms and increased computational power comprehensive multiphysics or multiscale models enabled novel possibility in the investigations of the cardiac function. However, as highlighted in section 1.3, only few recent studies focused the attention on the study of the SV mechanics. In this chapter, the fibre structure of the myocardium is described, as well as the passive and active behaviours of the cardiac tissue. Moreover, a description of the mathematical approaches used to model the ventricular mechanics is reported, distinguishing between 0D and 3D models. Then, a brief analysis of the multiscale models developed to couple the mechanical response of the heart to the fluid flow is reported. Finally, the approaches proposed in literature to describe the electromechanical function are mentioned.

2.2 Structure of the myocardium

The myocardium presents a complex 3D muscle fibre architecture. Several studies highlighted the presence of obliquely oriented muscle fibres whose orientation varies from a right-handed helix at the endocardium to a left-handed helix at the epicardium. Although the myocytes are relatively short, they are connected such that at any point in the normal heart wall a clear predominant fibre axis (approximately tangent with the wall) is observable. In the studies of Hort (Hort, 1957) and Streeter and colleagues (Streeter Jr. and Bassett, 1966), first quantitative measurements of smooth transmural distribution of fibre orientation have been reported. Later on, more detailed studies (Armour and Randall, 1970; Streeter Jr. et al., 1969) supported this view across different species, including human hearts (Fox and Hutchins, 1972; Greenbaum et al., 1981). More modern histological techniques have shown that in the plane of the wall, the mean muscle fibre angle makes a smooth transmural transition from epicardium to endocardium (Figure 2.2). Except in certain pathologies, myofibre angle dispersion is typically 10 to 15° (Karlon et al., 1998). Similar patterns have been described for humans and different animal species (e.g. dogs, baboons, pigs and rats). In the left ventricle of humans or dogs, the muscle fibre angle typically varies continuously from about $-60°$ at the epicardium to about $+60°$ at the

endocardium (Streeter Jr. et al., 1969). In the RV the orientation varies from -60° at the epicardium to $+90^\circ$ at the endocardium (Helm et al., 2005).

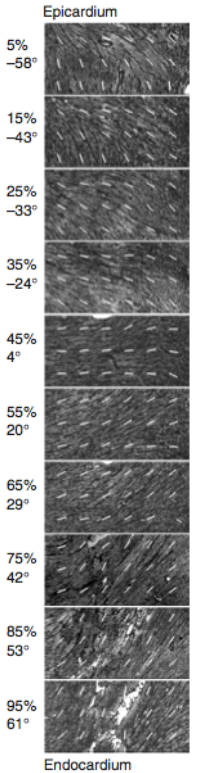

Figure 2.2 Cardiac muscle fibre orientations vary continuously through the left ventricular wall from a negative angle at the epicardium (0%) to near zero (circumferential) at the midwall (50%) and to increasing positive values toward the endocardium (100%) [Reprinted from (Bronzino, 2006) with permission by Taylor and Francis].

Although the traditional notion of discrete myofibre bundles has been revised in view of the continuous transmural variation of muscle fibre angle in the plane of the wall, a transverse laminar structure in the myocardium, separated by histologically distinct cleavage planes, has been observed (Smaill and Hunter, 1991; Spotnitz et al., 1974). In an extensive review of fibre studies, Streeter et al. (Streeter Jr., 1979) acknowledge that there is a substantial dis-

continuity in the muscular architecture of the ventricles at both the microscopic and macroscopic level. These findings have been confirmed quantitatively in the anatomical studies of LeGrice and colleagues (LeGrice et al., 1995), who report that the ventricular myocardium is a composite of discrete layers of myocardial muscle fibres tightly bound by endomysial collagen (Figure 2.3). These myocardial laminae groups fibres together in sheets of 4 ± 2 myocytes thick and continuously branch in each direction throughout the ventricular walls. Their orientation is generally normal to the ventricular surfaces.

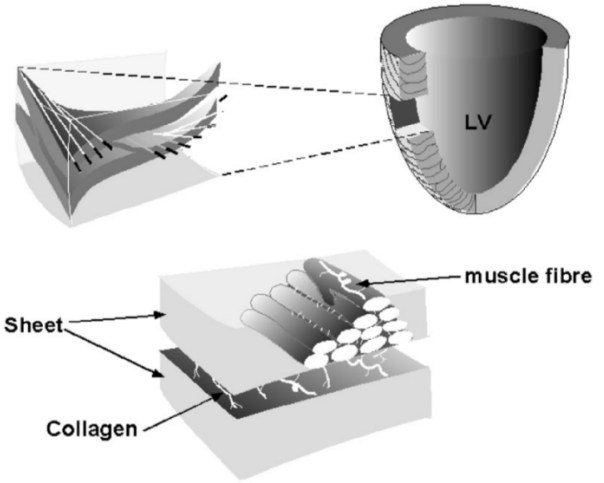

Figure 2.3 Schematic of fibrous-sheet structure of cardiac tissue. A transmural segment (top left) from the ventricular wall is shown with fibre axis vectors embedded in the myocardial sheets, which are 3 to 4 cells thick, as shown in lower figure. The myocytes are bound into the sheets with endomysial collagen and loosely connected with perimysial collagen [Reprinted from (Stevens et al., 2003) with permission by Elsevier].

Thus, for modelling purposes, it is convenient to define a natural set of material directions to characterise the structure of myocardial tissue at an arbitrary point in the heart wall Figure 2.4. The first of these directions refers to the fibre axis and coincides with the muscle fibre direction at each point. The sheet axis is defined to lie in the plane of the muscle layer and is perpendicular to the fibre direction. The third axis is defined to be orthogonal to the first two and refers to the sheet-normal axis as it is perpendicular to the muscle layer.

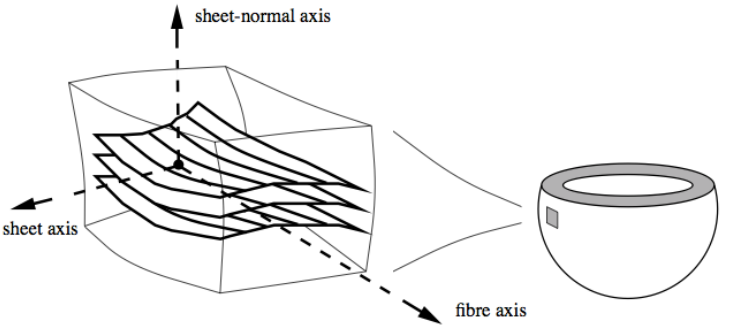

Figure 2.4 Microstructural material axes for myocardial tissue. [Reprinted from (Nash and Hunter, 2000) with permission by Springer].

2.3 Passive properties of the myocardium

Early models of ventricular mechanics used isotropic representations to describe the material properties of the myocardial tissue. In these models, the muscle response is considered without considering a material preferred direction (Gould et al., 1972; Sandler and Dodge, 1963; Wong and Rautaharju, 1968). However, as pointed out in section 2.2 several studies of tissue structure have revealed a clear fibrous architecture of the myocardial tissue (LeGrice et al., 1995; Smaill and Hunter, 1991; Streeter Jr., 1979; Streeter Jr. et al., 1969) which has important implications in determining the anisotropic mechanical properties of the cardiac wall.

The finite element methods (FEM) enabled the use of finite deformation theory, whose detailed analytical approach is prevented from the non linear nature of the equations, associated with the possibility to consider more realistic geometric models. One of the first FE model that incorporate material anisotropy and heterogeneity was proposed by Janz and Grimm (Janz and Grimm, 1972). In addition to the more realistic geometry, the model included an inner layer of compliant transversely isotropic myocardial elements, for which the tissue possessed a single preferred direction. While providing some qualitative insights into predicted myocardial stress distributions depending on the degree of heterogeneity and anisotropy, the quantitative accuracy of predicted stresses was questionable due to the use of small-strain elasticity theory. In a subsequent study (Janz et al., 1974) the finite element model was refined to include large deformation theory and concluded that the small-strain theory overesti-

mated the diastolic pressure-volume and stiffness-pressure relationships. They concluded that stress distributions derived from ventricular mechanics models based on small-strain elasticity theory must be treated with caution. The first non-axisymmetric large deformation FE model of the LV was proposed by Hunter and colleagues (Hunter, 1975). This model represented ventricular myocardium as an incompressible, transversely isotropic material and incorporated the transmural distribution of fibre orientations measured in the study of Streeter et al. (Streeter Jr. et al., 1969). Further studies have led to a more detailed description of the passive behaviour of the myocardium as an hyperelastic tissue incorporating transversely isotropic constitutive laws to represent the passive mechanical response of myocardial tissue (Bovendeerd et al., 1992; Guccione et al., 1995, 2003; Horowitz et al., 1988; Humphrey et al., 1990a; Huyghe et al., 1992; Panda and Natarajan, 1977; Vetter and McCulloch, 2000; Walker et al., 2005, 2008; Wang et al., 2009). Based on the evidences that the cardiac tissue is a composite of discrete layers of myocardial muscle fibres, also orthotropic constitutive models have been proposed (Costa et al., 2001; Holzapfel and Ogden, 2009; Nash and Hunter, 2000; Schmid et al., 2006).

However, to predict normal myocardial tissue response during the cardiac cycle, it is essential that the material properties (parameters of the constitutive law) are estimated using observations from experimental studies of healthy cardiac tissue. The most common experimental technique used to quantify the material properties of heart tissue has been *in-vitro* biaxial tension tests on thin sections of cardiac muscle (Demer and Yin, 1983; Humphrey et al., 1990b; Smaill and Hunter, 1991; Yin et al., 1987). Figure 2.5 shows an example of biaxial tests on isolate canine myocardium. Typically, forces are applied at the cut edges of the sample and the resulting deformation field is used in a FE representation of the experiment to fit the parameters of a pre-defined constitutive equation. These studies have revealed that cardiac tissue exhibits highly nonlinear, anisotropic stress-strain behaviour (typical of most soft biological tissues). More specifically, the strain stiffening properties of myocardium are more pronounced in the fibre direction than in the directions normal to the fibre axis. Figure 2.6 schematically illustrates the typical stress-strain relationships for myocardium. The main disadvantage of such a method is that the tissue samples have been cut from the ventricular wall and hence some of the collagen structures, which largely determine the passive tissue elasticity, have been damaged. Nevertheless, biaxial tests have provided valuable insights into the nonlinear form of the stress-strain response of myocardium, and have been used to effectively determine elastic limits of the tissue along the microstructural material directions.

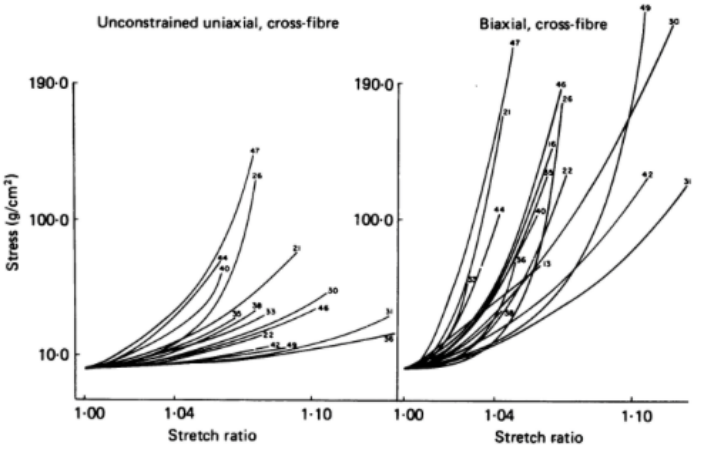

Figure 2.5 Comparison of the loading portions of the stress-stretch curves in the cross fibre direction during unconstrained uniaxial and equal biaxial loading.The numbers identify each particular specimen which was subjected to both types of boundary conditions. In each instance the tissue was stiffer under biaxial as compared with uniaxial [Reprinted from (Demer and Yin, 1983) with permission by John Wiley and Sons].

Alternatively, measurements of regional tissue deformations in isolated or intact whole hearts subject to prescribed loading conditions can be used together with the solution of a boundary value problem to estimate material constants of an assumed constitutive law in a semi-inverse analysis. The FEM is particularly well suited for this inverse analysis due to its ability to incorporate the 3D geometry, fibrous tissue architecture, pressure boundary conditions, and nonlinear material properties of the tissue. If a model accurately describes experimentally measured 3D strains, this provides confidence in the estimated stresses, which are important for understanding myocardial growth and remodeling in physiological and pathophysiological conditions.

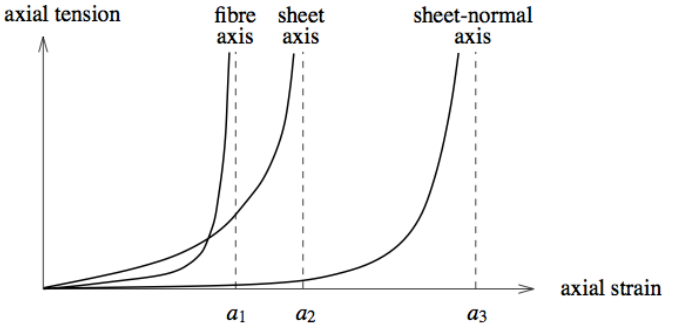

Figure 2.6 Typical nonlinear stress-strain properties of ventricular myocardium. The parameters a_1, a_2 and a_3 represent the limiting strains for elastic deformations along the fibre, sheet and sheet-normal axes, respectively. Note the highly nonlinear behaviour as the elastic limits are approached. [Reprinted from (Nash and Hunter, 2000) with permission by Springer].

2.4 Active properties of the myocardium

Early models of the active behaviour of the cardiac tissue were based largely on the skeletal muscle models of Hill (Hill, 1970) and Huxley (Huxley, 1957). The first is a phenomenological model that describe experimental observations in the skeletal muscle. It consists of a passive element in parallel to a series arrangement of a contractile element and an elastic element. The contractile element describes the generation of active stress by the sarcomeres as a function of sarcomere length (SL), time elapsed since activation and sarcomere shortening velocity. The latter is a microstructural model that describes the muscle properties from the microscopic processes accounting for the the cross bridge formation (i.e. the binding of myosin heads to actin filament). Later on, other cardiac muscle models have been proposed with basis varying from an empirical to a biophysical approach: Hill's models, in which the active fibre stress development is modified by shortening or lengthening according to the force-velocity relation, so that fibre tension is reduced by increased shortening velocity (Arts et al., 1982; Lumens et al., 2009; Nevo and Lanir, 1989); history-dependent models, either based on Huxley's cross-bridge theory, which yields a system of partial differential equations as functions of time and crossbridge position, or on myofilament activation models (Landesberg et al., 2000; Landesberg and Sideman, 1994; Regnier et al., 1995; Rice et al., 2008).

When the myocardium is modeled by means of solid mechanics, active fibre

stress can be incorporated into the constitutive formulation by adding the contribution of the fibre active stress acting along the fibre direction to the passive stress due to tissue deformation. Among different ways of integrating the active tension tensor into the passive stress tensor, the most straightforward method of integration is to add the time varying active tension calculated from a dynamic tension model to the first component (i.e. direction of the fibres) of the passive Cauchy stress tensor (Hunter et al., 1998; Nash and Hunter, 2000; Niederer and Smith, 2009; Vendelin et al., 2002). This approach was generalized by Usik and collaborators (Usyk and McCulloch, 2003b) by adding different active tension components in the fibre, cross fibre and sheet normal directions according with experimental studies (Lin and Yin, 1998). Finally, Watanabe and co-workers (Watanabe et al., 2004) using a completely different integration framework, defined the active tension as a strain energy density function with coefficients that scale with the time varying active tension.

To describe the active properties of the myocardium, parameters of the active models need to be estimated from experiment. Experimental tests are often performed on excised rat trabeculae. Isometric contraction tests revealed the active force generated by sarcomeres while SL is kept fixed. The relation between twitch duration, force and SL was investigated by Janssen and collaborators (Janssen and Hunter, 1995). Typical results highlighting the dependence of twitch duration and maximum stress level on the SL are showed in Figure 2.7. Kentish et al. (Kentish et al., 1986) showed how active stress rises with SL and calcium concentration (Figure 2.8). Minimum SL for stress to develop was about 1.6 μm, much lower than in the passive unloaded trabecula, which is about 2.0 μm. The relation between force and shortening velocity appears to be hyperbolic and it is known as the Hill relation, after A.V. Hill first studied this relation in skeletal muscle (Hill, 1938). Brutsaert et al. (Brutsaert and Sonnenblick, 1971) were among the first to report on the force-velocity relation in cardiac muscle. However, data obtained after the introduction of the optical technique to control SL are more reliable (De Tombe and Ter Keurs, 1990).

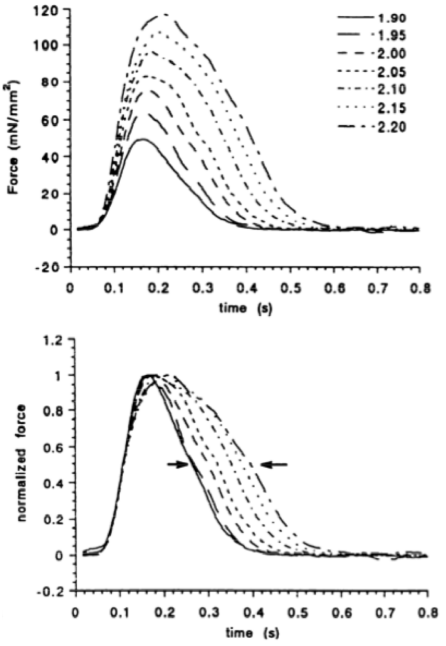

Figure 2.7 Superimposed tracings of active force from a single rat trabecula over a range of SL and extracellular levels of 2.0 mM. SL ranges from 1.90 to 2.20 μm. In the bottom panels, active force was normalized to peak twitch tension level of each contraction separately. Arrows emphasize prolongation of late systolic phase. Muscle was stimulated at t = 0.05 s [Reprinted from (Janssen and Hunter, 1995) with permission by The American Physiological Society].

2.5 Modelling the ventricular mechanics

Cardiologists and physiologists have long been interested in the quantification of the ventricular function in normal and pathological conditions. In this view, models of cardiac mechanics are valuable in understanding the normal and diseased heart, and as data accumulate on molecular and cellular mechanisms, the potential for powerful predictive mechanistic models is continually growing. Various parameters can be measured *in vitro*, such as morphology and biochemistry, and then this information can be used to implement models *in silico*. The results are then validated *in vivo*, leading to iterative model refinement. Since the first modeling studies on cardiac mechanics (Sandler and

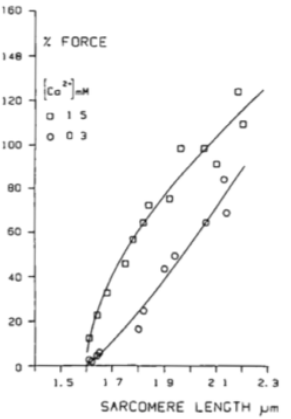

Figure 2.8 Force-sarcomere length relations at different Calcium concentration. Concentration was 1.5 mM (squares) or 0.3 mM (circles) [Reprinted from (Kentish et al., 1986) with permission by Wolters Kluwer Health].

Dodge, 1963; Wong and Rautaharju, 1968), various approaches have been explored in literature. Depending on the objectives of the work various model ranging from simple 0D to complex and more realistic 3D have been adopted to describe the ventricular function. In the next subsections, a brief description of the most common approaches is given.

2.5.1 Lumped parameters models

The simplest model to describe the behaviour of a ventricle is the time-varying elastance model proposed by Suga et al. (Suga et al., 1973). This model is a phenomenological description of the ventricular behaviour in the pressure-volume plane and it is based on the observation that the end-ejection points at various filling volumes are located on a straight line. The slope of this line is called maximum elastance E_{max} and the intercept with the volume axis is called V_0. This assumption is also extended at other constant moments in the cardiac cycle, the corresponding points in the pressure-volume diagram for various filling diastolic volumes are located on a straight line, and this line intersects the volume axis at V_0. The passive pressure-volume line has an elastance E_{pas}. During the cycle, the changing activation of the myocardial tissue is modelled as a change of the elastance between E_{pas} and E_{max}. The model is calculated as follow:

$$P_{ch} = E(t)\,(V(t) - V_0) \tag{2.1}$$

with:

$$E(t) = E_{pas} + a(t)\,(E_{max} - E_{pas}) \tag{2.2}$$

where $a(t)$ is a dimensionless normalized activation function, varying from 0 in the passive state to 1 in the active state. Even though this model represents a good starting point to describe the cardiac function, it presents several limitations. First the linear relation between the pressure and the volume is an approximation of the real behaviour of the ventricle. As reported in sections 2.3 and 2.4, the steepness of the end-ejection pressure-volume relation increases with increasing volume, while the steepness of the end-ejection pressure-volume relation decreases with increasing volume. Second, the model disregard the viscous effect of the myocardium. It has been proposed that the model should be extended with a flow-dependent term (Danielsen and Ottesen, 2001). Third, while the pressure-volume relation at end-ejection intersects the volume axis at V_0, the pressure-volume relations for other instants of time during the cardiac cycle do intersect the volume axis at different and greater volumes (Segers et al., 2001).

A more realistic lumped parameter model is the so called 1-fibre model proposed by Arts et al. (Arts et al., 1991). In this model, the global left-ventricular pump function as expressed in terms of cavity pressure and volume is related to local wall tissue function as expressed in terms of myocardial fibre stress and strain. This model is based on the *a priori* assumption of homogeneity of fibre strain and stress in the cardiac wall and relates properties at the fibre level with properties at the ventricular level. Hence, fibre stress and strain may be approximated by single values, being valid for the whole wall. When assuming rotational symmetry and homogeneity of mechanical load in the wall, the dimensionless ratio of muscle fibre stress σ_f to ventricular pressure P_{lv} appears to depend mainly on the dimensionless ratio of cavity volume V_{lv} to wall volume V_w and is quite independent of other geometric parameters. In their study, Arts et al. (Arts et al., 1991) found that a good and simple approximation of this relation considering a spherical ventricular model is given by the following relation:

$$\frac{\sigma_f}{P_{lv}} = 1 + 3\frac{V_{lv}}{V_w} \tag{2.3}$$

To complete the model relating the wall mechanics to the cavity mechanics the equation 2.3 is complemented by a relation between the ventricular volume and

the sarcomere length. This relation is derived from the condition for which the ventricular mechanical work dW as a whole is composed by the work of all the fibres in the wall:

$$dW = P_{lv} dV_{lv} = V_w \frac{\sigma_f}{l_s} dl_s \tag{2.4}$$

Elaboration of equation 2.3 and 2.4 leads to:

$$l_s = l_{s0} \left(\frac{1 + 3\frac{V_{lv}}{V_w}}{1 + 3\frac{V_{lv0}}{V_w}} \right) \tag{2.5}$$

where l_s is the sarcomere length, l_{s0} is defined as the sarcomere length in the reference state with the cavity volume V_{lvo}. It is convenient to choose the reference state as the state of zero cavity pressure in the passive ventricle.

2.5.2 Finite element models

In comparison with the models presented in the previous subsection, FE models allow a more complex description of the ventricular mechanics. As for most practical applications, materials behave nonlinearly and geometry assume complex shapes. FE model allows to account for more realistic geometry and fibre orientation and for a more realistic description of the material properties of the cardiac tissue. The geometric domain is discretized into a number of smaller regular elements, over which quantities of interest (for example the geometric coordinates of a point) are continuously approximated. It is often convenient, if not necessary, to use several different coordinate systems for the FEM for finite deformation elasticity. For instance, stress components are most conveniently expressed with respect to a system of material coordinates aligned with structural features of the body (i.e. the fibre direction). For each element, the equations governing finite deformation elasticity are expressed in terms of known material properties and the unknown displacements of the element nodes. Element contributions are assembled into a global system of equations to ensure that the solution is compatible across element boundaries. The system of nonlinear equations are solved, subject to boundary constraints, to yield a set of deformed nodal coordinates from which deformation patterns are approximated using interpolation.

Anatomically detailed 3D models of geometry and myofibre orientation for different species have been proposed in literature (Figure 2.9) for rabbit (Vetter and McCulloch, 2000), dog (Kerckhoffs et al., 2003b; LeGrice et al., 1997; Nielsen et al., 1991), pig (Stevens and Hunter, 2003), sheep (Sun et al., 2009;

Walker et al., 2005) and human (Krishnamurthy et al., 2013; Palit et al., 2015; Wang et al., 2013, 2009; Xia et al., 2005). Geometries of these models have been obtained from histological measurements, computer tomography (CT), or MRI scans and myofibre orientations have been reconstructed from histological measurements diffusion weighted MRI or by calculations.

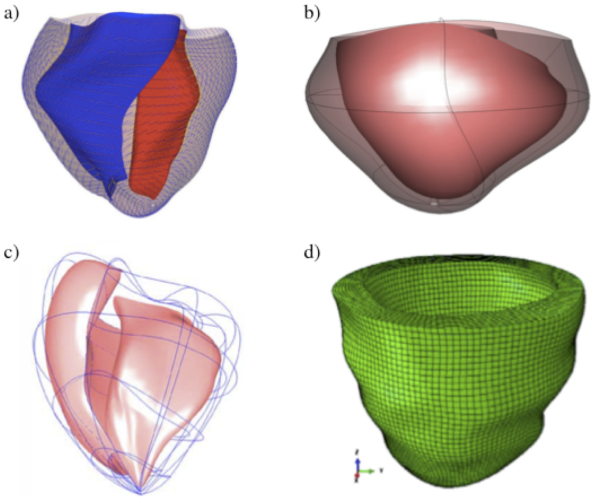

Figure 2.9 Anatomic models of: a) rabbit (Vetter and McCulloch, 2000); b) dog (Kerckhoffs et al., 2003b); c) pig (Stevens and Hunter, 2003); and d) human (Wang et al., 2009).

3D computational models of cardiac biomechanics have proved to be a valid tool to assess regional information (e.g. stress and strain) in the normal and abnormal heart. These models have been extensively used to investigate stress and strain in the myocardial wall in both the intact heart (Stevens and Hunter, 2003; Vetter and McCulloch, 2000) and under the effect of different pathologies such as infarct (Kerckhoffs et al., 2009, 2007; Wenk et al., 2011) and aneurysm (Sun et al., 2009; Walker et al., 2005, 2008). FE models have been also proposed to study possible new therapies as the injection of hydrogel into the infarcted myocardium to enhance the ventricular function after heart failure (Kortsmit et al., 2013; Miller et al., 2013) or the use of a cardiac assist device with a twist apical torsion to improve failing heart function (Trumble et al., 2011). Wang and colleagues (Wang et al., 2013, 2009) proposed a model of the human left ventricle to study the influence of fibre orientation in the mechanics of dias-

tole. Recently, models of cardiac growth have been implemented to simulate the ventricular adaptation in case of pressure and volume overload in the LV (Kerckhoffs, 2012; Kerckhoffs et al., 2012).

With the improvements in the imaging techniques, nowadays, it is easier to build patient-specific models of cardiovascular hemodynamics for both healthy and pathological patients. Krishnamurthy et al. (Krishnamurthy et al., 2013) proposed a multiscale model that couple a 3D ventricular model to 0D model of the whole circulatory system to study five infarcted patients (Figure 2.10a). Moreover they developed an unloading algorithm to find the unloaded geometry of the patents starting from the available ED geometry reconstructed from CT scans demonstrating the efficacy of such models in replicating the behavior of the patients. Lee et al. (Lee et al., 2014) included an intra ventricular parachute device in a patient-specific model of the LV (Figure 2.10b) to evaluate the improvement of the ventricular function after myocardial infarct. The authors in addition to simulating a beating LV simulates the entire implantation process of a parachute system to account for possible influence of the residual stress caused by the implanted device on the LV function.

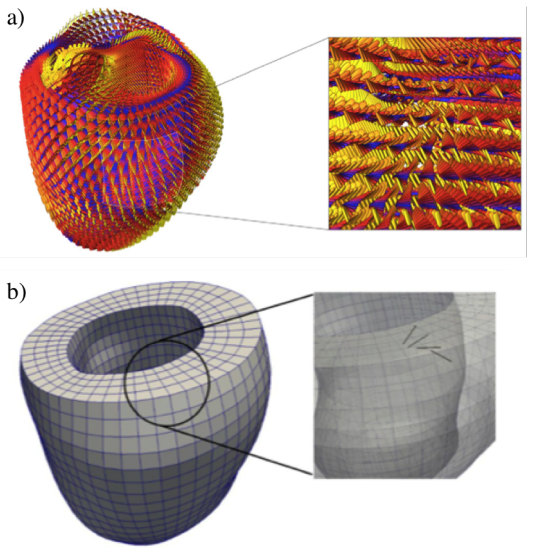

Figure 2.10 Fibre orientations in patient-specific finite element models. a) bi-ventricular model (Krishnamurthy et al., 2013) and b) LV model (Lee et al., 2014)

2.5.3 Multiphysics models

Cardiac performance is not only determined by the mechanical function of the ventricle, but it is due to a complex interaction of biological and physical processes. Moreover, such mechanisms result from intricate coupling that may involve different physical processes and span spatio-temporal scales. Myocardial contraction and relaxation is related to the dynamic of blood flowing through the heart chambers. Through the physical coupling of the myocardium and the blood which fills its chambers, mechanical energy is transferred to kinetic energy in the fluid, driving the transport processes essential for the survival. Modeling the interactions between the blood flow and the deforming vascular structure represents one of the major challenges in cardiovascular mechanics. In order to couple the ventricular blood flow to tissue mechanics, the boundary of the ventricular blood must remain geometrically compatible with the boundary of the solid.

One possible approach proposed in literature to account for the fluid-solid mechanics interactions is represented by the immersed boundary (IB) approach (Lemmon and Yoganathan, 2000; McQueen and Peskin, 2000). In this method the solid domain is not explicitly represented within the fluid domain, but rather exists by the additional force field that the solid exerts on the fluid where the two domains overlap. McQueen et al. (McQueen and Peskin, 2000) incorporated both right and left ventricles as well as valve structures, including anatomical details. In his study, Lemmon et al. (Lemmon and Yoganathan, 2000) simulated atrio-ventricular coupling by means of an idealized model of the left heart (atrium and ventricle). Recently, a dynamic models of LV function in health and disease using a version of the IB method that uses Lagrangian FE methods to describe the mechanics of the ventricular myocardium have been developed, considering the diastolic state (Gao et al., 2014a) and both active and passive phases (Gao et al., 2014b).

One of the first fluid structure interaction (FSI) model was an axisymmetric two dimensional model of a simplified canine ventricle in which nonlinear thin-shell theory were applied to simulate the filling of the ventricle (Vierendeels et al., 1999, 2000). Watanabe et al. (Watanabe et al., 2002) presented a three-dimensional FSI model incorporating the propagation of excitation and excitation-contraction mechanisms to simulate normal excitement and arrhythmia was simulated. Under the assumption that both fluid and structure inertias were negligible the fluid-structure interaction was restricted to the pressure acting on the interface. The model was further improved incorporating the dynamics of the left atrium and pulmonary circulation into the model to simulate the ventricular filling dynamics (Watanabe et al., 2004). A more refined fluid

model (Cheng et al., 2005) was proposed to study the diastolic phase of the left ventricle (modeled with a 3D ellipsoidal thin-wall geometry). The authors used a scheme applying the finite volume method to discretize the arbitrary Lagrangian-Eulerian formulation of the Navier-Stokes equations for the fluid and a nonlinear FEM to model the structure. The coupling of the fluid and the structure was implemented by combining fluid and structure equations as a unified system and solving it simultaneously at every time step. However, this model treated the myocardial wall as a thin-walled neo-Hookean material instead of incorporating a more comprehensive constitutive model. Recently, patient-specific FSI model has been proposed to investigate a case of Tetralogy of Fallot (Tang et al., 2010). The authors used the model to evaluate and optimize human pulmonary valve replacement surgical procedure and patch design and test a surgical hypothesis that valve replacement with small patch and aggressive scar tissue trimming may lead to improved recovery of RV function and reduced stress/strain conditions in the patch area Figure 2.11. Another patient-specific coupled model was published by Nordsletten et al. (Nordsletten et al., 2011), which incorporates patient-specific geometries and the anisotropic fibre distribution used with current state of the art tissue mechanical models.

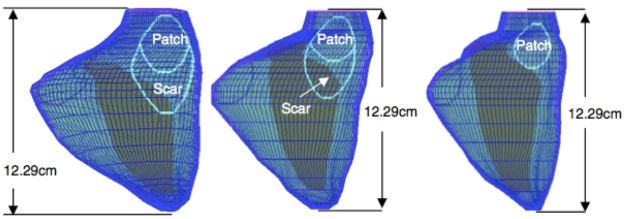

Figure 2.11 Sketch of models with different patch designs. a) Pre-operation model with the old patch and scar tissues; b) patch model 1 with a conventional patch and minimum scar tissue trimming; and c) patch model 2 with a small patch and aggressive scar tissue trimming [Adapted from (Tang et al., 2010)].

The mechanical function of the heart is heavily dependent on the myocardial architecture and this structure also contributes to the anisotropic electrical properties of the cardiac tissue. Responding to membrane depolarization, the myocyte is flooded with intracellular calcium, regulating the contractile apparatus to produce tension. Two different approach have been used to develop electromechanics models: strong and weak coupled models. In weak coupled models, the electrophysiology and mechanics problems are solved separately, with

only the timing of activation passing between the two systems. This method greatly reduces the computational load of the problem and increases numerical stability. The strong coupling consists in solving electrophysiology and mechanics simultaneously and using feedback mechanisms between the two systems. This method is computationally more demanding than weak coupling and is prone to numerical instabilities.

A number of weakly coupled electromechanics models have been proposed. Kerckhoffs and co-workers (Kerckhoffs et al., 2003a,b), investigates the effect of pacing in case of asynchronous activation. In these models the LV was first described as a truncated ellipsoid and then extended to include an anatomical heart geometry. Passive myocardial material was considered anisotropic and nonlinearly elastic and realistic fibre orientation was implemented. Watanabe et al. (Watanabe et al., 2004) proposed a weak coupling model also including the ventricular fluid. In this model cellular electrophysiology is simulated by a phenomenological model and propagation is calculated through monodomain equations. Recent multiscale models of ventricular electromechanics provided insights into the mechanisms by which electrical dyssynchrony can exacerbate mechanical pump dysfunction in dyssynchronous heart failure (Kerckhoffs et al., 2009, 2010; Niederer et al., 2011). Aguado-Sierra et al. (Aguado-Sierra et al., 2011) proposed a patient-specific modeling of dyssynchronous heart failure, and illustrated the approaches taken to tackle modeling challenges that generate clinically useful personalized models of cardiac electro-mechanical function Figure 2.12.

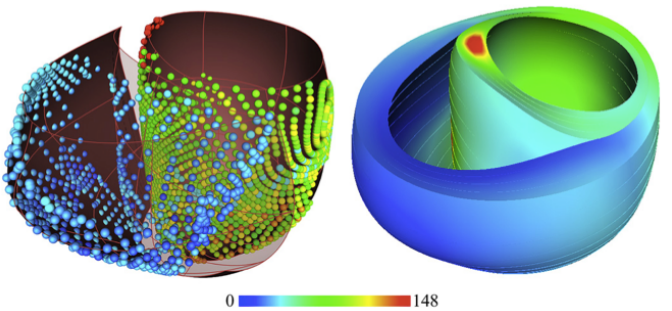

Figure 2.12 Electroanatomic map measurements of left bundle branch block (left) projected to the end-diastolic mesh and resulting activation times (right) from the computational model [ms]. Red indicates the latest activated region, coinciding with the basal location of a scar [Reprinted from (Aguado-Sierra et al., 2011) with permission by Elsevier].

Due to the computational challenges, few strongly coupled models have been developed. Nickerson and co-workers (Nickerson et al., 2006, 2005) developed a 3D strongly coupled electromechanics LV model. The ventricular geometry is represented by a truncated ellipsoid. Electrical activation is simulated by monodomain equations with cellular electrophysiology modeled using a simplified ventricle cell model adapted to include stretch activated channels. Tension is modeled using a model of contraction that includes dependence on SL and velocity of shortening of the sarcomeres (Hunter et al., 1998). Usyk et al. (Usyk and McCulloch, 2003b) developed a 3D anatomically detailed model of ventricular electromechanics to study the role of biventricular pacing on regional myocardial mechanics during the cardiac cycle in case of dilated failing heart. Investigation of the relationship between regional electrical activation and the timing of fibre shortening during normal and ventricular paced beats (Usyk and McCulloch, 2003c) was performed. Xia et al. (Xia et al., 2005) developed a biventricular model, coupling the electrical and mechanical properties of the heart. The mechanical analysis was based on composite material theory and the FEM, the propagation of electrical excitation was simulated using and electrical heart model, and the resulting active forces were used to calculate ventricular wall motion. Fibre orientation was set according to literature studies.

2.6 Conclusions

The complex function of the heart is the results of the interplay between different aspects such as electrical propagation, contraction of cardiac cells, arrangement of the cells in the cardiac wall, the pressure by which the heart is filled and the pressure against which the heart must eject. In this chapter, more attention was posed on the mechanical function of the cardiac tissue. The beahviour of the myocardium was described focusing on the myocardial fibre architecture, the resting and the active mechanical properties of the ventricular wall that play a fundamental role in carrying out the mechanical function of the heart (section 2.2, 2.3 and 2.4).

In section 2.5 a description of different approaches used to model the ventricular mechanics was proposed. At first, a description of the lumped parameter models was given. While this approach has many advantages in terms of simplicity and calculation time, it presents several limitations. However, depending on the purpose of the study, they represents a good starting point to describe the cardiac functionality. The use of the FEM allows for a more complex description. With this method, it is possible to account for realistic geometry and

fibre orientation and for a more complex description of the material properties of the cardiac tissue. Several FE models of cardiac biomechanics have been proposed to investigate both the normal and pathological heart, proving to be a valid tool to to assess regional information that are difficult to obtain otherwise. These models have been successfully used to evaluate heart function in infarcted heart and in case of ventricular aneurysm or to test innovative surgical procedure. With the improvement of imaging and computational techniques FE models could be incorporated in more comprehensive patient-specific multiscale models accounting also for the rest of the circulation in a closed loop fashion. Finally for sake of completeness, the FSI and the electromechanical approaches was discussed.

In this work, the adopted simulation framework was inspired by the work of Krishnamurthy et al. (Krishnamurthy et al., 2013). A 3D patient-specific finite element model of SV is coupled to a patient-specific LP model of the whole univentricular circulation in a closed-loop fashion. In the next chapter, the various parts of the model will be described in details.

Chapter 3

Multiscale model of the SV

In the present chapter, a multiscale model of single ventricle cardiac biomechanics is presented. In particular, a detailed description of each component of the model is provided separately, highlighting the role of each component in assembling the closed-loop multiscale model.

3.1 Introduction

THE patient-specific multiscale cardiovascular model consists of four main components; an anatomic model of the SV, a passive constitutive model, an active contractile model, and a closed-loop circulatory model. The anatomic model of the ventricle in turn consists of the unloaded ventricular geometry and a fibre local material coordinate system that represent the myofibre architecture. The unloaded ventricular geometry is obtained by means of an unloading algorithm, which uses the ventricular geometry segmented and fitted from MR images and pressure measurements representative of the ED condition. The ventricular geometry is modeled as a 3D hexahedral cubic-Hermite FE mesh. The boundary conditions of the model were specified to prevent displacement and rotation of the base along the long axis. The second component of the patient-specific model consists of the constitutive law for the resting myocardial material properties (Holzapfel and Ogden, 2009) along with parameters that are adjusted to match the end-diastolic pressure-volume relations of the patient. The third component of the patient-specific model is the active-contractile law (Lumens et al., 2009) that simulates muscle contraction. The parameters of this model were then adjusted to match the ventricular cavity pressures and CO measured in the patient. The fourth component is the lumped parameter closed-loop hemodynamic model that generates the boundary condition for the ventricular FE model. The patient-specific parameters of the circulation were obtained through an optimization process described elsewhere (Baretta et al., 2012).

3.2 Clinical pre-operative data

Clinical data acquisition is a crucial issue in the modelling process. Given the very young age, the particular nature of their physiology and the limitate number of patients, subjects affected by HHS represent a peculiar and challenging population. For modelling purpose, clinical data should be all collected at the same time, ensuring identical physiological conditions. However, in the daily clinical practice this is not feasible with the actual technology. Even measurements that are close in time present errors due to the equipment limitations and the constantly changing in the physiology of the patient. Moreover, clinical investigations that provide clinical data are not intended, nor designed, to develop mathematical modelling, but rather to provide guidance to the patient management. Therefore, the collaboration between clinicians and engineers of the Transatlantic Network, of which the present work is part, are important to

select those data which are considered to be more reliable.

Clinical data used in this work were collected at two different medical center involved in the project after institutional review board approval and informed consent from the subject's parents were obtained: The Medical University of South Carolina (Charleston, SC, USA) and University of Michigan Medical School, Division of Pediatric Cardiology (Ann Arbor, MI, USA). For each patient, clinical data were collected in terms of catheterization-derived pressure tracings, magnetic resonance (MR) flow tracings, MR-derived reconstruction of the SV and echocardiographic Doppler velocity tracings. Clinical measurements were performed prior to the stage 2 procedure. A pre-operative echocardiogram was performed under sedation and followed routine clinical protocols. MR was performed under general anesthesia, and flow and volume measurements were obtained in different locations. Cardiac catheterization for pre-operative testing was performed under conscious sedation, using an ECG-gated, free-breathing cine-phase contrast velocity-encoded pulse sequence and commercially available cardiac analysis software. Hemodynamic assessment with intra-cardiac and vascular pressure measurements was obtained using a fluid-filled catheter system. Figure 3.1 shows an example of MR flow, catheterization-derived pressure and Doppler velocity time tracings and a three views MRI n which the SA and the SV are denoted.

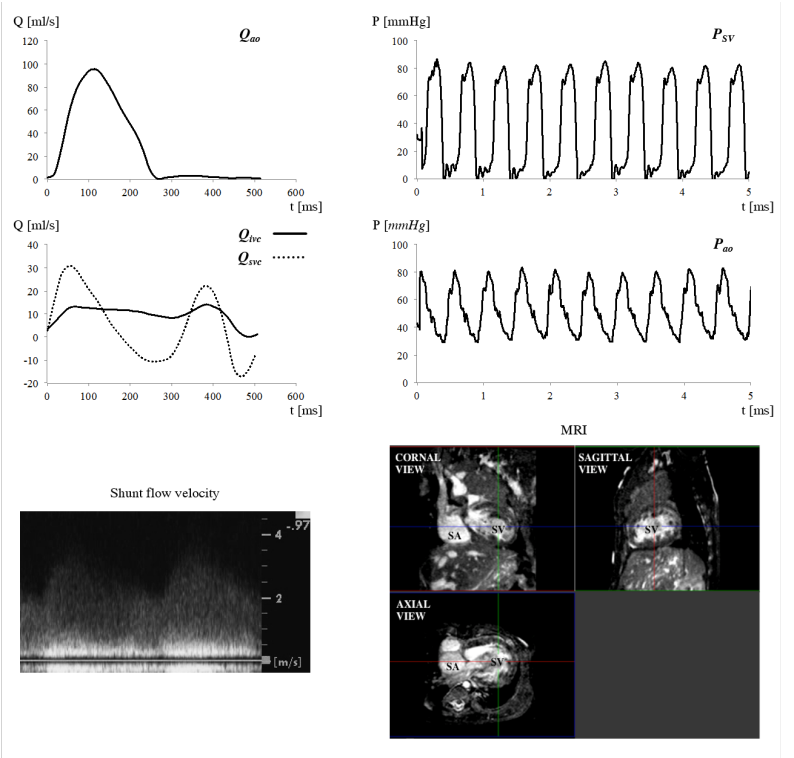

Figure 3.1 Example of clinical time tracings acquired for a SV patient and images from CMR. ao=aorta; svc=superior vena cava; ivc=inferior vena cava; SV=single ventricle; SA=single atrium.

3.3 Finite element mesh

At the basis of the structural model of ventricular mechanics is the FE mesh that describes the patient anatomy and fibre architecture. To obtain the mesh a discretization of a physical domain representing the patient ventricle is required. The sequential approach adopted in this work to obtain a SV finite-element model is described in the following subsections including, the manual segmentation of clinical images, the fitting of a template mesh to the clinical data and the inclusion of a realistic fibre orientation.

3.3.1 Single ventricle anatomy

The model of SV anatomy (right ventricle in case of HLHS and left in case of HRHS) is obtained starting from MRI of the specific paediatric patient. Images are acquired by clinician at end-diastole as defined by the peak of the R-wave. In order to distinguish between the myocardium and the surrounding tissues a manual segmentation process is performed by means of Amira®5.4.5 (FEI, Hillsboro, Oregon, USA). The reconstruction is performed based on about 50 slices equally spaced of 1 mm with respect to the ventricular long axis and with a spatial in-plane resolution of 0.25 x 0.25 mm. Figure 3.2 shows the endocardial (blue) and epicardial (red) surfaces obtained after manual segmentation of multiple slices have been performed for a patient suffering from HRHS.

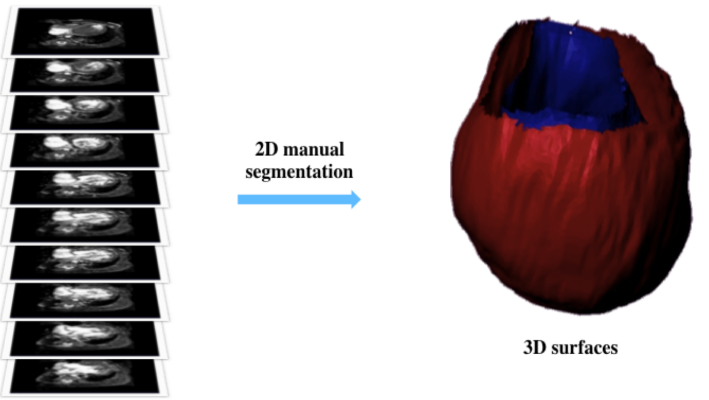

Figure 3.2 On the left, set of MR images used for the 2D manual segmentation. On the right results of the manual reconstruction. In blue the endocardial surface and in red the epicardial surfaces.

The segmentation results of each patient taken in consideration in this study was reviewed by clinician to avoid misinterpretation of the clinical images. After the check of the endocardial and the epicardial surfaces, a parametric approach is adopted to extract a number of points to be used as targets for the mesh obtainment. Equally spaced plane (2 mm) parallel to the valvular plane were defined along the whole length of the reconstructed geometry, by means of RHINOCEROS®4.0 (McNeel, Seattle, Washington, USA). Thus, multiple sections of the inner (endocardium) and outer (epicardium) wall of the myocardium are obtained. Every section is then subdivided in smaller segments to

define a proper number of reference points to be used for the subsequent phase of surface fitting (Figure 3.3).

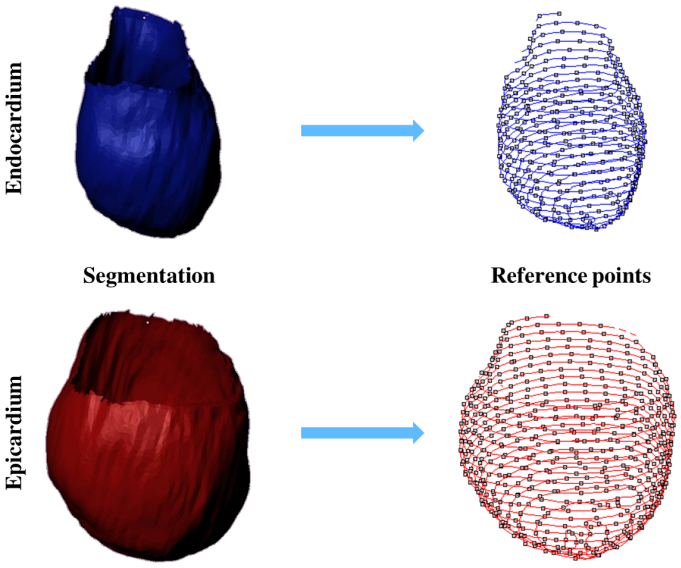

Figure 3.3 On the left, surface reconstructions of the endocardium and the epicardium of a SV patient. On the right, sections of the internal (blue) and the external surface (red) of the SV. Reference section points defined are shown for each sections.

Since the *in vivo* images were acquired at end-diastole, the reconstructed geometry required further processing after the 3D finite element mesh is obtained (see section 3.4). Indeed, to correctly compute stresses, an unloaded reference state, defined as the state at which the ventricle cavity pressure in a passive state is zero, must be identified.

3.3.2 2D surface fitting and conversion to a 3D mesh

The domain discretization of the ED geometry was performed using hexahedral cubic-Hermite FE mesh. This kind of interpolation implies as degrees of freedom both the nodal coordinate values and the nodal derivatives. Thus, geometries represented by means of Hermite interpolation guarantee C_1 continuity on the boundary between adjacent elements. This approximation yields to a smooth description of the shape, which represents a great advantage when

dealing with soft tissue simulations. To obtain the final 3D mesh of the patient a sequential approach was adopted (Figure 3.4). First, a simplified 2D cubic-Hermite template mesh (80 nodes and 64 elements) was defined in a prolate spheroidal coordinates system using Continuity 6.4 (National Biomedical Computation Resource, University of California, San Diego, CA, USA). The template consists of two nested surfaces representing the endocardial and epicardial surfaces. The template was then fitted in the radial coordinate (λ) to the reference points extracted from the patient reconstruction by a linear least squares minimization of the projection distance of the data to the interpolated mesh surfaces parameterized at the nodes. For a detailed description of the fitting method the reader is referred to (Nielsen et al., 1991). The obtained surface meshes were then converted to a 3D hexahedral cubic-Hermite elements (3 x 3 x 3 integration points) in rectangular Cartesian coordinates. In order to better define the transmural fibre orientation gradient, the mesh was refined across the myocardial wall thickness to a final resolution of 120 nodes and 64 elements. The accuracy of the results was verified by ensuring that the root mean square projection error was on the order of the spatial resolution of the image data (0.25 mm) and the LV cavity volume agreed to within 2% of the measured volume from the reconstruction.

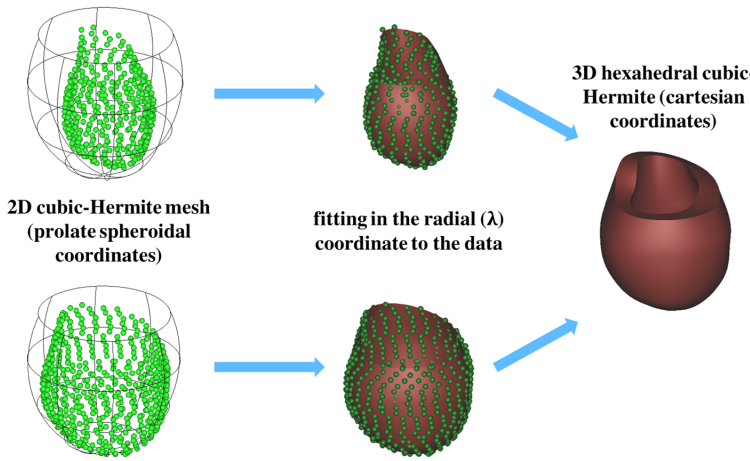

Figure 3.4 On the left, set of the MRI used for the 2D manual segmentation. On the right results of the manual reconstruction. In blue the endocardial surface and in red the epicardial surfaces.

3.3.3 Material coordinate system and fibre architecture

In the governing equations, various orthogonal coordinate systems have been used to describe the finite deformation of the ventricular model. Continuity 6.4 uses four coordinate systems: Global Rectangular Cartesian coordinates (Y_1,Y_2,Y_3); curvilinear World coordinates (Θ_1, Θ_2, Θ_3); local finite element coordinates (ξ_1, ξ_2, ξ_3); and local material coordinates (X_1, X_2, X_3). The global rectangular Cartesian reference coordinate system is defined collinear with the long axis of the ventricular cavity and with the orthogonal curvilinear coordinate systems are used to describe the geometry. The local element coordinates are used as intermediates to create a locally orthogonal body coordinate system with one axis aligned with ξ_1, one in the $\xi_1 - \xi_2$ plane and the third perpendicular to the other two. These axes are then rotated through the fibre, transverse and sheet angles to generate material coordinates coinciding with the fibre, sheet and sheet-normal directions.

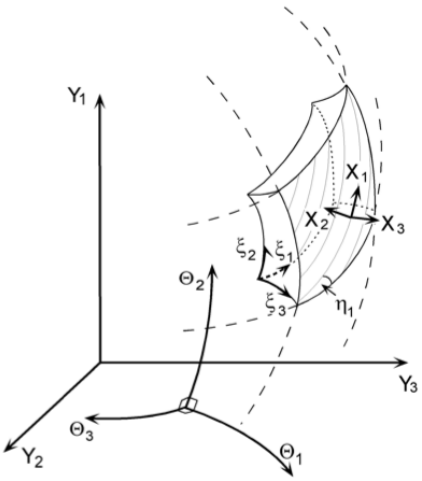

Figure 3.5 Four coordinate system are used in our finite element method. A rectangular Cartesian global reference coordinate system (Y_1,Y_2,Y_3) and orthogonal curvilinear coordinate systems (Θ_1, Θ_2, Θ_3) are used to describe the geometry. Curvilinear local finite element coordinates are (ξ_1, ξ_2, ξ_3), and locally orthonormal convecting body/fibre coordinates are (X_1, X_2, X_3) [Reprinted from (Usyk and McCulloch, 2003a) with permission by Springer].

In the fitting phase (described in section 3.3.2), a prolate spheroidal coordinate system (λ, μ, θ) rather than rectangular cartesian coordinates was used

because the prolate spheroid provides a good initial approximation to ventricular boundary geometry and therefore reduces the required number of nodal parameters (Figure 3.6).

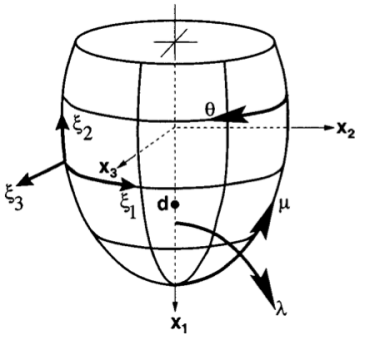

Figure 3.6 Schematic diagram of the rectangular Cartesian model coordinate system (X_1, X_2, X_3) collinear with the long axis of the ventricular cavity. The prolate spheroidal coordinate system (λ, μ, θ) is convenient for modeling cardiac geometry. The curvilinear parametric coordinates curvilinear coordinate systems (Θ_1, Θ_2, Θ_3) are used to describe the geometry. Curvilinear local finite element coordinates are the local finite element coordinates [Reprinted from (Vetter and McCulloch, 2000) with permission by Springer].

To model the muscle fibre orientations, it is assumed here that the fibres lie in the $\xi_1 - \xi_2$ coordinate planes so that they are tangential to the endocardial and epicardial surfaces. Hence, the fibre angle is defined with respect to the ξ_1 coordinate. The fibre angle at any point in the model is given by an interpolation of fibre field parameters defined at the same nodal positions used to define the ventricular geometry. The measured transmural distribution of fibre and sheet angles were approximated using trilinear Lagrange basis functions. As specific information on the patient-specific fibre orientation were not available, fibre architecture was assumed as in physiological adult ventricles.

Concerning boundary constraints, the 3D model was subjected to proper kinematic boundary conditions to prevent rigid body movements. To constrain the motion of the model displacement and rotation of the base along the long axis are set to zero, while the rest of the ventricle is left free to move. This constraints are applied to the ventricular model in all the simulations performed with the 3D in both the stand alone and the multiscale conditions.

3.4 Passive material model and unloaded geometry

The passive material properties of the myocardium were described using the transversely isotropic form of the Holzapfel constitutive model (Holzapfel and Ogden, 2009). If the myocardium is described as an incompressible medium with only one family of fibres perfectly aligned along their mean direction, the strain energy function includes two exponential terms, one accounting for the isotropic matrix and one for the anisotropy of the fibres. Two material parameters had to be estimated to reproduce a patient-specific behaviour of the passive ventricle. The in vivo MR images are necessarily obtained in a loaded configuration of the heart often end-diastole, as defined by the peak of the R-wave. However, to compute stresses in a correct way, the unloaded reference state is required. This unloaded geometry, when loaded to the measured ED pressure, will deform to the measured end-diastolic geometry. This, in turn, depends on the material properties used for the description of the mechanical behaviour of the myocardium. Thus, the myocardial passive material parameters were estimated together with the identification of the unloaded geometry. To this aim, an iterative method previously developed by Krishnamurthy et al. (Krishnamurthy et al., 2013) was adopted. This unloading algorithm allows to estimate the unloaded geometry on the basis of the ED ventricular model, if the ED pressure (measured) and the unloaded volume (assumed) were known, while the passive material parameters were iteratively tuned.

3.4.1 Passive constitutive model

To describe the constitutive law assumed in this work for the description of the resting myocardial properties a brief remind to the basic equations of continuum mechanics is carried out. The basic deformation variable for the description of the local kinematics is the deformation gradient $\mathbf{F}$, with the standard notation and convention:

$$J = \det \mathbf{F} > 0 \tag{3.1}$$

For an incompressible material, there is the constraint

$$J = \det \mathbf{F} \equiv 1. \tag{3.2}$$

Associated with $\mathbf{F}$ are the right and left Cauchy-Green deformation tensors, defined by

$$\mathbf{C} = \mathbf{F}^{\mathrm{T}}\mathbf{F} \text{ and } \mathbf{B} = \mathbf{F}\mathbf{F}^{T} \tag{3.3}$$

respectively. Also important for what follows is the Green-Lagrange (or Green) strain tensor, defined by

$$\mathbf{E} = \frac{1}{2}(\mathbf{C} - \mathbf{I}) \tag{3.4}$$

where $\mathbf{I}$ is the identity tensor. The principal invariants of $\mathbf{C}$ (and also of $\mathbf{B}$) are defined by

$$I_1 = \operatorname{tr}\mathbf{C}, \quad I_2 = \frac{1}{2}\left[I_2 - \operatorname{tr}\left(\mathbf{C}^2\right)\right] \text{ and } I_3 = \det\mathbf{C} \tag{3.5}$$

with $I_3 = J^2 = 1$ for an incompressible material. These are isotropic invariants. For more details of the relevant material from continuum mechanics, the reader is referred to Holzapfel (Holzapfel, 2000) and Ogden (Ogden, 1997).

If the material has a preferred direction in the reference configuration, denoted by the unit vector $\mathbf{a}_0$, this introduces anisotropy, specifically transverse isotropy, and with it comes two additional (transversely isotropic) invariants (or quasi-invariants) defined by

$$I_4 = \mathbf{a}_0 \cdot (\mathbf{C}\mathbf{a}_0) \text{ and } I_5 = \mathbf{a}_0 \cdot \left(\mathbf{C}^2\mathbf{a}_0\right) \tag{3.6}$$

Note that these are unaffected by reversal of the direction of $\mathbf{a}_0$. If one wishes to distinguish between the directions $\mathbf{a}_0$ and $-\mathbf{a}_0$ as far as the material response is concerned, then yet another invariant would be needed. Here, however, we do not consider this possibility.

In this description the material properties are expressed by a strain-energy function $\boldsymbol{\Psi}$, which is measured per unit reference volume. This depends on the deformation gradient $\mathbf{F}$ through $\mathbf{C}$ (equivalently through $\mathbf{E}$), which ensures objectivity. For such an elastic material, the Cauchy stress tensor $\boldsymbol{\sigma}$ is given by the formulae

$$J\boldsymbol{\sigma} = \mathbf{F}\frac{\partial\boldsymbol{\Psi}}{\partial\mathbf{F}} = \mathbf{F}\frac{\partial\boldsymbol{\Psi}}{\partial\mathbf{E}}\mathbf{F}^{T} \tag{3.7}$$

for a compressible material (for $\boldsymbol{\Psi}$ treated as a function of $\mathbf{F}$ and $\mathbf{E}$, respectively), which are modified to

$$\boldsymbol{\sigma} = \mathbf{F}\frac{\partial\boldsymbol{\Psi}}{\partial\mathbf{F}} - p\mathbf{I} = \mathbf{F}\frac{\partial\boldsymbol{\Psi}}{\partial\mathbf{E}}\mathbf{F}^{T} - p\mathbf{I} \tag{3.8}$$

for an incompressible material, in which case is valid the constraint $J = 1$ (equivalently $I_3 = J^2 = 1$) and this is accommodated in the expression for the stress by the Lagrange multiplier p.

For an elastic material possessing a strain-energy function $\mathbf{\Psi}$ that depends on a list of invariants, say I_1, I_2, . . . , I_N, for some N, equations 3.7 and 3.8 may be expanded in the forms

$$J\boldsymbol{\sigma} = \mathbf{F}\sum_{i=1}^{N}\psi_i\frac{\partial I_i}{\partial \mathbf{F}} \text{ and } \boldsymbol{\sigma} = \mathbf{F}\sum_{i=1,i\neq 3}^{N}\psi_i\frac{\partial I_i}{\partial \mathbf{F}} - p\mathbf{I} \tag{3.9}$$

respectively, where the following notation has introduced

$$\psi_i = \frac{\partial \mathbf{\Psi}}{\partial I_i}, \quad i = 1, 2, ..., N, \tag{3.10}$$

with $i = 3$ omitted from the summation for the incompressible material and I_3 omitted from the list of invariants in $\mathbf{\Psi}$ in this case. Note that $\partial I_i/\partial \mathbf{F} = (\partial I_i/\partial \mathbf{E})\,\mathbf{F}^T$ in terms of the Green-Lagrange strain tensor. Note that the second Piola-Kirchhoff stress tensor $\mathbf{S}$ is given in terms of the Cauchy stress tensor via the simple formula $\mathbf{S} = J\mathbf{F}^{-1}\boldsymbol{\sigma}\mathbf{F}^{-T}$, using equation 3.7 for a compressible material and using equation 3.8 for an incompressible material with $J = 1$. Explicitly, with $\mathbf{E}$ as the independent variable, we have simply

$$\mathbf{S} = \frac{\partial \mathbf{\Psi}}{\partial \mathbf{E}} \text{ and } \mathbf{S} = \frac{\partial \mathbf{\Psi}}{\partial \mathbf{E}} - p\left(\mathbf{I} + 2\mathbf{E}\right)^{-1} \tag{3.11}$$

for compressible and incompressible materials, respectively.

In this work the transversely-isotropic form of the constitutive model developed by Holzapfel and Ogden (Holzapfel and Ogden, 2009) was assumed to model the passive properties of the resting myocardium. In this model, the anisotropy in the fibre and cross-fibre directions of the myocardium has been accounted using separate exponential terms with different exponents. Equation 3.12 gives the equation for the strain energy.

$$\mathbf{\Psi} = \frac{a}{2b}e^{b(I_1-3)} + \frac{a_f}{2b_f}(e^{b_f(I_{4f}-1)} - 1) \tag{3.12}$$

where a, b, a_f, b_f are material constants, the a parameters having dimension of stress, whereas the b parameters are dimensionless. I_1 is the first invariant of the right Cauchy-Green strain tensor (isotropic term), I_{4f} are the components of the right Cauchy-Green strain tensor in the fibre direction (transversely isotropic term). The parameters of the model were fitted to match the biaxial tests of Yin

et al. (Yin et al., 1987) and the shear tests of Dokos et al. (Dokos et al., 2002) of *ex-vivo* canine myocardial tissue and are reported in Table 3.1.

Table 3.1 Default parameters of the Holzapfel passive constitutive law.

Symbol	Unit	Value
a	kPa	2.28
b	-	9.726
a_f	kPa	1.685
b_f	-	15.779

The default parameters of the transversely-isotropic model resulted in extremely stiff stress-strain relations in the patient-specific models. Hence, the pressure scaling parameters (a, a_f) were scaled uniformly to fit the end-diastolic pressure and volume in the patient-specific models. If the default parameters were still too non-linear for some patient-specific models, the exponential parameters (b, b_f) were slightly altered.

3.4.2 Unloading algorithm

Anatomical models reconstructed from *in vivo* images are obtained in a loaded configuration, thus to compute stresses correctly an unloaded reference state is required. In their work, Krishnamurthy et al. (Krishnamurthy et al., 2013) proposed an unloading algorithm, that is able to compute an unloaded geometry given the ED geometry, the ED pressure, a set of material properties and fibre orientation and an estimation of the unloaded volume (V_{SV0}). Since, the MRIs of the patients taken in to account in this work are taken at end-diastole and ED pressure is measured clinically, in this work the same unloading algorithm is adopted.

The unloading algorithm is based on the multiplicative decomposition of the deformation gradient tensor $\mathbf{F}$, as described in tissue growth modelling (Rodriguez et al., 1994). The iterative estimation scheme aimed at finding the unloaded reference geometry that minimized the difference between the measured ED geometry and the computed geometry when the unloaded model was inflated to the measured ED pressure, given nonlinear myocardial material properties. Thus, given a set of material parameters, an unloaded geometry is calculated that when inflated to ED pressure, results in a loaded geometry that is the same as the mesh fitted to the ED state to within acceptable error limits.

As shown in Figure 3.7, the fitted ED mesh is assumed as an initial guess for the unloaded state $\mathbf{X_0}$. This model is then inflated to the ED pressure to obtain the geometry $\mathbf{Y_0}$. The inverse of the deformation gradient $\mathbf{F_{YY0}}$ between $\mathbf{Y_0}$ and the fitted ED geometry $\mathbf{Y}$, is then calculated and applied to the initial guess, $\mathbf{X_0}$, to obtain a new estimate of the unloaded geometry $\mathbf{X_1} = [\mathbf{F_{YY0}}]^{-1}\,\mathbf{X_0}$. This process is iterated until the loaded geometry and the fitted ED geometries matched the measurement accuracy of the diastolic geometry.

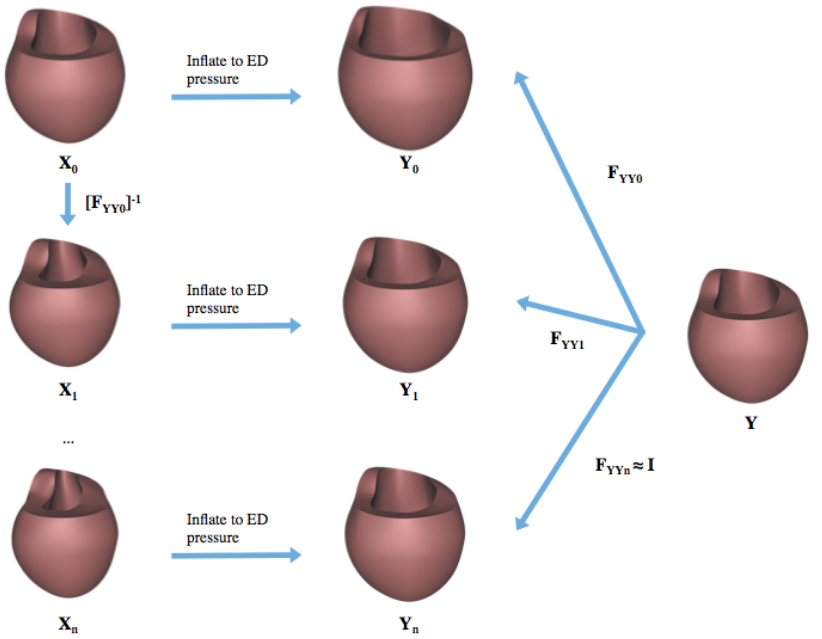

Figure 3.7 Algorithm to find the unloaded geometry. The initial geometry, $\mathbf{X_0}$, is first inflated to the measured ED pressure. The deformation gradient between the inflated mesh ($\mathbf{Y_0}$) and the fitted ED ($\mathbf{Y}$) is then computed. This deformation gradient is then applied inversely to the initial estimate to get a new unloaded geometry estimate. This process is iterated until the projection error between the surfaces of the measured and loaded geometries is lower than the fitting error.

The fundamental step of this procedure is to apply inversely the deformation gradient tensor to get the estimate of the unloaded geometry that is consistent with respect to the nodal positions of the initial geometry. However, applying this operation in a single step is not possible due to the large changes in the

nodal coordinates. Thus, the deformation gradient tensor is decomposed in a linear way and applied in subsequent steps to the estimated geometry to obtain the unloaded geometry.

$$\left[\mathbf{F_{YYi}}\right]_k^{-1} = k\left[\mathbf{F_{YYi}}\right]^{-1} + (1-k)\,\mathbf{I} \tag{3.13}$$

Starting from the estimated geometry $\mathbf{X_i}$, $\left[\mathbf{F_{YYi}}\right]^{-1}$ is applied to obtain a new estimated unloaded geometry $\mathbf{X_{i+1}}$. This operation is carried out by decomposing $\left[\mathbf{F_{YYi}}\right]^{-1}$ linearly with $\mathbf{I}$, starting with $\left[\mathbf{F_{YYi}}\right]_k^{-1}$, given by Equation 3.13 and $k = 0$. Then k is incremented to a little value and the resulting deformation gradient is used to compute the stress in the geometry. The equilibrium solution for the position of the nodes that will reduce this stress to zero is then obtained. The value of k is then incremented and the process is repeated until the final unloaded geometry is obtained at $k = 1$.

In the work of Krishnamurthy et al. (Krishnamurthy et al., 2013), the estimation of the unloaded volume was based on an empirical relation proposed by Klotz and co-workers (Klotz et al., 2006), that proposed a mathematical relation to calculate the unloaded volume as a function of the ED pressure and volume. This relation was found to correlate well with measurements in human adults and animal hearts in healthy and disease conditions.

$$V_0 = (0.6 - 0.006P_m)\,V_m \tag{3.14}$$

Klotz et al. (Klotz et al., 2006) found this relation proposing a standardized volume normalization of the ED pressure-volume relation that eliminates most of the variation between individuals (including heart disease patients) and across species. They showed that the volume-normalized ED pressure-volume relation can be approximated by a power law expression for both normal and a pathological subjects. However, this relation applied to paediatric patients provided unrealistic results (i.e. unloaded volumes always larger than end-systolic volume), thus suggesting that this relation is not suitable for SV patients. Among the data available in the Transatlantic Network of which this project is part, for some Stage 1 (not the same patients chose in this study) patients pressure-volume loops (PVLs) were measured. From the PVLs is then possible to extract a reliable estimation of the ED pressure-volume relation. Following the approach proposed in the work by Klotz et al. (Klotz et al., 2006) the following relation is found

$$V_0 = (0.5738 - 0.0225P_m)\,V_m \tag{3.15}$$

and used to scale the resting material parameters so that the SV cavity volume of the unloaded model matches the estimated unloaded volume. In the algorithm, if the computed unloaded volume is smaller than the estimated volume, the material stiffness is increased, otherwise the material stiffness is decreased.

3.5 Active contraction model

The active contraction model of myocardial fibres proposed by Lumens et al. (Lumens et al., 2009) was adopted in this study. In this model, the sarcomere is modeled as a passive element in parallel with a series of a contractile element and an elastic element. The myofibre strain is converted to sarcomere length L_S by

$$L_S = L_{S,ref}\sqrt{C\,[0,0]} \tag{3.16}$$

where $L_{S,ref}$ is the reference sarcomere length at zero strain and $C\,[0,0]$ is the component in the fibre direction of the right Cauchy-Green deformation tensor. The active tension generated by the sarcomere is defined as:

$$T_{act} = s_{act}C\left(L_{SC} - L_{SC0}\right)\frac{L_S - L_{SC}}{L_{SC,iso}} \tag{3.17}$$

where s_{act} is a factor scaling the active myofibre stress, C the mechanical activation, L_{SC} the contractile element length, L_{SC0} the contractile element length with zero load and $L_{SC,iso}$ the length of isometrically stressed elastic element. The active tension depends on two state variables (i.e., the contractile element length L_{SC} and the mechanical activation C). The time derivative of L_{SC} can be written as:

$$\frac{dL_{SC}}{dt} = \left(\frac{L_S - L_{SC}}{L_{SC,iso}} - 1\right)v_{max} \tag{3.18}$$

where v_{max} represents sarcomere shortening velocity with zero load. The time derivative of C is:

$$\frac{dC}{dt} = \frac{1}{\tau_R}C_L\left(L_{SC}\right)F_R\left(t\right) + \frac{1}{\tau_D}\left(\frac{C_{rest} - C}{1 + e^{(T(L_{SC}) - t)/\tau_D}}\right) \tag{3.19}$$

where τ_R and τ_D are scaling rise and decay time, respectively, t and C_{rest} represent time and diastolic resting level of activation, respectively, and C_L, F_R and T are functions describing the increase of activation with the sarcomere

length, the rise of mechanical activation and the decrease of activation duration with decrease of sarcomere length, respectively:

$$C_L\left(L_{SC}\right) = \tanh\left(4.0\left(L_{SC} - L_{SC0}\right)^2\right) \tag{3.20}$$

$$F_R\left(t\right) = 0.02\, x^3\left(8 - x\right)^2 e^{-x} \tag{3.21}$$

$$T\left(L_{SC}\right) = \tau_{SC}\left(0.29 + 0.3 L_{SC}\right) \tag{3.22}$$

The active tension is then used to define the active stress tensor $\mathbf{S}_{\text{active}}$ added to the second Piola-Kirchoff stress tensor $\mathbf{S}$ (defined in subsection 3.4.1) to account for the contribution of fibre contraction:

$$\mathbf{S}_{\text{tot}} = \mathbf{S} + \mathbf{S}_{\text{active}} \tag{3.23}$$

The default parameter of active contractile model are reported in Table 4.9

Table 3.2 Default parameters of the active contractile constitutive model

Symbol	Unit	Value	Parameter description
C_{rest}	-	0.02	Diastolic resting level of activation
L_{SC0}	μm	1.51	Contractile element length at zero active stress
$L_{S,ref}$	μm	1.85	Reference sarcomere length at zero strain
v_{max}	μm/s	10	Sarcomere shortening velocity with zero load
τ_D	ms	42	Factor scaling contraction decay time
τ_R	ms	42	Factor scaling contraction rise time
τ_{SC}	ms	300	Factor scaling duration of contraction
s_{act}	kPa	300	Factor scaling active myofibre tension

3.6 Circulatory model

The lumped-parameter closed-loop hemodynamic model has been adopted in this work to accomplish two main tasks. First, the LP model is used in a fully LP description (i.e. even the ventricle is described with a lumped parameter approach) to perform the patient-specific parameter identification of the circulatory parameters. The use of a LP of the SV model was mandatory in this step to obtain parameter estimation with a reasonable computational effort.

Second, the LP model is used to generate the proper hemodynamic boundary condition for the ventricular FE model to simulate both pre- and post-operative conditions.

Two LP models of the circulation were developed corresponding to stage 1 and stage 2 of the Fontan surgical procedures. The cardio-circulatory layout of the stage 1 circulation is depicted in Figure 3.8.

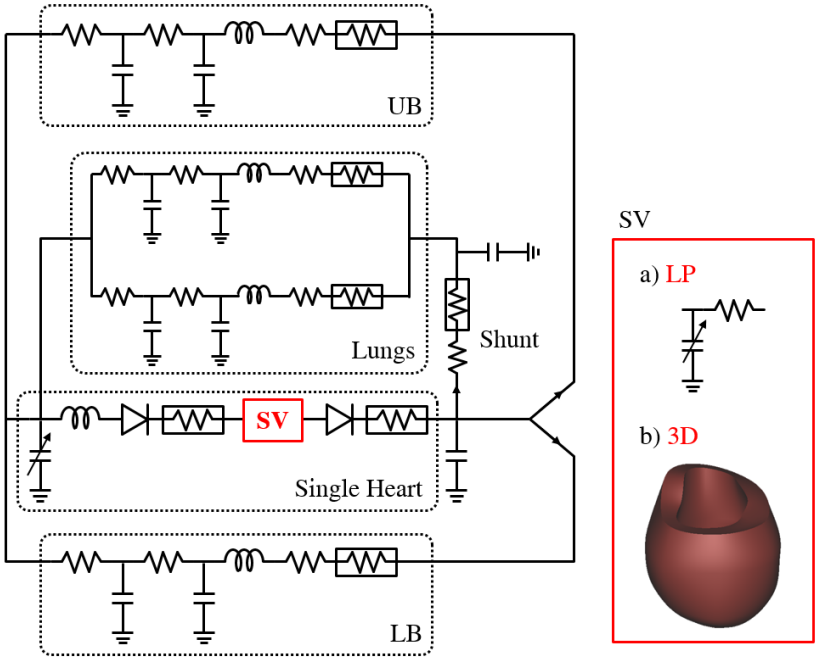

Figure 3.8 Patient-specific biomechanical model for stage 1 SV circulation. The circulatory layout of stage 1 comprised the single heart, the systemic upper body (UB), lower body (LB) and lungs circulations and the shunt. The single ventricle was modelled as a time-varying elastance in series with a linear resistance for the LP model (red box a)) to perform parameters identification. To obtain the multiscale model the LP model of the SV was replaced by the ventricular FE model (red box b)).

The hemodynamic model comprised four main blocks to model the single heart, the systemic upper (UB) and lower (LB) body circulations and the lungs. A resistive block mimicking the systemic-to-pulmonary shunt was added. For the sake of simplicity and in the absence of any clinical information, coronary circulation, gravity and respiratory effects were neglected in the present case study.

In the following subsections a detailed description of the general equations governing the LP circulatory model is reported.

3.6.1 Cardiac chambers

Single-atrium and single-ventricle were described by means of time-varying elastances accounting for the active and the passive behaviour of the myocardium. The pressure generated by a generic chamber $P_{ch}(t)$ was defined as:

$$P_{ch}(t) = P_{ch-active}(V_{ch}, t)A_{ch}(t) + P_{ch-passive}(V_{ch}, t) + R_{myo}\frac{dV_{ch}}{dt} \quad (3.24)$$

where ch = SV, SA indicates the single-ventricle and the single-atrium. The viscous term R_{myo} was considered only for the ventricle. Ventricular active pressure-volume relationship was considered non-linear while a linear relation was considered for the atrium. Both atrial and ventricular passive pressure-volume relationships were described with a non-linear relation. The following equations were used:

$$P_{SV-active}(V_{SV}, t) = a(V_{SV}(t) - V_{SV0}) + b(V_{SV}(t) - V_{SV0})^2 \quad (3.25)$$

$$P_{SV-passive}(V_{SV}, t) = c_{SV}(e^{(d_{SV}V_{SV}(t) - V_{SV0})} - 1) \quad (3.26)$$

$$P_{SA-active}(V_{SA}, t) = \frac{1}{C_{SA}}(V_{SA}(t) - V_{SA0}) \quad (3.27)$$

$$P_{SA-passive}(V_{SA}, t) = c_{SA}e^{(d_{SA}(V_{SA}(t) - V_{SA0}) - 1)} \quad (3.28)$$

where V_{SV0} and V_{SA0} are the unstressed volumes of each cardiac chamber (i.e., the volume at zero pressure), a, b, c_{SV} and d_{SV} are model parameters specific to the single-ventricle while C_{SA}, c_{SA} and d_{SA} are model parameters specific to the single atrium. In Figure 3.9, the typical pressure-volume curves for both SV and SA are depicted.

The term $A_{ch}(t)$ in equation 3.24 ranges from 0 during diastole and 1 at the peak of systole. It describes the excitation-relaxation pattern of the sarcomeres and is defined as:

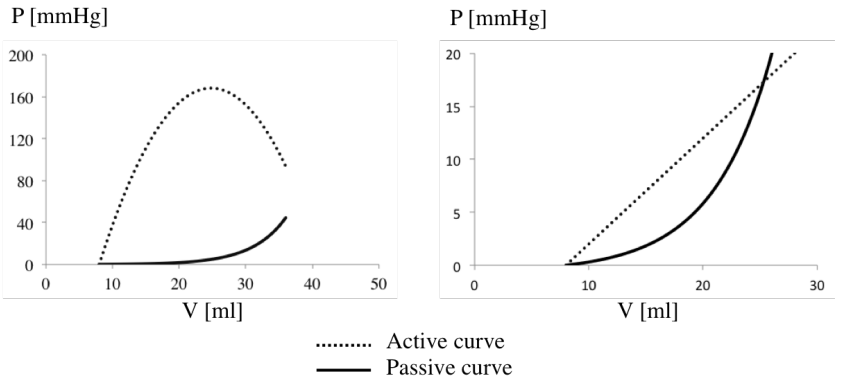

Figure 3.9 Typical ventricular (left) and atrial (right) active (continuos line) and passive (dashed line) curves used in the 0D model of Stage 1 patients.

$$A_{SV} = \begin{cases} 0.5\,[1 - cos(2\pi t/t_s)] & \text{if} \quad t < t_s \\ 0 & \text{otherwise} \end{cases} \tag{3.29}$$

$$A_{SA} = \begin{cases} 0.5\left[1 - cos\left(\frac{2\pi(t-\Delta t)}{t_{sa}}\right)\right] & \text{if} \quad t < t_{sa} \\ 0 & \text{otherwise} \end{cases} \tag{3.30}$$

where t_s and t_{sa} are atrial and ventricular systole durations (Figure 3.10).

Values of atrial and ventricular contraction durations and of the time lapse when atrial and ventricular activation functions overlap were calculated according to the equations below as functions of the total cycle length (t_c), by means of time ratios $t_{s,r}$, $t_{sa,r}$ and $t_{1,r}$.

$$t_s = t_{s,r}\sqrt{t_c} \tag{3.31}$$

$$t_{sa} = t_{sa,r}\sqrt{t_c} \tag{3.32}$$

$$t_1 = t_{1,r}\sqrt{t_c} \tag{3.33}$$

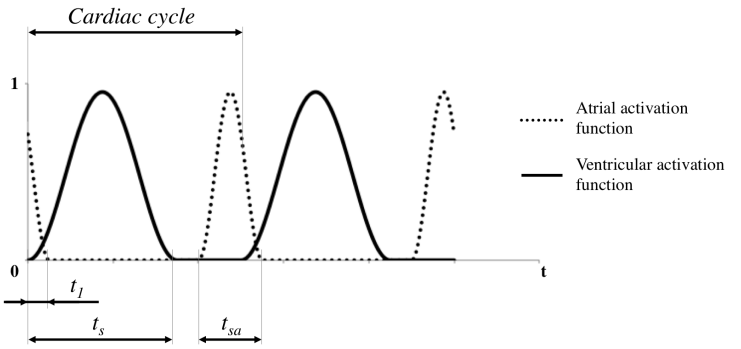

Figure 3.10 Atrial and ventricular activation functions, shifted in time. t_s = ventricular systole duration, t_{sa} = atrial systole duration t_1 = time shifting of the atrial activation.

Time ratios $t_{s,r}$ and $t_{sa,r}$ were identified in a range centered on values derived from literature (Gemignani et al., 2008; Katz and Feil, 1923; Ursino, 1998). Time ratio $t_{1,r}$ was bound to assume values between 0.01 and 0.15 (i.e. cardiac chambers contraction overlapping between 0% and 15% t_c).

3.6.2 Valves

The aortic valve was described by means of diode with non-linear resistance K_{ao}. The pressure drop across the valve was calculated based on:

$$P_{SV} - P_{ao} = R_{myo}Q_{ao} + K_{ao}Q_{ao}^2 \tag{3.34}$$

where P_{SV} is the SV pressure, P_{ao} and Q_{ao} represent the pressure downstream and the flow across the valve respectively. R_{myo} is a term accounting for the viscous behaviour of the myocardium and K_{ao} in the non-linear resistance of the valve. The flow across the valve was then ruled by the following equations:

$$Q_{ao} = \begin{cases} \frac{R_{myo}\sqrt{4K_{ao}(P_{SV}-P_{ao})-R_{myo}}}{2K_{ao}} & \text{if} \quad P_{SV} > P_{ao} \\ 0 & \text{if} \quad P_{SV} < P_{ao} \end{cases} \tag{3.35}$$

The atrio-ventricular valve was modelled as a diode with non-linear resistance in series with an inertance. The pressure drop across the valve was:

$$P_{SA} - P_{SV} = L_{AV}\left(\frac{dQ_{AV}}{dt}\right) + K_{AV}Q_{AV}^2 \tag{3.36}$$

where P_{SA} is the pressure in the single atrium, L_{AV} and K_{AV} are the atrio-ventricular inertance and non-linear resistance and Q_{AV} is the atrio-ventricular flow.The flow across the valve was defined as follows:

$$Q_{AV} = 0 \qquad \text{if} \qquad Q_{AV} < 0$$

$$\frac{dQ_{AV}}{dt} = \begin{cases} 0 & \text{if} \quad P_{SA} > P_{SV} \text{ and } Q_{AV} \leqslant 0 \\ \frac{P_{SA} - Q_{AV}^2 K_{AV} - P_{SV}}{L_{AV}} & \text{elsewhere} \end{cases} \tag{3.37}$$

Figure 3.11 shows the schematic of the two valve models.

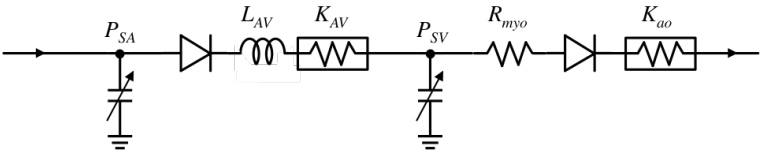

Figure 3.11 Schematics of the valve models, including the single atrium (SA), the single ventricle (SV), the viscous resistance of the myocardium R_{myo}, and the two cardiac valves described by non-linear diodes. The atrio-ventricular valve is described by the non-linear resistance K_{AV} in series with the inertance L_{AV}. The aortic valve is described by the non-linear resistance K_{ao}.

3.6.3 Vascular blocks

All the circulatory blocks (UB and LB circulations, right and left pulmonary circulations) were described by means of RLC-R-CR blocks (Figure 3.12).
The following equations (one algebraic and two differential) were used to describe the blood pressure and volume.

$$Q = (P_{up} - P_{dw})/R \tag{3.38}$$

$$\frac{dP_{dw}}{dt} = (Q_{up} - Q_{dw})/C \tag{3.39}$$

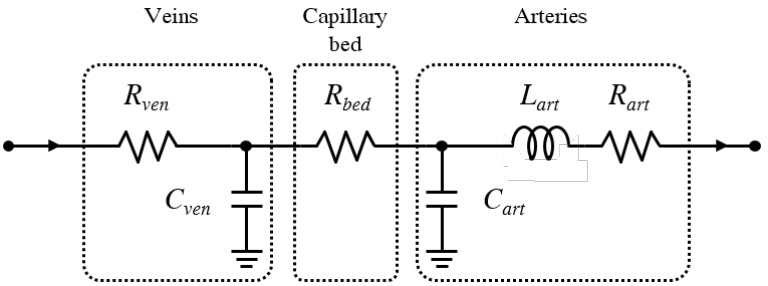

Figure 3.12 RLC-R-CR block with subdivision of resistive components: arterial resistance R_{art}, arterial inertance L_{art}, capillary bed resistance R_{bed}, venous resistance R_{ven}; arterial compliance C_{art} and venous compliance C_{ven}.

$$\frac{dQ}{dt} = (P_{up} - P_{dw} - RQ)/L \tag{3.40}$$

In the equations R, C and L refer, respectively, to the generic resistance, compliance and inertance of each vascular block. The terms P_{up}, P_{dw}, Q_{up} and Q_{dw} represent the generic pressures (P) and volumes (Q) upstream and downstream from each component. For each patient, patient-specific right and left pulmonary vascular resistances (RPVR, LPVR) and upper and lower body systemic vascular resistances (UBSVR, LBSVR) were calculated. Based on the mean values of clinical flows and pressures collected the following expression were used:

$$RPVR = \frac{P_{PA} - P_{SA}}{Q_{P-R}} \tag{3.41}$$

$$LPVR = \frac{P_{PA} - P_{SA}}{Q_{P-L}} \tag{3.42}$$

$$UBSVR = \frac{P_{ao} - P_{SA}}{Q_{UB}} \tag{3.43}$$

$$LBSVR = \frac{P_{ao} - P_{SA}}{Q_{LB}} \tag{3.44}$$

where P_{PA}, P_{SA} and P_{ao} represent the main pulmonary artery pressure, the atrial pressure and the aortic arch pressure, respectively. Q_{P-R} and Q_{P-R} are the right and left pulmonary flows, Q_{UB} and Q_{LB} are the upper body and lower body systemic flows.

3.6.4 Shunt

In the stage 1 circulation, a resistive block mimicking the systemic-to-pulmonary shunt was added, including linear and non-linear components accounting for both distributed and localized energy dissipations. To model the shunt the following mathematical equation is used:

$$\Delta P = R_{sh}Q + K_{sh}Q^2 \tag{3.45}$$

Shunt parameters were expressed as functions of the shunt diameter D_{sh} as described in Migliavacca et al. (Migliavacca et al., 2001).

$$R_{sh} = \frac{k_1}{D_{sh}^4} \tag{3.46}$$

$$K_{sh} = \frac{k_2}{D_{sh}^4} \tag{3.47}$$

Thus the flow through the shunt is calculated as:

$$Q_{sh} = \frac{\sqrt{R_{sh}^2 + 4K_{sh}\left(P_{ao} - P_{pa}\right)}}{2K_{sh}} \tag{3.48}$$

3.7 Estimation of patient-specific parameters

A key issue in the development of the multiscale model is the estimation of both the patient-specific SV mechanical properties and the circulatory parameters. To this aim, a sequential approach was carried out in this study (Figure 3.13).

The parameter estimation of the cardio-circulatory model was performed by means of a fully LP closed-loop model (step 1, Figure 3.13). The patient-specific parameters of the cardio-circulatory model were obtained through an optimization process described elsewhere (Baretta, 2014). Briefly, a Bayesian estimation of the parameters was performed. Adaptive Markov chain Monte Carlo was employed to obtain the distributions of the model parameters. Then, Nelder-Mead hill-climb optimization was performed from the parameter set that was found to maximize the posterior distribution during the Markov chain Monte Carlo iterations. Optimization was performed to find the patient-specific parameters that best replicated the clinical pre-operatory haemodynamics of the patient in terms of mean, maximum and minimum values of pressures, flows and cardiac volumes. In this phase, the use of a fully LP model to estimate

patient-specific circulatory parameters was mandatory to dramatically reduce the computational effort.

Then, the SV material parameters and the unloaded reference configuration were identified using the stand-alone ventricular FE model of the SV (step 2, Figure 3.13). The unloaded reference state and the myocardial passive properties were identified by means of the unloading algorithm described in section 3.4. Starting from the default parameters of the passive constitutive law, the algorithm is able to find an unloaded reference configuration that when inflated to the ED pressure gives the ED geometry. At this point, if the unloaded volume correspond to the V_0 estimated with equation 3.15 the unloaded reference state has been found, otherwise the material parameters are altered and algorithm run again until the unloaded volume agreed within 5% of the estimated volume. Then, the 3D finite-element model is inflated to different volumes and isovolumic contraction is simulated, iteratively tuning the active myocardial parameters in order to resemble the active ventricular elastances obtained from the fully LP optimized model.

Finally, a fine tuning of the active parameters is performed after coupling the 3D model to the LP model of circulation (step 3, Figure 3.13), thus closing the loop, to properly simulate ES volume, CO and systolic peak pressure. The results previously obtained from the fully LP model were used as the initial conditions for the multiscale model to obtain a faster achievement of a steady solution.

The optimization process and the fully LP closed-loop circulatory model were carried out in Matlab (The MathWorks, Inc., Natick, MA), whereas the FE simulations were performed using Continuity 6.4 (National Biomedical Computation Resource, University of California, San Diego, CA).

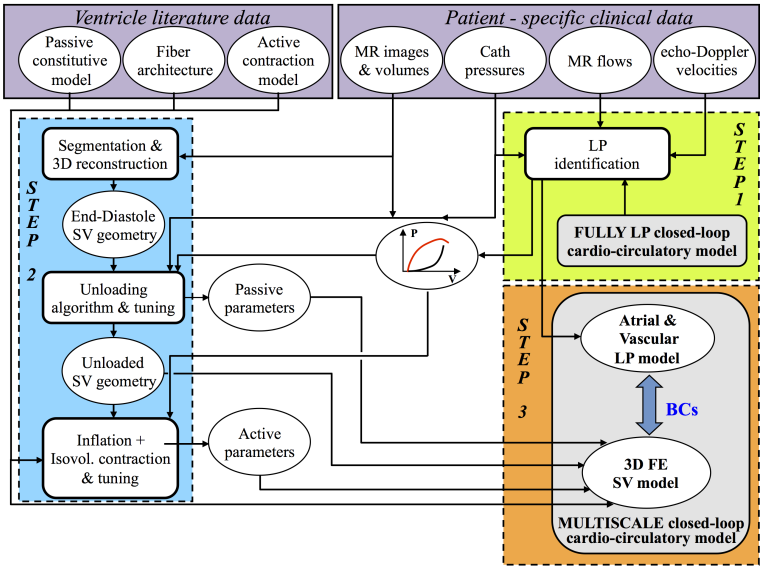

Figure 3.13 Workflow of the sequential approach adopted in this study. The parameter estimation of the cardio-circulatory model was performed by means of a fully LP closed-loop model (step 1, green box). The 3D ventricular geometry of the patient was reconstructed from MRI and the myocardial parameters (passive and active models and unloaded geometry) were estimated considering the stand-alone 3D FE model of SV (step 2, blue box). A multiscale closed-loop cardio-circulatory model was created by coupling the LP circulatory model to the 3D FE model (step 3, orange box). Literature information combined with patient-specific clinical data were used during step 1 and step 2 (violet box) [Reprinted from (Meoli et al., 2015) with permission by The Royal Society].

3.8 Conclusions

In this Chapter the patient-specific multiscale cardiovascular model adopted in this work is presented. The model is composed by four main components; an anatomic model of the SV, a passive constitutive model, an active contractile model, and a closed-loop circulatory model.

The anatomic model is modeled as a 3D hexahedral cubic-Hermite FE mesh obtained starting from reconstruction of MR images by means of surface fitting (Nielsen et al., 1991). The myofibre architecture is assumed, depending on the functional ventricle, since patient-specific data are not available. Since images

taken *in vivo* are taken in a loaded configuration (i.e. the end of the diastolic phase). An unloaded geometry is required to compute correct stresses in the myocardial wall. The unloaded ventricular geometry is obtained by means of an unloading algorithm, which uses the ventricular geometry segmented and fitted from MR images and pressure measurements representative of the ED condition (Krishnamurthy et al., 2013).

The mechanical function of the myocardium is expressed by the passive and active properties of the cardiac tissue. As discussed in Chapter 2 different approaches and models were proposed in literature to describe the mechanical behaviour of the myocardium. In this work, a transversely-isotropic constitutive model (Holzapfel and Ogden, 2009) was adopted to describe the passive properties of the cardiac wall while a Hill's based model (Lumens et al., 2009) was used to model the active behaviour of the cardiac tissue. The parameters of this model are adjusted to match the end-diaolic pressure-volume relations of the patient and systolic ventricular pressures and CO measured in the patient respectively.

The last component of the multiscale model is the lumped parameter closed-loop hemodynamic model that generates the hemodynamic boundary condition for the ventricular FE model. The patient-specific parameters of the circulation were obtained through an optimization process described elsewhere (Baretta et al., 2012).

Chapter 4

Pre-operative multiscale models

In the present chapter, the multiscale model representative of the pre-operative state prior the stage 2 surgeries is used to investigate two SV patients. The clinical cases are briefly described, then the set-up of the closed-loop multiscale models is discussed. Finally, full beats simulations of the pre-operative state are performed for each patient and results are discussed.

4.1 Introduction

THIS Chapter is aimed at modelling single-ventricle circulation prior to Stage 2 surgery, to be used for surgical planning. In the first part of the chapter the patients selected in this study are briefly described highlighting the common as the peculiar features they present. As described in the previous chapter, the set-up of the multiscale closed-loop models follow a sequential approach. At first, an identification of the circulatory parameters is performed by means of an optimization strategy that makes use of clinical data as target for the optimization. In this phase, to reduce the computation time a full LP closed-loop model is adopted. Second the 3D model is used stand alone to compute the unloaded reference geometry by means of the unloading algorithm. After unloaded geometry and passive material parameters are determined, isovolumic contraction is performed to tune the active parameters. In the last part of the chapter, the closed-loop multiscale models are assembled to simulate the pre-operative state of the patients and the results are presented and discussed in terms of global hemodynamic quantities and regional myocardial quantities as myofibre stress and strain and wall kinematics of the SV models.

4.2 Clinical cases

Among all the patients recruited for the whole international Project, two patients were selected for the present study: MUSC7 and UM5 whose names are acronyms referred to the clinical centers which provided the patients data. In Table 4.1 the general information of the two patients are reported.

Table 4.1 Patients considered in this study. BSA, body surface area.

Patient	Age (months)	BSA (m^2)	Pathology
MUSC7	3	0.26	HRHS, tric,pulm atresia
UM5	4	0.28	HLHS, Ao, mitral atresia

A determinant for the patient selection was the availability of all the clinical data required to built the multiscale model. Moreover, in order to investigate different clinical scenarios two patients with peculiar features were chosen. As listed in the first and second columns of Table 4.1, both patients undergoing the second stage of the Fontan procedure had similar ages and body surface areas at the time of the surgery. Indeed, this stage of the Fontan surgical treatment

is commonly performed from 2 to 6 months after the birth, and typical BSA for these patients is about 0.3 m^2. The patient MUSC7 had HRHS, while the other had HLHS. Although the only functioning ventricle may perform differently according to its original morphology (RV wall is thinner but gets thicker adapting to the higher after-load when acting as SV and present different fibre orientation), the initial side of the SV was not discriminated in the modelling procedure. Both the patients present severely hypoplastic heart syndrome, unsuitable for a two ventricle circulation who underwent surgical placement of a right modified Blalock-Taussig shunt in the firsts day of life. In the following, HRH (hypoplastic right heart) and HLH (hypoplastic left heart) will be used to refer to MUSC7 and UM5 respectively, as this indication is more clinically relevant and help the reader to keep in mind which pathology the two patients are affected by.

Table 4.2 reports the vascular resistances calculated for each patient. It can be observed that similar values of systemic and pulmonary vascular resistances is present among the two patients. This is consistent with the very similar age and BSA. However, a higher difference can be appreciated comparing the UB and LB vascular resistance as well as the left and right pulmonary resistances. This inter-patient variability may be due to a different development of a body district during growth or to a vasodilation/vasoconstriction in a particular district due to drug administration during data acquisition or other compensatory effects. In particular, different proportions between UB and LB SVR yield to a variety of flow splits between upper and lower body. This will likely affect the way the system reacts to the Stage 2 surgery, where the flow in the UB is directed into the lungs.

Table 4.2 Clinical data of the recruited patients. UB(LB)LSVR = upper (lower) body systemic vascular resistance, R(L)PVR = right (left) pulmonary vascular resistance. Vascular resistances are expressed in mmHg/ml/s.

Patient	SVR	PVR	UBSVR	LBSVR	LPVR	RPVR
HRH	3.07	0.75	4.60	9.20	2.25	1.13
HLH	3.17	0.66	4.33	11.90	1.22	1.45

Tables 4.3, 4.4 and 4.5 summarize the clinical quantities that characterize the considered patients. In particular heart rates, pressures and flows peculiar for each patient are reported.

As regards ventricular volumes, it can be noted that for the two patients different values of volume were available, one measured clinically and one ob-

Table 4.3 Clinical data of the recruited patients. CO, cardiac output; EDV_{clin}, clinical end-diastolic volume; EDV_{MRI}, reconstructed end-diastolic volume; EDV_{FE}, finite element end-diastolic volume. Units are bpm for HR, ml for the EDV and ml/s for CO.

Patient	HR	CO	EDV_{clin}	EDV_{MRI}	EDV_{FE}
HRH	118	27.4	29.0	28.6	28.0
HLH	90	27.0	35.5	31.2	29.6

tained after the manual 3D reconstruction described in Chapter 3. As shown in Table 4.3 the clinical ED volumes is similar to the one obtained from the reconstruction for the patient HRH while for HLH the clinical volume seems to overestimate the reconstructed volume of the patient. It is worth noting that the clinical measured volume is obtained based on cine-MR images: a sequence of few 2D slices is taken on the long axis of the ventricle and the cavity area is drawn manually by the clinician, then the software calculates the EDV assuming the typical ellipsoidal shape model of the healthy LV. It should be noted that for the patient HRH the functional ventricle is the LV while for the patient HLH the SV is the RV. Hence, for HLH the clinical EDV may have errors since the RV shape may not be well approximate by an ellipsoid, thus overestimating the SV volume. On the contrary, the manual reconstructions were performed on about 50 slices and were reviewed by clinicians, the EDV obtained from the reconstructions were assumed as the correct values. Figure 4.1 shows the results of the manual segmentation obtained for the two patients investigated. It can be noted that they showed similar ventricular shapes, except for the valvular plane that is clearly different. This is due to the fact that, since the two patients had different pathology, the functional ventricle was for one patient the LV (HRH) and for the other patient the RV (HLH). It should be noted that for HRH it is possible to identify one valvular plane, while for HLH the two valves lies over two inclined planes. This seems to be a peculiar features of SV patients, indeed in a work parallel to this project the reconstruction of about 40 SV hearts (both HRHS and HLHS) confirmed the difference observed in the valvular plane of the two patients. However, for modelling purpose the valvular plane is disregarded in the FE mesh. This approximation is motivated by the fact that the valvular plane is non-contracting and thus does not contribute to the ventricular pumping function. Moreover, information on the material properties are lacking and similar literature studies on ventricular mechanics commonly avoided this portion in the FE models. It is worth noting that disregarding the valvular plane for the patient HLH implies that the cavity volume in the FE model is slightly

smaller than the reconstructed one.

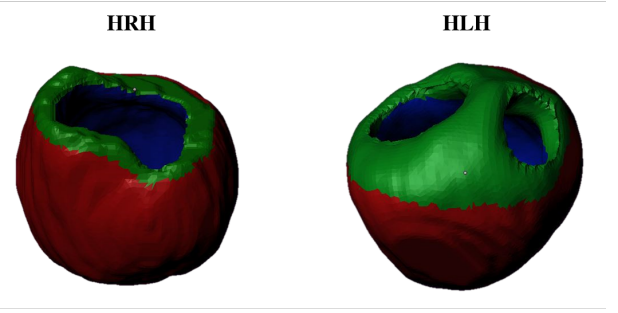

Figure 4.1 Results of the manual segmentations for HRH (left) and HLH (right). In red epicardium, in blue endocardium and in green the valvular plane.

Table 4.4 Clinical data of the recruited patients. *=(min/max/avg); units are bpm for HR and mmHg for pressures. P_{ao}, aortic pressure; mP_{SA}, mean atrial pressure; mP_{PA}, mean pulmonary pressure; maxP_{SV}, maximum single ventricle pressure; EDP_{SV}, single ventricle pressure at end diastole.

Patient	HR	P^*_{ao}	mP_{SA}	mP_{PA}	maxP_{SV}	EDP_{SV}
HRH	118	30/80/53	7	16	82	6.5
HLH	90	30/87/53	5	13	90	6.3

Table 4.5 Clinical data of the recruited patients. Units are bpm for HR and ml/s for flows. mQ_{RPA}, mean right pulmonary flow; mQ_{LPA}, mean left pulmonary flow; mQ_{UB}, mean upper body flow; mQ_{LB}, mean lower body flow; Q_P/Q_S, pulmonary to systemic flow ratio

Patient	HR	mQ_{RPA}	mQ_{LPA}	mQ_{UB}	mQ_{LB}	Q_P/Q_S
HRH	118	8.0	4.0	10.0	5.0	0.8
HLH	90	5.5	6.5	11.0	4.0	0.8

Even though the two patients presented different pathologies they had similar ED volumes and CO. Concerning the measured pressures Table 4.4, even if the patients showed similar ED pressures, maximum aortic and max SV pressure are higher for HLH, while HRH reported the higher values of mean SA

and PA pressures. As already discussed, different vascular resistances of the different vascular district imply different proportions between upper and lower body flow splits. Table 4.5 also reports the ratio of pulmonary to systemic flow (Q_P/Q_S) that is often used by clinicians as an indicator of hemodynamic stability, i.e. balance between pulmonary and systemic blood flow, and to determine the effects of interventions designed to alter the pulmonary flow supply as in single ventricle palliation. In healthy patients, all blood oxygenated by the lungs is directed back to the heart and then to the system, hence Q_P/Q_S=1. In SV circulation, Q_P/Q_S is restored equal to unity after Stage 3, while in the previous steps it may be lower or higher than one according to the patient's vascular resistances and shunt features.

4.3 Set-up of the multiscale models

As described in Chapter 3, the patient-specific closed-loop multiscale model consists of four main parts: an hemodynamic model, an anatomic model of the SV, a passive constitutive model, and an active contractile model. Before the model can be used to make predictions or to investigate the outcome of alternative surgical outputs, a good estimation of patient-specific parameters is required. In this work, a sequential approach has been applied that imply to use both the circulatory LP model and the 3D FE model stand alone prior to assemble the multiscale model.

4.3.1 Identification of circulatory parameters

The adoption of a closed-loop approach was mandatory in order to simulate the changes in the circulatory layout involved in the surgical treatment of SV patients. Thus, the estimation of the circulatory parameters is fundamental to apply proper hemodynamic boundary condition to the 3D FE model. Since the high number of parameters of the circulatory layout, in this work an automatic identification was adopted to avoid manual tuning that is time-consuming and user dependent (Section 3.7).

The results of the simulation of the pre-operatory conditions of the two investigated patients after the optimization process are summarized in Table 4.6. Results from the fully LP stage 1 models were reported against the pre-operative clinical data of the patients.

An overall good agreement for the patients can be observed comparing the right and left columns with an error lower than 5% in each patient-specific case for almost all the quantities taken in to account. Values of the cardiac

Table 4.6 Comparison between the clinical data and the results obtained from the fully LP models for the pre-operatory state of the investigated patients. CO, cardiac output; EDV, end-diastolic volume; EDP_{SV}, single ventricle pressure at end diastole; mP_{ao}, mean aortic pressure; maxP_{ao}, maximum aortic pressure; minP_{ao}, minimum aortic pressure; mP_{SA}, mean atrial pressure; mP_{PA}, mean pulmonary pressure; maxP_{SV}, maximum single ventricle pressure; mQ_P, mean pulmonary flow; mQ_{UB}, mean upper body flow; mQ_{LB}, mean lower body flow.

	HRH		HLH	
	Clin.	Opt.	Clin.	Opt.
CO (ml/s)	27.1	27.5	27.0	27.3
EDV (ml)	28.0	27.1	29.6	30.7
EDP_{SV} (mmHg)	6.5	6.3	6.3	6.0
mP_{ao} (mmHg)	53.0	51.1	53.0	53.1
maxP_{ao} (mmHg)	80.0	81.9	87.0	84.0
minP_{ao} (mmHg)	30.0	31.2	30.0	29.11
mP_{SA} (mmHg)	7.0	7.9	5.0	5.1
mP_{PA} (mmHg)	17.0	17.1	13.3	13.2
maxP_{SV} (mmHg)	82.0	82.8	90.0	86.2
mQ_P (mmHg)	12.0	12.1	12.0	12.1
mQ_{UB} (mmHg)	10.0	10.2	11.0	11.2
mQ_{LB} (mmHg)	5.1	5.2	4.0	4.0

output close to the clinical ones suggest a satisfactorily reproduction of the ventricular-arterial coupling (i.e. the interaction between ventricular behaviour and system impedance), as well as a good diastolic modelling (i.e. ventricular filling). Comparable values of flows between model and clinical data reflect the goodness of the systemic to pulmonary flow split suggesting a good capability of the shunt model used to calculate the linear and non-linear resistances from clinical flow and pressure drop across the shunt. In addition, measured ED ventricular volumes were well captured by the models, thus producing a ventricular pressure-volume loop well positioned. These results suggest that a good set of circulatory parameters has been found for each of the investigated patients.

4.3.2 Unloaded geometry

Since the *in vivo* MR images are necessarily obtained in a loaded configuration, to compute stresses correctly, the unloaded reference state is required. This

unloaded geometry, when loaded to the measured ED pressure, will deform to the measured end-diastolic geometry. This, in turn, depends on the material parameters of the passive constitutive law. A semiautomatic method is adopted in this phase that allows the estimation of the unloaded geometry together with the myocardial passive material parameters. The iterative algorithm described in Subection 3.4.2 performs the estimation on the basis of the ED ventricular geometry, if the ED pressure and the unloaded volume are known.

In Table 4.7 the parameters used to run the unloading algorithm are reported against the computed SV unloaded volume for the two patients considered in this study. Given a set of material parameters the algorithm is able to find the unloading geometry, that when inflated to the EDP_{SV} matched with the ED model, within five iterations. If the difference between the computed (3D model) and the estimated (Equation 3.15) V_{SV0} is lower than 5% the algorithm is not repeated, otherwise the material properties are tuned as described in Subsection 3.4.2 and the unloaded geometry computed again.

Table 4.7 Quantities used in the unloading algorithm for the investigated patients and computed unloading volumes. Units are ml for the volumes and mmHg for the pressure. EDV, end diastolic volume; EDP_{SV}, single ventricle pressure at end diastole; V_{SV0} (est.), estimated unloaded SV volume, V_{SV0} (comp.) computed unloaded SV volume.

Patient	EDV	EDP_{SV}	V_{SV0} (est.)	V_{SV0} (comp.)
HRH	28.0	6.5	11.9	11.6
HLH	29.6	6.3	12.8	12.7

In the fourth column of Table 4.7 the unloaded volume calculated by mens of Equation 3.15 are reported. It is worth noting that for all the patients was possible to find a V_{SV0} (est.) that differ from the estimated one by less than 3%. The estimated parameters are given in Table 4.8.

Table 4.8 Parameters of the passive constitutive model (Holzapfel and Ogden, 2009) models optimized for the patient-specific models.

Symbol	Unit	HRH	HLH
a	kPa	0.76	0.60
b	-	4.50	4.80
a_f	kPa	0.56	0.45
b_f	-	7.30	7.78

It can be seen that the parameters for the two patients are similar, but softer than the default parameters (Table 4.8) of the passive constitutive model obtained fitting experimental data of canine myocardium. As previously reported by Krishnamurthy et al. (Krishnamurthy et al., 2013) these parameters result in a extremely stiff PV relation in the patient-specific models. One reason of that difference can be related to the hardening of the originally tested canine tissue samples due to the effects of rigour, edema and cutting injury. Thus, the material parameters are properly tuned to find the unloading geometries. Figure 4.2 shows both the unloaded geometry and the fitted diastolic model of the patients considered obtained after convergence of the unloading algorithm was achieved.

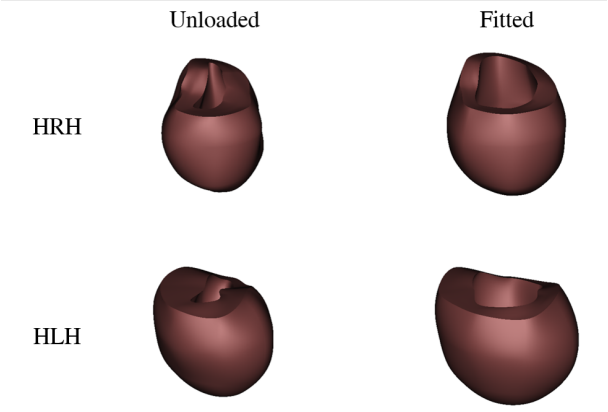

Figure 4.2 On the left, the unloaded meshes obtained after convergence of the unloading algorithm has been achieved. On the right, the meshes fitted to the patient data. The two investigated patients are shown.

4.3.3 Active material properties

Once the passive parameters together with the unloaded geometry were identified for the specific patient, the parameters of the active contraction model to be estimated are the active stress scaling coefficient and the scaling factors of the activation time-function. A suitable patient-specific value for the first parameter was assessed by manual tuning and the use of the active ventricular elastance obtained from the fully LP optimized model. For each patient the stand-alone 3D FE model of the SV was inflated up to three different volumes. Isovolumic contractions were simulated, and the ventricular pressure was

evaluated at maximum contraction. The active stress scaling coefficient was iteratively tuned until the obtained pressures roughly matched those deduced from the fully LP model. Finally, starting from the activation function obtained from the fully LP optimized model, the scaling factors of the contraction time-function were calibrated until the response of the multiscale closed-loop model well reproduced the clinical data.

In Table 4.9 the final active parameters that allowed the multiscale pre-operative models to match the patient behaviours are reported.

Table 4.9 Parameters of the active contraction model (Lumens et al., 2009) optimized for the patient-specific models.

Symbol	Unit	HRH	HLH
τ_D	ms	28	38
τ_R	ms	41	57
τ_{SC}	ms	220	305
s_{act}	kPa	160	300
bcl	ms	508	667

It is worth noting that although the active material parameters of the stand-alone 3D SV model were adjusted on the basis of the elastances obtained from the fully LP model optimization, a finer tuning was still required to match the patient behaviour when the multiscale model was used. This was mainly due to the different description of the myocardium contractility, in particular to the effects of the velocity of contraction. Indeed, while the LP model of SV in the fully LP model accounted for a constant viscosity of the myocardium acting when the SV volume changes, the viscous term included in the active model of the three-dimensional model relied on a more complex description based on sarcomere mechanics. However, the use of the data from the LP model allowed to build the multiscale model starting from working condition closer to the patient pre-operatory behaviour, thus limiting the overall computational cost.

4.4 Pre-operative multiscale results

Once the identification of the patient-specific parameters is carried out the 3D model can be coupled to the LP circulatory model to perform full beats multiscale closed-loop simulation of the pre-operative state. In the following sections the pre-operative results obtained for the patients considered in this study are reported and discussed in terms of global hemodynamic and regional myocardial results.

4.4.1 Global circulatory results

The main role of the SV is to provide an adequate CO to the systemic circulation to ensure the blood perfusion of all the body compartments. Therefore, to analyse the model results, the first aspect to consider is the hemodynamic outcome of the multiscale model in terms of generated pressure and flow. The results of the simulation of the pre-operatory conditions of the investigated patients after the multiscale models are properly set-up are reported in Table 4.10. Results of the multiscale stage 1 models were reported against the pre-operative clinical data. An overall good agreement were obtained for the both the investigated patients in describing the main clinical quantities, with an error lower than 5% in each patient-specific case for almost all the analysed quantities. However, when the error is higher than 5% does not exceed 10%. A proper CO indicates a satisfactory description of ventricular-arterial and venous-atrial couplings. Moreover, the correct repartition of flows to the systemic (Q_{UB} and Q_{LB}) and pulmonary circulations (Q_P) ensures a good modelling of the systemic-to-pulmonary shunt. Measured ED ventricular volumes were well captured by the model, thus a well positioned pressure-volume loop is expectable. A good agreement in EDV values implies a good reproduction of the stroke volume ejected at each cardiac cycle for each patient.

Figure 4.3 shows the pressure tracings (left) and the PVL (right) obtained from the multiscale models of the two patients. Three consecutive cardiac cycles are depicted for the SV and aortic pressures. It is worth observing that a steady solution was obtained after only two cycles (difference lower than 1% between subsequent cycles) for patient HRH and HLH. Indeed, the use of the initial values provided by the fully LP model allowed us to limit the simulation to a few cardiac cycles, with an effective reduction in the total computation time. Another study (Kerckhoffs et al., 2007) in which a 3D biventricular canine ventricular model was coupled to a closed-loop 0D circulatory model reported that 21 full cycles was needed to reach a steady solution even starting from initial values determined by a full lumped parameter circulatory model. However,

Table 4.10 Comparison between the clinical data and the results obtained from the fully multiscale models for the pre-operative state of the investigated patients. CO, cardiac output; EDV, end-diastolic volume; EDP_{SV}, single ventricle pressure at end diastole; mP_{ao}, mean aortic pressure; maxP_{ao}, maximum aortic pressure; minP_{ao}, minimum aortic pressure; mP_{SA}, mean atrial pressure; mP_{PA}, mean pulmonary pressure; maxP_{SV}, maximum single ventricle pressure; mQ_P, mean pulmonary flow; mQ_{UB}, mean upper body flow; mQ_{LB}, mean lower body flow.

	HRH		HLH	
	Clin.	3D	Clin.	3D
CO (ml/s)	27.1	26.7	27.0	27.4
EDV (ml)	28.0	28.7	29.6	29.2
EDP_{SV} (mmHg)	6.5	7.3	6.3	5.9
mP_{ao} (mmHg)	53.0	53.9	53.0	53.2
maxP_{ao} (mmHg)	80.0	81.5	87.0	82.8
minP_{ao} (mmHg)	30.0	31.7	30.0	29.1
mP_{SA} (mmHg)	7.0	7.8	5.0	4.8
mP_{PA} (mmHg)	17.0	16.9	13.3	12.9
maxP_{SV} (mmHg)	82.0	83.3	90.0	85.2
mQ_P (mmHg)	12.0	12.1	12.0	12.2
mQ_{UB} (mmHg)	10.0	10.2	11.0	11.1
mQ_{LB} (mmHg)	5.1	5.2	4.0	4.1

they made use of linear varying elastance models in the LP description while in this work, non linear elastances have been used (Section 3.6) and circulatory parameters are optimized to match clinical data. In the middle panel of Figure 4.3 clinical measured pressure tracings of three cardiac cycles are depicted. It can be seen that the mutiscale models are able to describe the main features of the pressure tracings. The PVL contains useful information on the ventricular functionality, from this data clinicians are used to extract contractility information, typically the ESPVR (i.e. the line tangent to the upper-left corner of the PVL), estimation of unstressed volume and information on the distensibility (i.e. the EDPVR). Also other indexes (EF, stroke work, dP/dt, dV/dt, etc.) can be extracted which are believed to give helpful information on the patient's state. Since the goodness of the global hemodynamic results (proper CO and EDV) the PVL obtained for the patients are well positioned in the PV plane. In the next chapter, the PVL will be used to highlight the changes occurring after simulation of the virtual surgery.

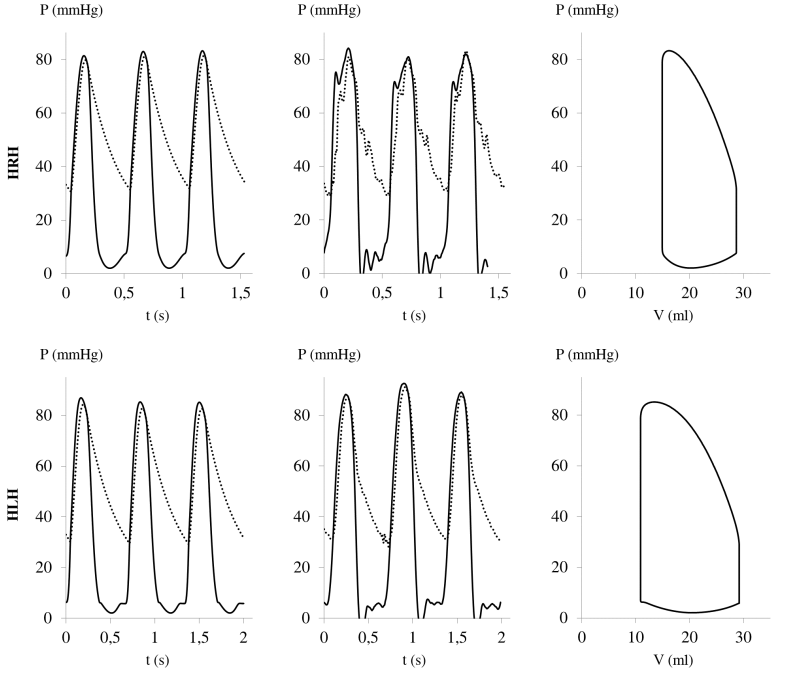

Figure 4.3 Hemodynamic results of the multiscale model for the pre-operatory state of the investigated patients. Pressure tracings of the SV (P_{SV}, solid line) and the aorta (P_{ao}, dotted line) of three consecutive cardiac cycle are shown on the left (model) and in the middle (clinical). On the right, the PVL of one cardiac cycle (model) is shown.

4.4.2 Regional myocardial results

The analysis of wall kinematics and mechanics is fundamental to understand the mechanical function of the ventricle. In this section, the regional myocardial kinematical and mechanical results obtained from the multiscale models of the investigated patients are presented. In particular the former are reported in terms of longitudinal displacement time tracings while the latter are presented as stress and strain time tracings. Regarding stress and strain also mean values at given time of interest (i.e. end diastole, end systole and systolic peak) are presented. All the quantities were evaluated at four different locations through the myocardial wall (Figure 4.4): the ventricular apex, the ventricular base and two ventricular middle sections with respect to the ventricular long axis (Mid1

closer to the apex and Mid2 closer to the base).

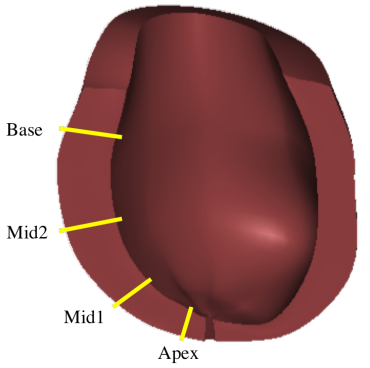

Figure 4.4 Locations of the myocardial wall (Base, Mid2, Mid1 and Apex) where quantities of interest are evaluated.

The longitudinal displacements for the four locations defined are shown in Figure 4.5. The values of the displacements are reported over a normalized time computed with respect to the end of the diastole. For all the patients similar patterns of longitudinal displacement were found. It can be seen that in all the considered cases, higher displacement values are found passing from the base to the apex. Among the investigated patients, HLH showed higher displacement at the systolic peak.

The normalized time tracings of the stress in the fibre direction (averaged over the Guass points) measured at the different locations are shown in Figure 4.6 and Figure 4.7. As expected, for the two patients, at each level of the myocardium an increase in the fibre stresses was observed during the systole with a maximum stress value at the systolic peak while the stresses decrease during the diastole. The corresponding time tracings of the Green-Lagrangian strain tensors in the fibre direction (averaged over the Guass points) are reported in Figure 4.8 and Figure 4.9.

In addition, the mean fibre stress and strain computed as the average value per element weighted by the element volume are depicted in Figure 4.10 at end diastole, end systole and systolic peak. As expected, higher stress are observed at the peak of the systole when the maximum pressure is generated by the ventricle. Comparing the two patients, a similar pattern of time tracings was found. Concerning global stresses in the fibre direction HRH showed higher values at end diastole while during systole HLH showed the higher values. Re-

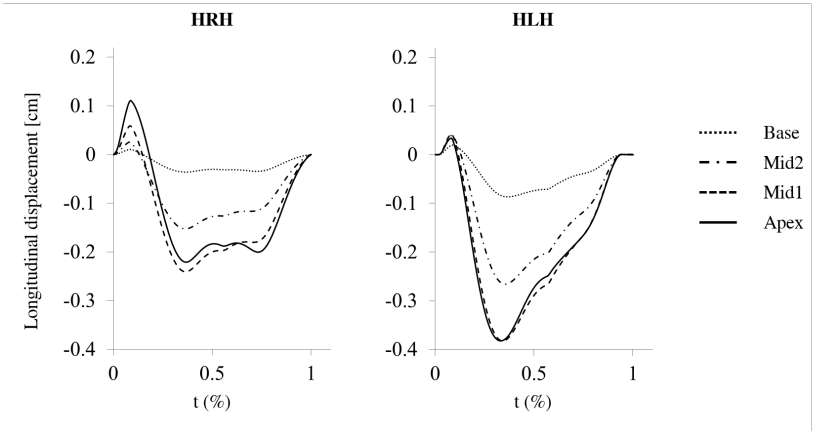

Figure 4.5 Longitudinal displacements for HRH and HLH evaluated at the Apex, the Base and two middle sections (defined as Mid1 and Mid2) with respect to the ventricular long axis. %Time is the normalized cardiac cycle time starting from end diastole.

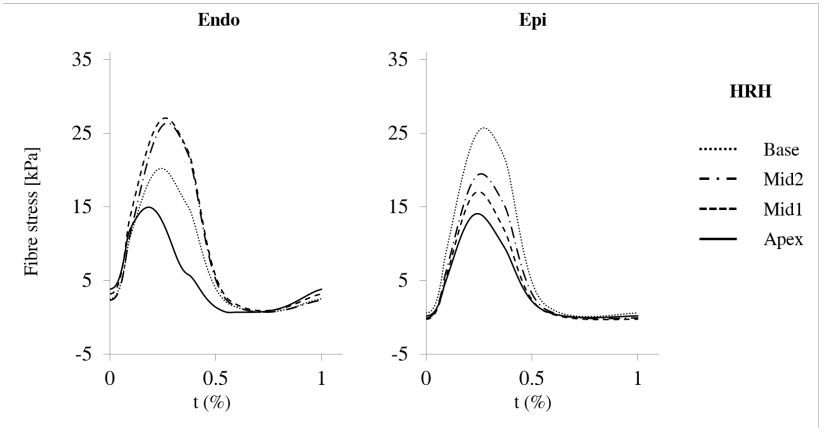

Figure 4.6 Fibre stress for HRH evaluated at the Apex, the Base and two middle sections (Mid1 and Mid2) with respect to the ventricular long axis. %Time is the normalized cardiac cycle time starting from end diastole.

garding the strain in the fibre direction, HRH had the higher fibre strain at end diastole, indicating that this patient resulted in a SV that potentially works in conditions close to the sarcomere decompensation. At end systole both patient

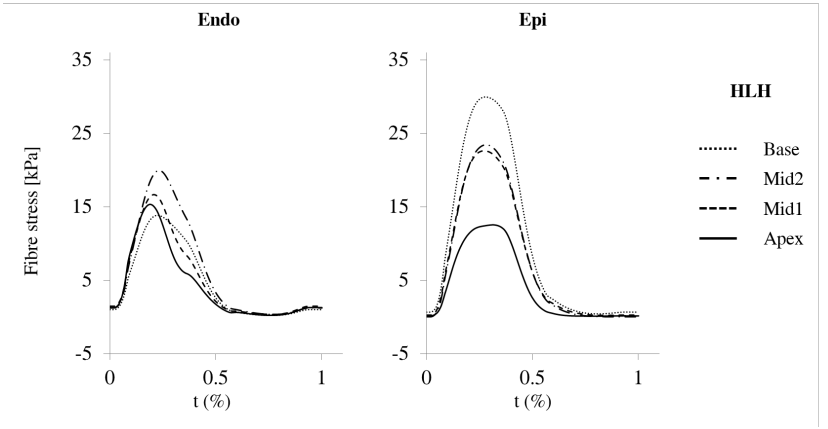

Figure 4.7 Fibre stress for HLH evaluated at the Apex, the Base and two middle sections (Mid1 and Mid2) with respect to the ventricular long axis. %Time is the normalized cardiac cycle time starting from end diastole.

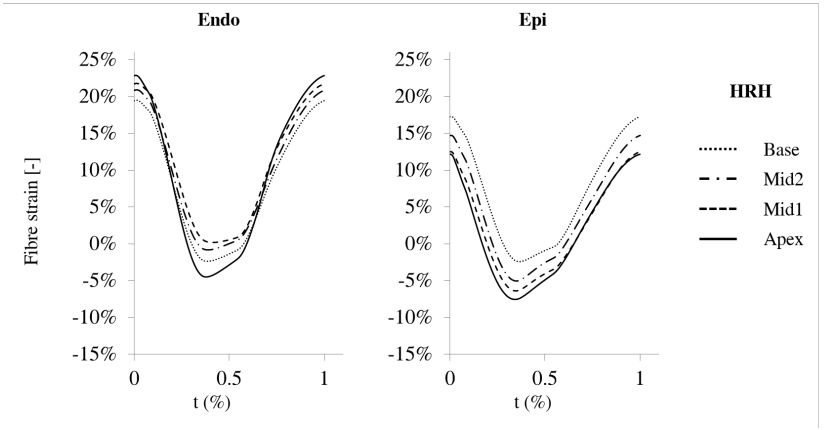

Figure 4.8 Fibre strain for HRH evaluated at the Apex, the Base and two middle sections (Mid1 and Mid2) with respect to the ventricular long axis. %Time is the normalized cardiac cycle time starting from end diastole.

had negative fibre strain indicating that to guarantee the correct stroke volume the sarcomere works at SL lower than that of the resting condition.

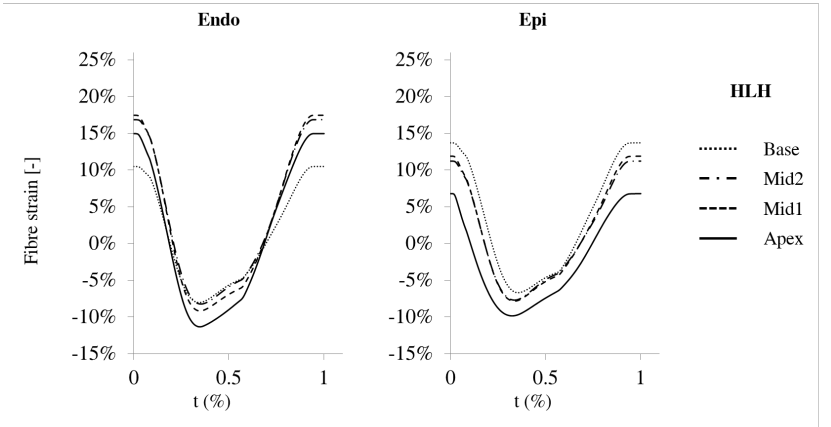

Figure 4.9 Fibre strain for HLH evaluated at the Apex, the Base and two middle sections (Mid1 and Mid2) with respect to the ventricular long axis. %Time is the normalized cardiac cycle time starting from end diastole.

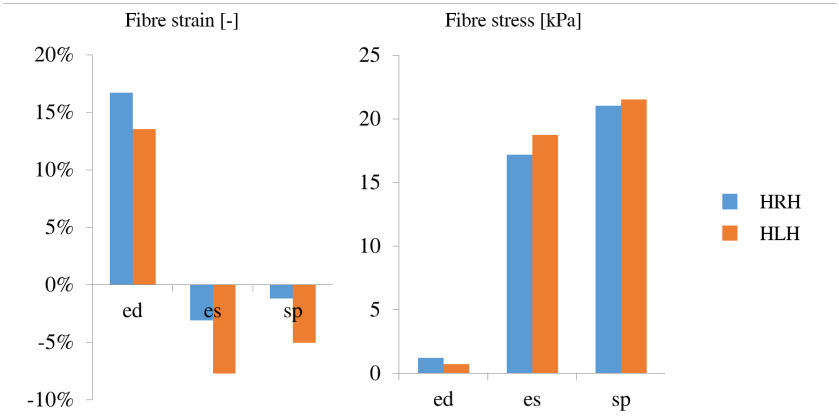

Figure 4.10 Mean fibre strain (left) and stress (right) computed as averaged element value at end diastole (ed), end systole (es) and systolic peak (sp).

In Figure 4.11 the stress and strain distributions in the myocardial wall of the pre-operative conditions for both considered patients are depicted. Stress in the fibre direction are reported at the systolic peak and at end diastole, while the fibre strain is reported at end diastole. Patterns typical for each patient can

be seen, while the maximum values are similar for the investigated patients. Concerning the systolic peak, HLH presented the higher fibre stress (46 kPa) while in the ED state HRH showed the higher values (5 kPa). The magnitude of both average and maximum fibre stress calculated in this work are in agreement with the values calculated in other FE works (Kortsmit et al., 2013; Miller et al., 2013; Palit et al., 2015; Wang et al., 2013; Wenk et al., 2011), thus increasing the confidence in the obtained results. The average ED fibre stress in case of healthy LV was found to be approximately 1-2 kPa while for the ES fibre stress, values in the range 12-16 kPa are reported. In this study, slightly higher values are found for both the patients. This finding are expectable since the SV are known to be subjected to heavier working conditions. An increase in the fibre stress was found also in literature when simulating a pathological state.

Regarding the fibre strain, HRH showed the higher values of strain reaching 25% of strain. It is worth noting that each patient showed significant portions of the myocardial wall were subjected to fibre strains ranging from 20% to 25%. These values are known to be rather critical because they may be close to sarcomere decompensation. Indeed, 20 to 25% of fibre strain correspond to a SL in the range of 2.2-2.4 μm, thus near to the limit of 2.3 μm that indicates sarcomere decompensation. This is expectable for this patients in the stage 1 condition since the SV are subjected to a significant volume overload that could force the ventricle to work in conditions near to the critical. Kortsmit and colleagues (Kortsmit et al., 2013), for a healthy LV reported maximum strain in the fibre direction of 18% at end diastole and 2% at end systole. A maximum fibre strain of 15% was reported by Palit et al. (Palit et al., 2015) at end diastole for a biventricular healthy model. These finding confirm that SV hearts are subjected to working condition unusual for the normal biventricular circulation.

Numerical simulation have been preformed on distributed CPUs using a Quad-Core Intel i7 processor (3,07GHz), 24 GB RAM. For the full beats simulations, a time step of 1 ms was adopted to obtain faster convergence of each time step. A single step of the analysis took from 45 to 50 seconds, depending on the different instant of the cardiac cycle. One full cardiac cycle could take from about 6,2 hours for the HRH patient to 8,2 hours in the case of the HLH patient. The difference is mainly due to the different cardiac cycle length of the two patients (508 ms for HRH and 667 ms for HLH). It is worth noting that, in a single step the heavier computational cost is represented by the calculation of the stiffness matrix of the 3D model (about 90% of the total calculation time), while just few seconds are necessary to solve the lumped parameter circulatory model.

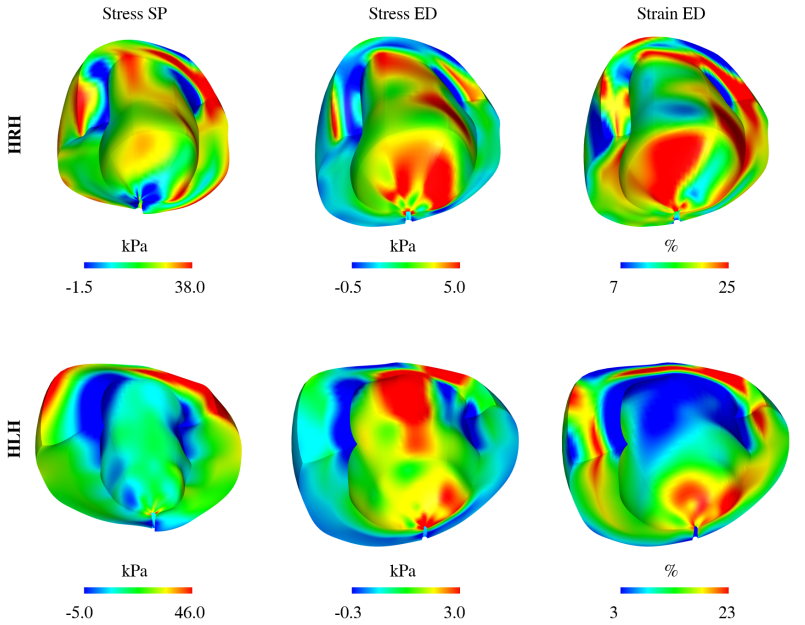

Figure 4.11 Results of the multiscale model of the the investigated patients in the pre-operative state. Distributions of fibre stress (kPa) and strain (%) at the systolic peak (left panel) and at end diastole (middle and right panel).

4.5 Conclusions

In this chapter, multiscale models of the two patients affected by HHS were built to investigate the pre-operative state and comparing the obtain results to the clinical one. In the first part of the Chapter, the clinical cases taken in consideration in this work are presented reporting the peculiar features of the patients and the clinical data used to set-up the models.

A fundamental issue in the development of the multiscale model is the estimation of both the patient-specific SV mechanical properties and the circulatory parameters. Thus, in the second part of the chapter the sequential approach adopted in this study was reported discussing each patient-specifc case. At first, the circulatory layout is considered alone, in a fully lumped parameter description, to estimate the patient-specific circulatory parameters. Then, the 3D FE the SV material parameters and the unloaded reference configuration were iden-

tified using the stand-alone ventricular FE model. The unloaded reference state and the myocardial passive properties were identified by means of the unloading algorithm described in Section 3.4. Then, the 3D finite-element model is contracted isovolumically to perform a first tuning of the active material parameters.

In the final part the multiscale models are assembled and the pre-operative state of each patient simulated. The pre-operative state of the patients were successfully simulated in the two cases (HRH and HLH) with errors in replicating the main global hemodynamic quantities lower then 5%. The regional myocardial results reported were in agreement with other FE works and showed that SV hearts are subjected to heavier working conditions in respect to normal heart

Chapter 5

Post-operative multiscale models

In the present chapter, the multiscale model is used to investigate the changes in the SV physiology after virtual surgery is performed for the two SV patients considered in this study. The modelling procedure is described, then the results of the closed-loop multiscale models are discussed. Finally, additional scenarios as the simulation of the active state and the change in the fibre orientation are simulated and discussed.

5.1 Introduction

THE final goal of this work is to develop a multiscale strategy that allows the simulation of SV circulation and the to predict the behaviour of the SV when subjected to the abrupt changes that happens across the surgical procedure. In this chapter, the surgical procedure from stage 1 to stage 2 is simulated, thus allowing a prediction of the outcomes of the surgery. Post-operative multiscale models are created by manipulating the connection in the lumped parameter network. In the first part of Chapter, patient models were tested at rest conditions (at the time of the clinical measurements) and difference between the pre- and post-operative states are described and discussed in terms of both global hemodynamic quantities and regional myocardial quantities. Then, additional scenarios were simulated with the goal of testing the multiscale models. In particular, active condition and influence of fibre orientation were considered.

5.2 Modelling the stage 2 surgical procedure

As reported in Chapter 1 patients affected by HHS are treated following a three-stage surgical procedure that implies changes in the circulatory layout with the goal of restoring a series of the systemic and pulmonary circulations. In this work, attention was placed on the investigation of the stage 1 physiology and the acute changes happening across the surgery. The treatment involves the ligation of the systemic to pulmonary shunt and the redirection of the upper portion of the systemic venous return to the lungs bypassing the SV, thus helping to relieve ventricular volume overload and resulting in the upper body (UB) systemic circulation being in series with the pulmonary circulation. Since no changes affected the SV anatomy, from the modelling point of view the surgery implies a change in the circulatory model layout. Figure 5.1 shows the difference between stage 1 and stage 2 circulatory layouts: the shunt is removed, the UB circulation is disconnected from the atrium and connected to the lungs. In the absence of specific information, the parameters of the circulatory model is assumed to be unchanged from the pre-operative situation, thus simulating an acute change. Similarly, the myocardial properties of the 3D ventricular model are assumed unchanged. Final values of the last stabilized cardiac cycle simulated using the pre-operative model are used as initial conditions for the post-operative simulations.

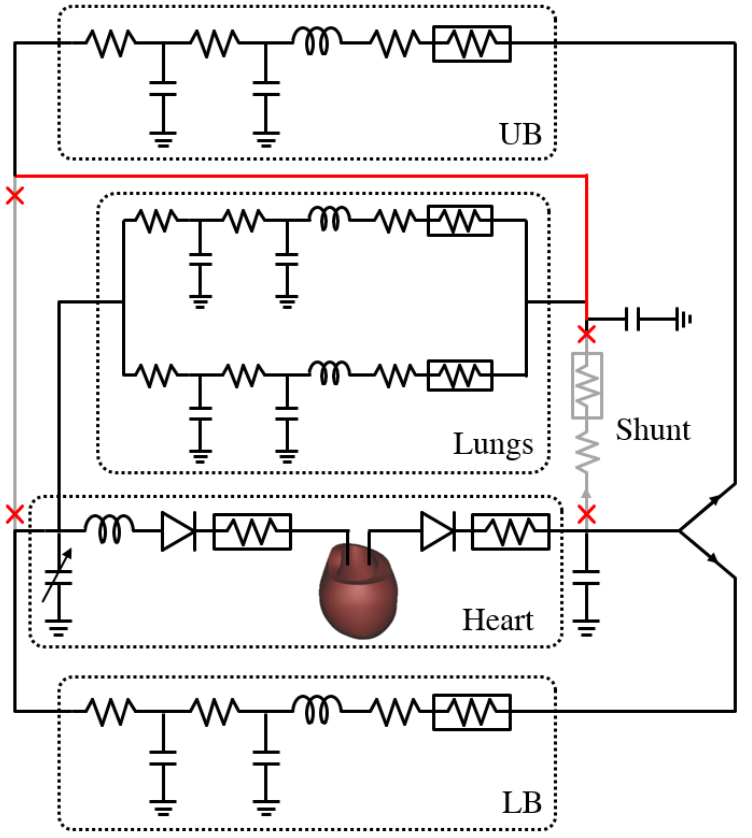

Figure 5.1 Patient-specific biomechanical model for stage 2. The circulatory layout comprised the single heart, the systemic upper body (UB), lower body (LB) and lungs circulations. After the stage 2 surgery, the shunt is removed and the UB circulation connected in series to the pulmonary circulation. Changes in the circulatory layout after stage 2 are shown in red while the elements of the stage 1 circulation which are removed in the surgery are coloured in grey. The single ventricle is modelled by the 3D FE model.

5.3 Post-operative multiscale simulations

Once the pre-operatory multiscale is properly simulated, the model can be used to perform virtual surgery and to evaluate the acute changes associated to the surgical treatment. In the following sections the post-operative results

obtained for the patients considered in this study are reported and compared with the pre-oprative state.

5.3.1 Global circulatory results

The results of the multiscale simulation of the post-operatory conditions of the two patients investigated in this study are reported in Table 5.1. Results from the last cycle, after the solution had stabilized, were used in the analysis.

Table 5.1 Comparison between the pre- and post-operative results obtained from the multiscale models for the investigated patients. CO, cardiac output; EDV, end-diastolic volume; EDP_{SV}, single ventricle pressure at end diastole; mP_{ao}, mean aortic pressure; maxP_{ao}, maximum aortic pressure; minP_{ao}, minimum aortic pressure; mP_{SA}, mean atrial pressure; mP_{PA}, mean pulmonary pressure; maxP_{SV}, maximum single ventricle pressure; mQ_P, mean pulmonary flow; mQ_{UB}, mean upper body flow; mQ_{LB}, mean lower body flow.

	HRH		HLH	
	Pre	Post	Pre	Post
CO (ml/s)	26.7	20.3	27.4	19.0
EDV (ml)	28.7	26.3	29.2	24.1
EDP_{SV} (mmHg)	7.3	4.6	5.9	2.2
mP_{ao} (mmHg)	53.9	74.0	53.2	69.1
maxP_{ao} (mmHg)	81.5	95.8	82.8	90.4
minP_{ao} (mmHg)	31.7	55.5	29.1	50.6
mP_{SA} (mmHg)	7.8	4.6	4.8	1.7
mP_{PA} (mmHg)	16.9	14.4	12.9	10.6
maxP_{SV} (mmHg)	83.3	96.7	85.2	91.3
mQ_P (mmHg)	12.1	12.9	12.2	13.4
mQ_{UB} (mmHg)	10.2	12.9	11.1	13.4
mQ_{LB} (mmHg)	5.2	7.4	4.1	5.6

The results obtained from all the post-operative multiscale models show comparable variations in the global hemodynamic parameters with respect to the pre-operative stage 1 model. Unfortunately, post-operative data are not usually collected in the clinical practice owing to the invasiveness of such exams and to the absence of necessity for clinical aims. Thus, for the investigated patients the obtained results are compared only with the pre-operative results.

The changes in the circulatory layout associated with the stage 2 surgery, led to an increase in the after-load and to a decrease of the preload of the SV. Figure 5.2 (left) shows the pressure tracings (P_{SV} , P_{ao}) of six consecutive cardiac cycles (necessary to reach the steady state, i.e. difference in in the hemodynamic quantities lower than 1% between two subsequent cardiac cycles) after the circulatory model was changed to simulate the surgery.

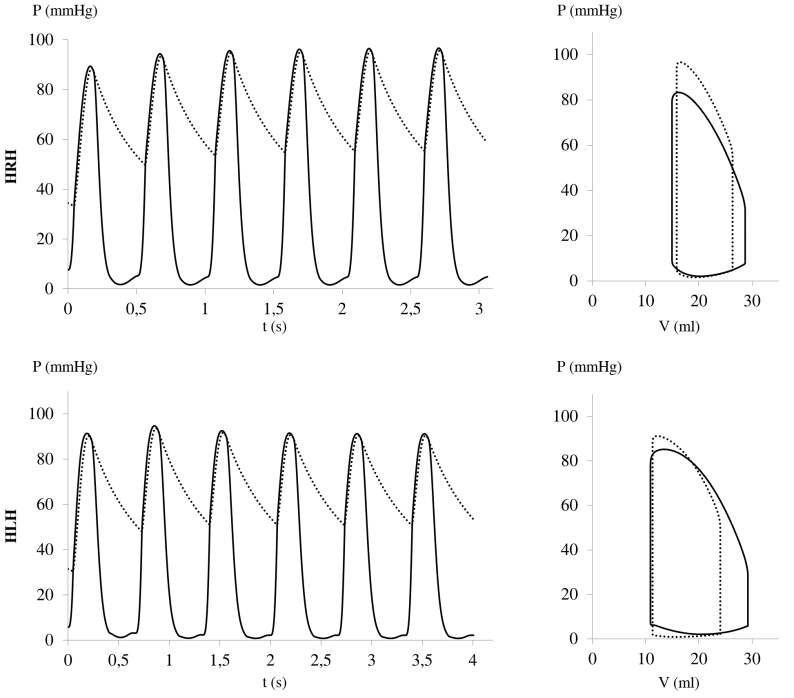

Figure 5.2 Hemodynamic results of the multiscale model after simulation of the surgical procedure state for the investigated patients. On the left, pressure tracings (P_{SV}, solid line and P_{ao} dotted line) of six consecutive cardiac cycles. On the righ, pressure-volume loops of the pre- (solid line) and the post-operative (dotted line) state are shown.

The analysis of the pre-operative and post-operative PVLs reported in Figure 5.2 (right) shows that as a consequence of the surgery, a significant decrease of the stroke volume with a slight increase in the end-systolic volume together with a larger decrease of the ED volume. A decrease in the CO together with

an increase of the ventricular peak pressure can be noted. Mean aortic pressure increases and similar increments also occurred in both systolic and diastolic values. Conversely, the atrial pressure decreased. These significant changes of variables mean values in the post-operative state from the pre-operative were expected with ventricle volume unloading and the increasing in the afterload. Indeed, in stage 1 circulation, the total resistance was composed of three resistances in parallel: UB and LB systemic vascular resistances and the series of shunt and pulmonary vascular resistances. After stage 2 surgery, the shunt resistance was removed, whereas the UB is connected in series with the PVR. As a consequence, the total afterload of the heart increased post-operatively (Figure 5.3). The repartition of flows in post-operative conditions depends on the contribution of the shunt resistance and the PVR resistance to the total parallel of resistances: the higher amount of flow passes through the shunt in Stage 1 (high Q_P/Q_S), the more sensitive to the layout change will be the post-operative flow distribution. In general, high Q_P/Q_S corresponds to a more evident decrease in the CO post-operatively, and vice-versa.

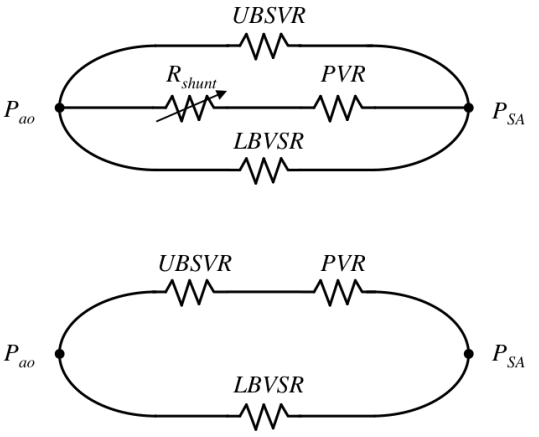

Figure 5.3 Schematic representations of the total resistances seen by the SV heart before (up) and after (down) the surgery.

Comparing the post-operative configurations of the patients, different behaviors are exhibited, higlighting a patient-specific response to the surgery, which is likely related to the combination of vasculature impedance and confirm the need for patient-specific investigation of in this peculiar patients. Analyzing the results for each patients, interesting considerations can be deduced. Com-

paring HRH to HLH, pre-operatively they presented similar vascular resistances (0.75, 4.60, 9.20 vs. 0.66, 4.33, 11.90 for PVR, UBSVR, LBSVR) and systemic to pulmonary flow split (Q_P/Q_S 0.80, and 0.79 respectively) resulting in a post-operative decrease of the CO of 24% and 30% respectively. Concerning the unloading of the SV, HLH showed the highest reduction in the EDV in the post-operative state (17%) while for HRH is lower (8% and 13% respectively). The ventricular unloading represents a beneficial change, because the ventricle operates at a lower ED volume, thus reducing the risk of critical conditions that could lead to sarcomere decompensation. This suggest that HLH had more beneficial effects in respect to the other patient and this can be related to the higher decrease in the mean atrial pressure for the patient.

In summary, comparing post-operative and pre-operative simulations: i) stroke volume (i.e. the CO, assuming no change in HR) significantly decreases (about 20-40% depending onthe considered patient; ii) the EDV decreases confirming the beneficial effect of the surgery; iii) aortic pressure increases in the mean value; iv) each patient presents specific response to the surgical procedure confirming the need for patient-specific modelling. It is worth noting that the predicted changes in flows and pressures are in a good agreement with a previous work (Corsini et al., 2014), in which the authors reported decrease of the CO of 21% together with a slight increase in the systolic pressure. Moreover, they reported an increase in the mean aortic pressure as in both systolic and diastolic values, thus increasing the confidence in the results obtained from the multiscale models.

5.3.2 Regional myocardial results

In this section, the regional myocardial kinematical and mechanical results of the post-operative model are presented and compared with the results of the corresponding pre-operative model. The comparison of the longitudinal displacements obtained from the pre-operative model and the post-operative model are summarized in Figure 5.4 and 5.5. A slight increase in the longitudinal displacement in the post-operative condition as respect of the pre-operative one can be observed for each patient during the diastolic phase while a decrease in the longitudinal motion was found in diastole. This is associated with the decrease of the stroke volume after the stage 2 surgeries is performed, with HLH that showed an higher decrease of the longitudinal displacement coherent with the higher decrease in the CO post-operatively.

The time profile of the Green-Lagrange strain tensor in the fibre direction of the post-operative model is depicted in Figure 5.6 and 5.7 for all the considered

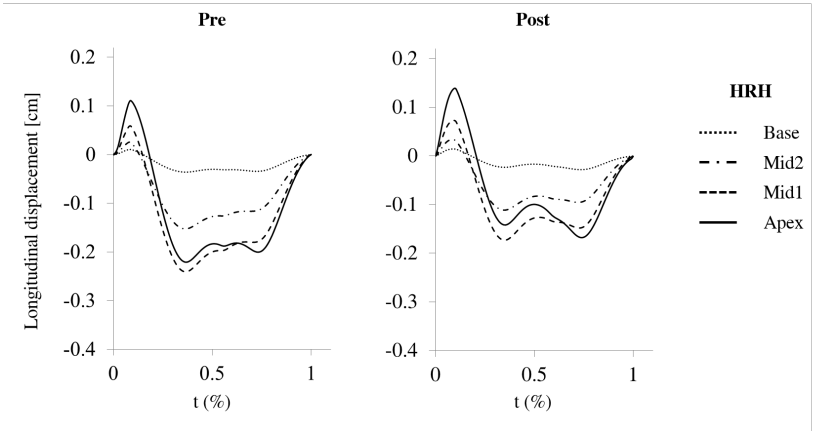

Figure 5.4 Longitudinal displacements obtained from the pre-operative and post-operative models for HRH evaluated at the Apex, the Base and two middle sections (Mid1 and Mid2) with respect to the ventricular long axis. %Time is the normalized cardiac cycle duration starting from end diastole.

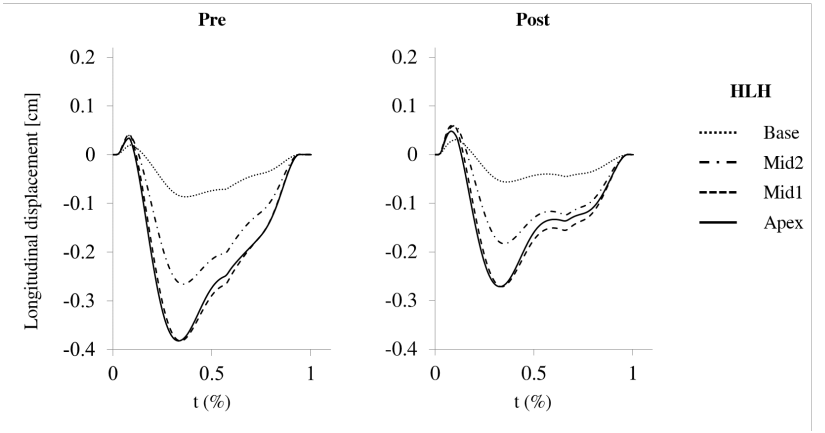

Figure 5.5 Longitudinal displacements obtained from the pre-operative and post-operative models for HLH evaluated at the Apex, the Base and two middle sections (Mid1 and Mid2) with respect to the ventricular long axis. %Time is the normalized cardiac cycle duration starting from end diastole.

locations along the myocardial wall. The comparison of the fibre strain highlights an overall reduction of the diastolic strain in the post-operative condition with respect to the pre-operative one, which is consistent with the results from the corresponding patient's PVLs Figure 5.2 (right). Indeed, lower ED volumes were observed for all the considered patient after the surgery simulations.

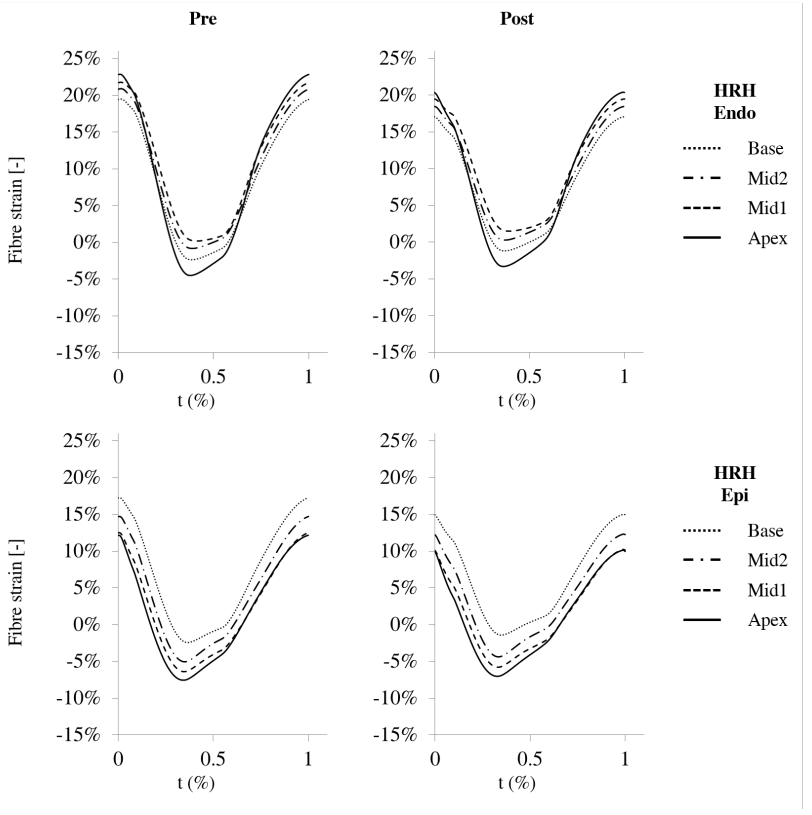

Figure 5.6 Fibre strains obtained from the pre-operative and post-operative models for HRH evaluated at the Apex, the Base and two middle sections (Mid1 and Mid2) with respect to the ventricular long axis. %Time is the normalized cardiac cycle duration starting from end diastole.

The comparison of the fibre strain highlights an overall reduction of the diastolic strain in the post-operative condition with respect to the pre-operative one, which is consistent with the results from the corresponding patient's PVLs

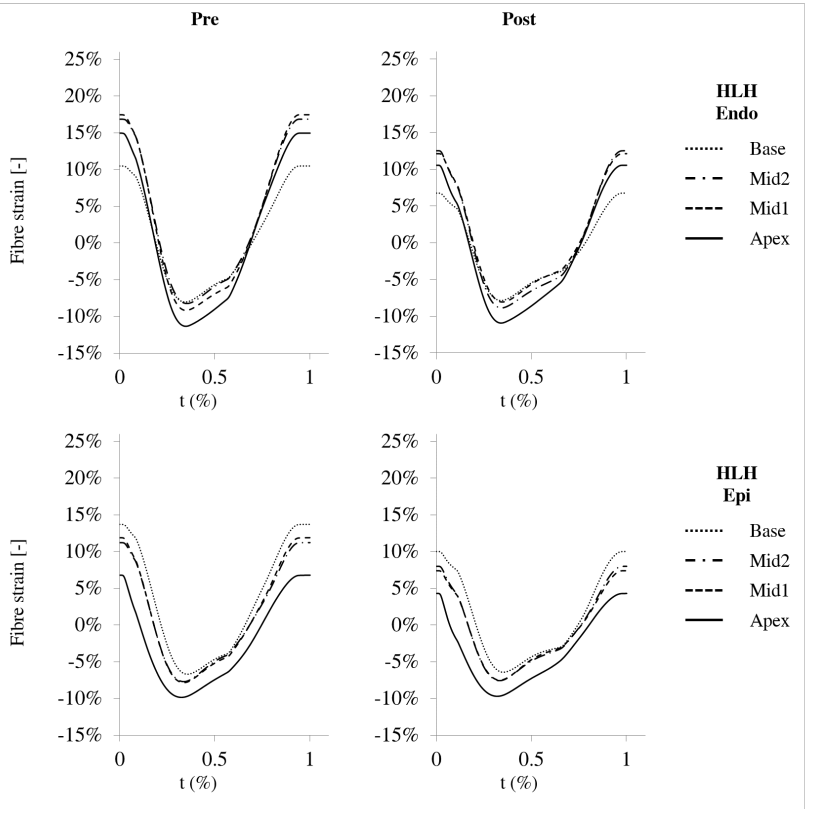

Figure 5.7 Fibre strains obtained from the pre-operative and post-operative models for HLH evaluated at the Apex, the Base and two middle sections (Mid1 and Mid2) with respect to the ventricular long axis. %Time is the normalized cardiac cycle duration starting from end diastole.

Figure 5.2 (right). Indeed, lower ED volumes were observed for all the considered patient after the surgery simulations. Again this results are corroborated by the increase of the systolic pressure highlighted in the post-operative condition.

Conversely, the comparison of the fibre stresses in the post-operative state to the pre-operative one showed an increase of the stress value for all the considered location of the myocardium during systole. Figure 5.8 shows the stress pattern for both the pre-operative and post-operative conditions at the end of the diastole and at the systolic peak. Concerning the ED state, a reduction of

the maximum stress in the myocardium was observed from stage 1 to stage 2 as well as in the overall values for all the patients considered in this study. This reduction of myocardial stress was expected as a consequence of the change of the layout of the circulation, which leads to the unloading of the ventricle. The stress pattern distribution was preserved from the pre-operative to the post-operative state. Indeed, the simulation of the stage 2 surgical procedure represented an acute condition, thus the remodelling process associated with chronic condition was neglected. With respect to the systolic peak, an opposite trend was observed. Indeed, a higher systolic peak pressure was found in stage 2 with respect to stage 1 as shown in the PVL reported in Figure 5.2.

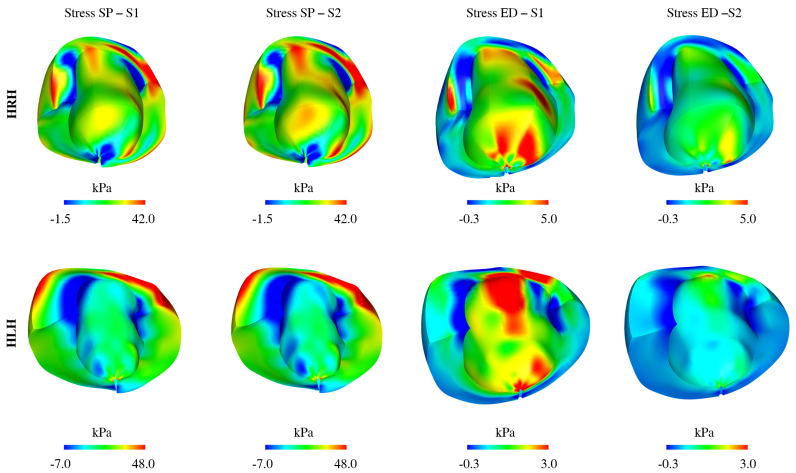

Figure 5.8 Results of the multiscale model of the there investigated patient in the pre-operative state. Distributions of fibre stress (kPa) at the systolic peak (left panel) and at end diastole (middle and right panel).

The maximum ED strains in the fibre direction at the stage 1 and stage 2 are summarized in Table 5.2. An overall reduction of the fibre strains in the stage 2 was found with respect to stage 1 for all the patients. In stage 1, significant portions of the myocardial wall were subjected to fibre strains ranging from 20% to 25%. These values are known to be rather critical because they are very close to sarcomere decompensation. The decrease in the fibre strain observed for all the patient confirm the beneficial effect for the SV after volume unloading.

Table 5.2 Comparison between the pre- and post-operative fibre strain for the investigated patients. The maximum value measured in the patient is reported.

	HRH		HLH	
	Pre	Post	Pre	Post
ED strain	25	22	23	18

In addition, the average fibre stress and strain computed as the average value per element weighted by the element volume are depicted in Figure 5.9 and 5.10 at end diastole, end systole and systolic peak. This results confirm the previous finding, each patient experienced a positive effect due to the stage 2 surgery with a significant decrease in the fibre stress and strain at end diastole related to the unloading of the SV. Conversely, a global increase in the fibre stress at the systolic peak as well as at end systole was observed. This is related to the higher pressure generated by the ventricle during the systolic phase.

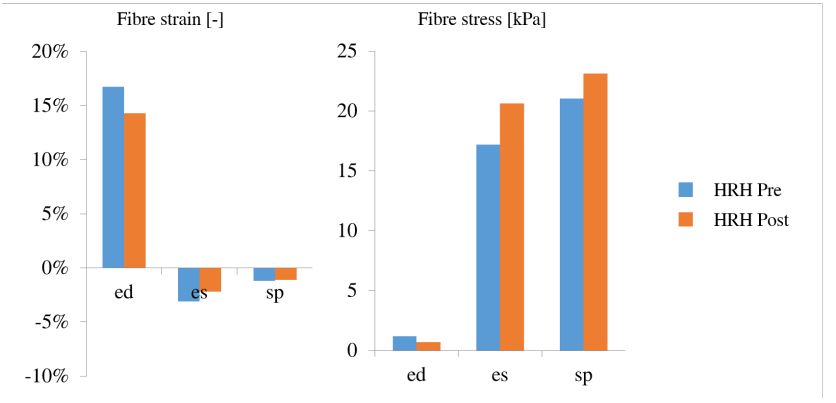

Figure 5.9 Mean fibre strain (left) and stress (right) computed as averaged element value at end diastole (ed), end systole (es) and systolic peak (sp) for the patient HRH. Pre-operative versus post-operative results.

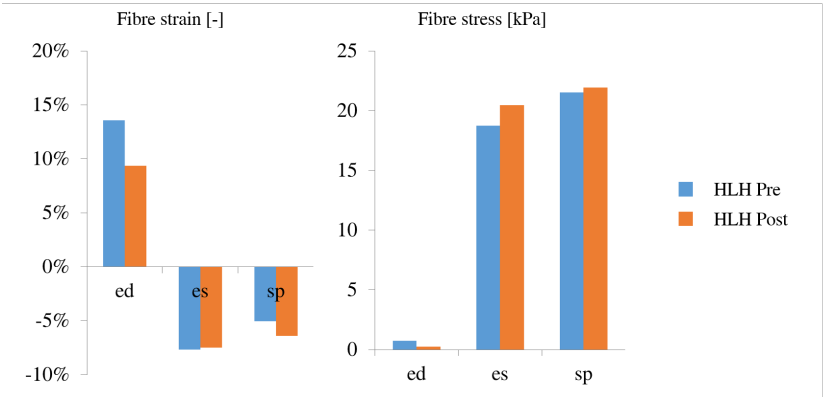

Figure 5.10 Mean fibre strain (left) and stress (right) computed as averaged element value at end diastole (ed), end systole (es) and systolic peak (sp) for the patient HLH. Pre-operative versus post-operative results.

5.4 Simulation of additional scenarios

In the first part of this Chapter for all the patients under study virtual surgery simulations were reported. Even though the results are not validated against clinical data, the obtain results are in agreement with other modelling studies, thus suggesting a good modelling of the surgical procedure. Once the model is properly set-up and reliable results are obtained, it is possible to explore other scenarios to evaluate the performance of the multiscale model in simulating conditions different from the clinical ones. In this Section active conditions and different fibre orientation were performed on the two patients to assess whether different simulating conditions might affect the response of the multiscale model.

5.4.1 Active state

For the patient HRH, an active condition state which approximates the physiology of the patient during voluntary movements of the limbs and increased blood flow was simulated. An active state of an infant was chosen to replicate an exercise state of an older patient capable of exercising. Thus a new set of circulatory parameter values was prescribed. In particular, to simulate the active condition an increase of 30% in heart rate (Berg et al., 1971) and a decrease of 20% and 30% in PVR and total SVR respectively (Kung et al., 2013) were assumed. More precisely, when active state is simulated the vessels are assumed to vasodilate (i.e., they increase their diameter) thus decreasing the resistance and increasing the compliance. Considering the dependence of the parameters on the diameter ($R \approx D^4$ and $C \approx D^3$, (Pennati et al., 2000)), and leaving other factors unchanged (e.g. the wall thickness), the compliances C_{i-act} of lungs and leg blocks during active conditions were obtained according to Equation 5.1:

$$C_{i-act} = C_i \left(\frac{R_{i-act}}{R_i} \right)^{-3/4} \tag{5.1}$$

where C_i and R_i are the compliances and resistances of the i^{th}-block in the model under normal resting condition, and C_{i-act} and R_{i-act} are the compliances and the resistances of the i_{th}-block under active condition. All other model parameters and fluid properties were kept fixed.

Figure 5.11 (left) shows the pressure tracings of the six cardiac cycles necessary to reach a steady solution while on the right the PVL of the last cycle (dotted line) is reported superimposed to the PVL representative of the resting

condition (solid line). It can be seen a significative drop in the pressures and EDV as response to the vasodilation effect and increase of the heart rate. The area inside the pressure-volume loop for the active condition is smaller than that for the resting condition in both patients, indicating that a lower work is performed during each individual cardiac cycle.

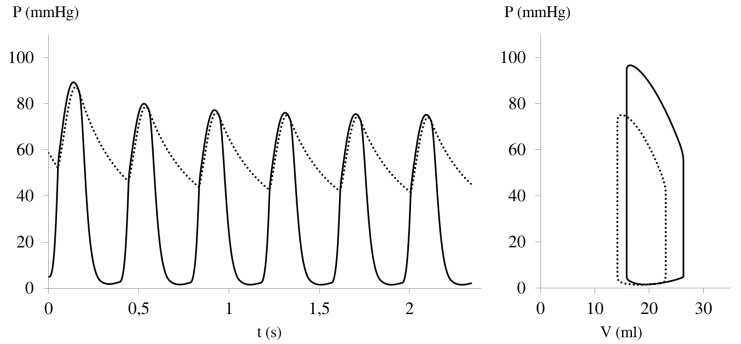

Figure 5.11 Hemodynamic results of the multiscale model after simulation of the active state for the patient HRH. On the left, Pressure tracings of the SV (P_{SV}, solid line) and the aorta (P_{ao}, dotted line) of six consecutive cardiac cycle are shown. On the right, PVL of the active state (dotted line) compared to the PVL of the resting state (solid line).

Results are shown in Table 5.3 in terms of mean values representative of the global performance of the model. As a consequence of the increased heart rate and decrease in vascular resistances, CO increased with respect to rest conditions of about 10%. Even though the HR is increased of 30% the decrease in the stroke volume partially compensates the increasing of the CO. The pulmonary flow as well as the UB flow increased of the same amount as CO while the mean pressure in the aorta decrease of about 30%. It is worth nothing that similar behaviour of the hemodynamic quantities is consistent with another study (Kung et al., 2013) in which the exercise conditions was simulated for two patient-specific cases of SV circulations.

To evaluate the effect of the active state, the tracings of longitudinal displacements normalized with respect to the resting cycle duration and evaluated at different locations (i.e., apex, two middle cross sections (mid1 and mid2) and base) for both the resting and the active state condition were compared (Figure 5.12). An increase of the maximum longitudinal displacements was observed during the systole for all the considered locations while an overall reduction of the longitudinal displacements were found in the diastolic phase. In addition,

Table 5.3 Comparison between the resting and active results for the patient HRH. CO, cardiac output; EDV, end-diastolic volume; EDP_{SV}, single ventricle pressure at end diastole; mP_{ao}, mean aortic pressure; maxP_{ao}, maximum aortic pressure; minP_{ao}, minimum aortic pressure; maxP_{SV}, maximum single ventricle pressure; mQ_P, mean pulmonary flow; mQ_{UB}, mean upper body flow; mQ_{LB}, mean lower body flow.

	HRH	
	Resting	Active
CO (ml/s)	20.3	22.3
EDV (ml)	26.3	21.3
EDP_{SV} (mmHg)	4.6	2.2
mP_{ao} (mmHg)	74.0	56.4
maxP_{ao} (mmHg)	95.8	73.9
minP_{ao} (mmHg)	55.5	41.6
maxP_{SV} (mmHg)	96.7	74.9
mQ_P (mmHg)	12.8	14.2
mQ_{UB} (mmHg)	12.8	14.2
mQ_{LB} (mmHg)	7.5	8.2

the resting and active conditions were compared in terms of average stress and strain (Figure 5.13).

A decrease in both the fibre stress and strain were observed which are consistent with the hemodynamic results. Indeed, in the active state condition a decrease in the systolic peak pressure and of the end diastolic volume was found. Indeed, in the active state the increase in the CO due to the increase of the HR was associated to a decrease in the ED volume. Moreover, due to the vasodilation a decrease in the systolic pressure was observed. Accordingly, an overall reduction in both the mean fibre stress and mean strain was reported for the active state with respect to the resting condition.

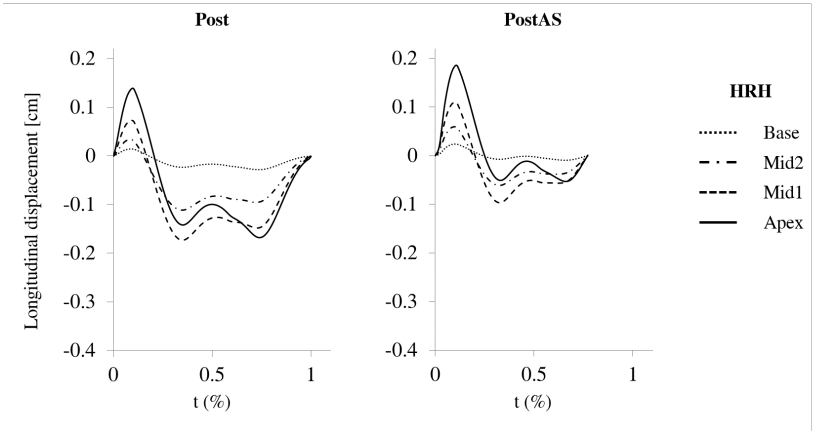

Figure 5.12 Longitudinal displacements obtained from the post-operative model for the resting and active condition for the patient HRH evaluated at the Apex, the Base and two middle sections (Mid1 and Mid2) with respect to the ventricular long axis. %Time is the normalized cardiac cycle duration starting from end diastole.

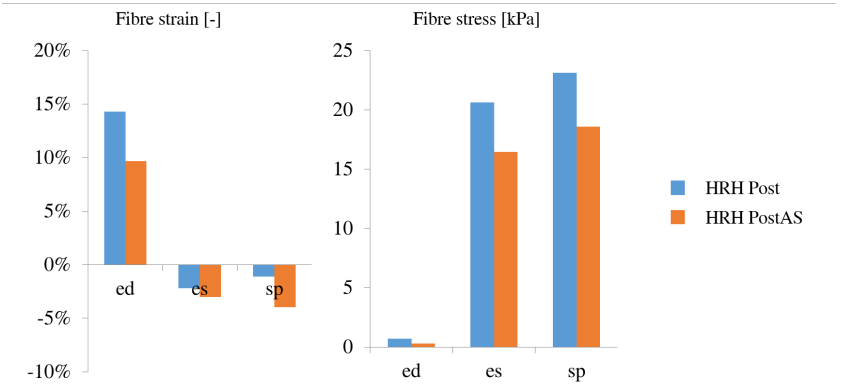

Figure 5.13 Mean fibre strain (left) and stress (right) computed as averaged element value at end diastole (ed), end systole (es) and systolic peak (sp) for the resting and active states.

5.4.2 Influence of the fibre orientation

As discussed in Subsection 3.3.3 no information about the fibre orientation was available for the investigated patients. Thus, typical patterns for adults and physiological state were assumed. In case of HRHS, the assumption can be considered more reliable since the only functional ventricle for this patient was the LV. Thus, the SV is a systemic ventricle which underwent an higher work, but still as a systemic ventricle. Instead, in case of HLHS, the functional ventricle is the RV, thus a ventricle that normally behave at different pressures. The RV wall is thinner but gets thicker adapting to the higher after-load when acting as systemic SV. Under the hypothesis that also the fibre orientation may change adapting to the higher work, in this Section for the patient HLH, we tested both the fibre orientation of the healthy RV and LV.

In the sequential approach adopted in this work, the identification of the circulatory parameters did not account for differences in the material properties of the myocardium and in the fibre orientations, thus the circulatory layout was kept fixed for both configurations (RV and LV). Instead, the unloading algorithm was repeated to account for possible difference due to the different fibre orientation. It is worth noting that given the same set of material parameters found for the RV configuration, the algorithm was able to find an unloaded geometry in the LV configuration that presented an unloaded volume with difference between the computed (3D model) and the estimated (Equation 3.15) V_{SV0} lower than 5%. Thus, the algorithm was not repeated and the unloaded geometry was accepted to build the multiscale model. Once the unloaded geometry were identified, the 3D model was inflated at the ED pressure and then was coupled to the circulatory model using as active parameters those identified for the RV fibre configuration. In Table 5.4, the global hemodynamics results are summarized for both the pre- and post-operative condition. It is worth noting that, using different fibre orientations and same active parameters no significant changes in the global hemodynamic can be seen. Thus, adopting in the 3D model a different configuration of fibre orientation the global pumping functionality of the SV was not significantly affected. Indeed, in both cases the SV were able to replicates the hemodynamics conditions of the patients in the pre-operative state and behaved in a similar way after the simulation of the stage 2 surgery.

The analysis of the longitudinal displacements in case of fibre distributed according to physiological pattern of the LV showed an increase in the systolic phase and a decrease in the diastolic phase for the LV cases with respect to the RV case (Figure 5.14). It is worth noting that even though for both cases the global hemodynamics is similar in the pre- and post-operative conditions

Table 5.4 Comparison between the pre- and post-operative results obtained from the multiscale models for HLH with different fibre orientations. CO, cardiac output; EDV, end-diastolic volume; EDP_{SV}, single ventricle pressure at end diastole; mP_{ao}, mean aortic pressure; maxP_{ao}, maximum aortic pressure; minP_{ao}, minimum aortic pressure; mP_{SA}, mean atrial pressure; mP_{pa}, mean pulmonary pressure; maxP_{SV}, maximum single ventricle pressure; mQ_P, mean pulmonary flow; mQ_{UB}, mean upper body flow; mQ_{LB}, mean lower body flow.

	HLH			
	Pre (RV)	Pre (LV)	Post (RV)	Post (LV)
CO (ml/s)	27.4	26.9	19.0	18.8
EDV (ml)	29.2	29.1	24.1	24.0
EDP_{SV} (mmHg)	5.9	6.0	2.2	2.3
mP_{ao} (mmHg)	53.2	52.3	69.1	68.5
maxP_{ao} (mmHg)	82.8	81.5	90.4	89.6
minP_{ao} (mmHg)	29.1	28.7	50.6	50.2
mP_{SA} (mmHg)	4.8	4.8	1.7	1.7
mP_{pa} (mmHg)	12.9	12.8	10.6	10.6
maxP_{SV} (mmHg)	85.2	83.8	91.3	90.4
mQ_P (mmHg)	12.2	12.0	13.4	13.3
mQ_{UB} (mmHg)	11.1	10.9	13.4	13.3
mQ_{LB} (mmHg)	4.1	4.0	5.6	5.5

peculiar displacement pattern were observed in all the conditions simulated depending on the fibre orientations. In the case of RV fibre orientation the SV showed higher longitudinal displacement, that is expectable since in this case at the endocardium the fibre are longitudinal (-90 vs -60 for the LV). In case of LV configuration the patient showed longitudinal displacement with a pattern similar to that observed for the patient HRH (Figures 4.5 and 5.4) in both pre- and post-operative states confirming that the kinematics of the myocardial wall is affected by the fibre orientation. Unfortunately, information on wall movements were not available for the patients considered in this study, thus was not possible to validate these assumptions. However, these findings may be useful in further study to increase the understanding of such complex pathology.

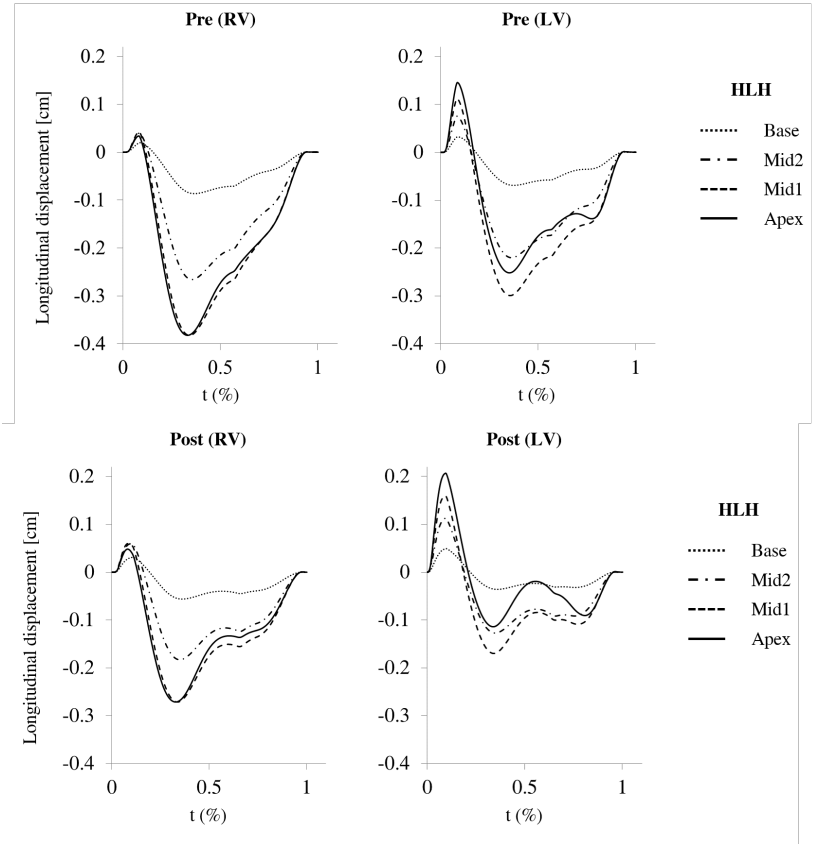

Figure 5.14 Time tracings of the longitudinal displacements obtained from the simulation of pre- and post-operative conditions for the two different fibre orientations (RV vs LV) evaluated at the Apex, the Base and two middle sections (Mid1 and Mid2) with respect to the ventricular long axis. %Time is the normalized cardiac cycle duration starting from end diastole.

The comparison of the time profile of the fibre strain (Figure 5.15) in case of RV fibre distribution and LV distribution showed higher values of the strain values in all the considered locations in case of LV configurations. However, the strain patterns appeared qualitatively more homogenous at the various location through the cardiac cycle.

The evaluation of the mean values of the fibre stress and strain (Figure 5.16

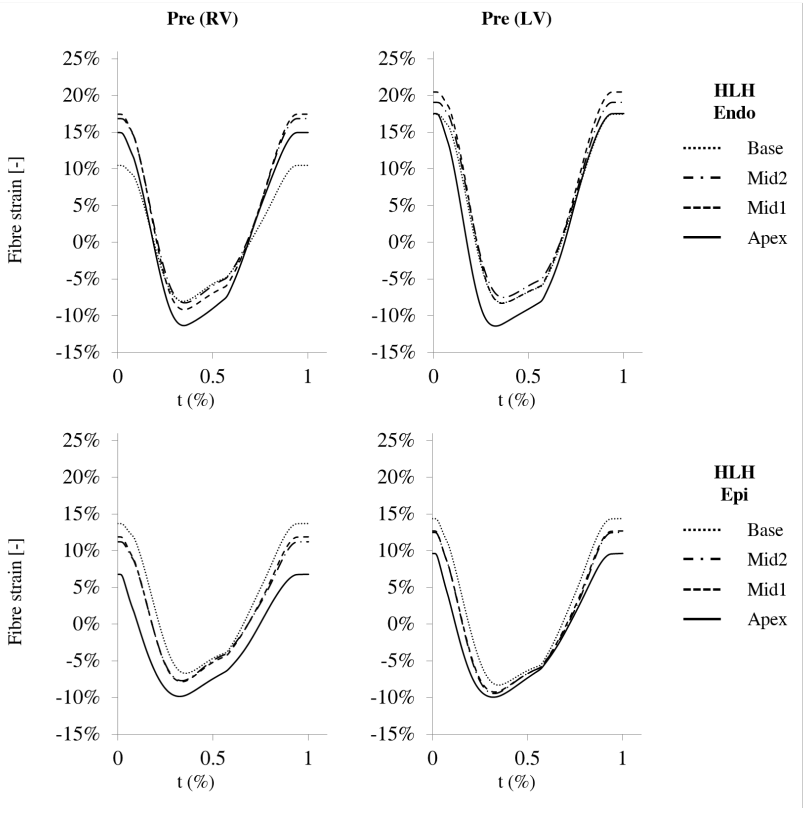

Figure 5.15 Time tracings of the fibre strain obtained from the simulation of pre-operative and post- operative conditions versus the simulations of the LV fibre distributions evaluated at the ventricular apex, ventricular base and at two middle sections (mid1 and mid2) with respect to the ventricular long axis. %Time=normalized cardiac cycle duration. 0 end systole and 1 end diastole.

and Figure 5.17) confirmed the general trends showed from the previous results. As a consequence of the different kinematics the LV configurations showed globally higher strains at end diastole and higher compression strains at both the systolic peak and at end systole. Thus, in this case the sarcomeres are subjected to a higher length variations during the cardiac cycle. Concerning the fibre stresses the LV configurations showed lower values at the systolic peak. This is in agreement to the global hemodynamics results, indeed the LV configuration

generates lower systolic pressures as reported in Table 5.4.

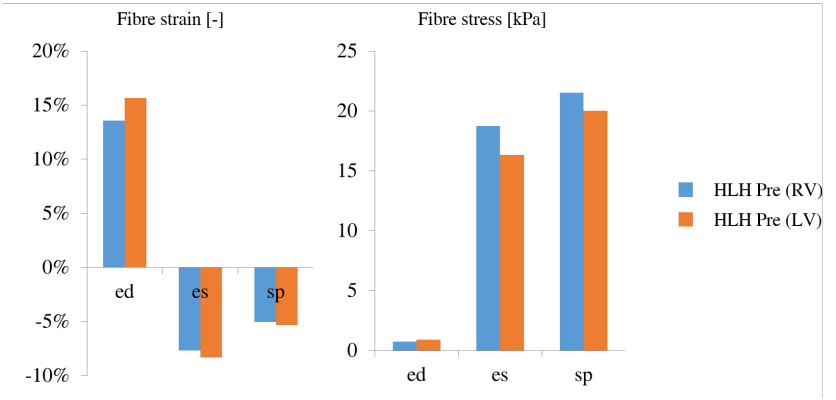

Figure 5.16 Mean fibre strain (left) and stress (right) computed as averaged element value at end diastole (ed), end systole (es) and systolic peak (sp) for the simulation of pre-operative conditions versus the simulations of the LV fibre distributions.

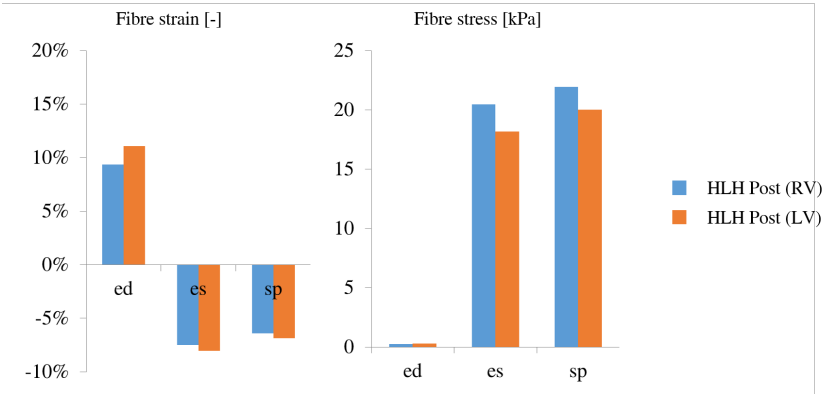

Figure 5.17 Mean fibre strain (left) and stress (right) computed as averaged element value at end diastole (ed), end systole (es) and systolic peak (sp) for the simulation of post-operative conditions versus the simulations of the LV fibre distributions.

5.5 Conclusions

In this chapter the multiscale closed-loop model was used to simulate the surgery of two SV patients. The post-operative state is obtained modifying the connection in the lumped parameter network. In each case, successfully simulations of the surgery were performed, thus allowing a prediction of the operative outcomes. The obtained results are in good agreement with another work reported in literature (Corsini et al., 2014).

In summary, comparing post-operative and pre-operative hemodynamic results we can affirm that: i) stroke volume (i.e. the CO, assuming no change in HR) significantly decreases (about 20-40% depending on the considered patient; ii) the EDV decreases confirming the beneficial effect of the surgery; iii) aortic pressure increases in the mean value; iv) each patient presents specific response to the surgical procedure confirming the need for patient-specific modelling. The regional myocardial results showed an overall reduction in both stress and strain at end diastole confirming the beneficial effect due to the volume unloading after the stage 2 surgery in the acute post-operative condition.

To test the ability of the model in simulating SV circulation also in condition different from the clinical one, additional scenarios were simulated. In particular, active condition and influence of fibre orientations were simulated. All this scenarios are well simulated, in particular for the active state we obtain results in agreement with those reported by another study (Kung et al., 2013) thus increasing the confidence in the multiscale model results. Regarding the effect of the different fibre orientations, while the global hemodynamic performances were not affected by different fibre orientations, the wall kinematics and mechanics showed a clearly different behaviour. Thus, the model supported by additional clinical data could help to gain a more clear understanding of this peculiar conditions.

Chapter 6

General conclusions

6.1 Summary of results

In the present Ph.D. thesis a computational multiscale closed-loop model aimed used to simulate patient-specific biomechanics in the case of SV defect was proposed. The modelling process integrated clinical data, including MR imaging, catheterization and echocardiography, to develop patient-specific models able to account for the main features of the SV patients physiology.

With reference to the main objectives of this work, we successfully built patient-specific multiscale closed-loop models that couple a 3D FE model of SV mechanics to a lumped parameter model of the whole circulatory system. A sequential approach involved distinct steps was defined to identify patient-specific parameters that involve the use of stand alone lumped parameter model and 3D FE model. The approach was then applied to three SV patient-specific cases taken in consideration in this work. Once the models were properly set-up the pre-operative of such patients was successfully simulated. For two SV patients with different pathologies (HRHS and HLHS) good agreement was found in comparison with the pre-operative clinical data of the patients with errors in the main hemodynamic quantities lower than 5%.

The multiscale model was then used to simulate the stage 2 surgery to predict the surgical outcomes of the treatment. The post-operative simulations of the three patients were successfully performed by modifying the circulatory layout accordingly with the changes implied in the surgical procedure. Comparing post-operative and pre-operative hemodynamic results we found a decrease in the CO associated with a decrease in the EDV and a conversely increase of the aortic pressures. This changes are expected due to the volume unloading consequence of the surgery and in agreement with a literature study (Corsini et al., 2014). The regional myocardial results showed an overall reduction in both stress and strain at end diastole confirming the beneficial effect due to the volume unloading after the stage 2 surgery in the acute post-operative condition.

Finally additional scenarios was simulated to test the ability of the model in simulating SV circulations also in condition different from the clinical one. In particular, active condition and influence of fibre orientation were simulated. All this scenarios are well simulated, in particular for the active state we obtain results in agreement with those reported by another literature study (Kung et al., 2013) thus increasing the confidence in the multiscale model results. Regarding the effect of the different fibre orientations, the global hemodynamic performances were not affected by different fibre orientations. However the wall kinematics and mechanics showed peculiar beavhiour depending on the fibre orientations suggesting that the use of the model supported by additional

clinical data could help in achieving deep understanding of this peculiar conditions. In future works the simulation of others additional scenarios as the presence of valve regurgitation or coarctation (often associated to HHS) could be take in to account in the modeling process to evaluate their effect on to the SV cardiac functionality.

6.2 Limitations and possible applications

The proposed computational framework represents a robust tool to couple a patient-specific 3D model of SV and an LP model of the circulatory network. The framework easily enables the simulation of different circulatory models to describe several surgical treatment scenarios. Nevertheless, the model presents some limitations. First, the main limitation of this study is that the model results were not validated against clinical data. The model parameters were identified to replicate the pre-operative patient haemodynamic quantities. Concerning the pre-operative state, a validation process will be performed as soon as more detailed clinical data (e.g. four-dimensional displacement field of the myocardium) are available for stage 1 patients. Regarding the post-operative results, no data were collected for the investigated patient, as they would require invasive and unnecessary clinical exams. In addition, the simulations of the surgical treatment were performed assuming unchanged material and circulatory model parameters. However, no quantitative information is presently available to describe possible active changes or adaptations of the cardiovascular system in this kind of paediatric patients. Second, owing to the lack of patient-specific measurement, a fibre architecture consistent with the literature physiological data was assumed. Fibre orientation in pathological conditions may be significantly different with respect to the physiological case. Moreover, the estimation of the material anisotropy may be incorrect. To this issue, the combination of the 3D cine MR images measurement with the already available clinical data can provide important information. Indeed, the four-dimensional displacement field of the myocardium might be used to validate our assumptions. Regarding the simulation of the active state, only changes in resitances and compliances of the circulatory layout and an increase in the heart rate of the patient are adopted to describe an active state. However, the finality of the simulation was to show the ability of the model in simulating a condition different from the clinical state even though in a simplified manner.

The multiscale model presented might be useful in the evaluation of the acute post-operative outcomes. Indeed, the surgical procedure leads to an abrupt alteration of the working conditions of the SV which are typically hardly pre-

dictable. In addition, the timing of the surgical treatment is critical and based on the clinical experience of the surgeons. In this view, the multiscale model can be used to simulate a number of different surgical scenarios, thus providing important information to assist the surgeon in the decision-making process. Moreover, this information can help customize the post-operative pharmacological treatment. The systematic application of this methodology to a number of SV patients could provide further insights into material properties and fibre orientation data for this pathology, still lacking in the literature. Indeed, the material parameters and fibre orientation could be calibrated, so that the kinematic outcomes of the multiscale model (i.e. myocardial wall displacement and deformation) reproduce the four-dimensional displacement field of the patient. In addition, the study of the two different groups of SV patients (HLHS and HRHS) could highlight both inter- and intragroup variability, thus improving the understanding of such a complex pathology.

Bibliography

Aguado-Sierra, J., Krishnamurthy, A., Villongco, C., Chuang, J., Howard, E., Gonzales, M., Omens, J., Krummen, D., Narayan, S., Kerckhoffs, R., and McCulloch, A. (2011). Patient-specific modeling of dyssynchronous heart failure: A case study. *Progress in Biophysics and Molecular Biology*, 107(1):147–155.

Alboliras, E., Chin, A., Barber, G., Helton, J., Pigott, J., and Norwood, W. (1989). Pulmonary artery configuration after palliative operations for hypoplastic left heart symdrome. *Journal of Thoracic and Cardiovascular Surgery*, 97(6):878–885.

Algra, S., Breur, J., Evens, F., de Roo, F., Schoof, P., and Haas, F. (2011). Improving surgical outcome following the norwood procedure. *Netherlands Heart Journal*, 19(9):369–372.

Alsoufi, B., Bennetts, J., Verma, S., and Caldarone, C. (2007). New developments in the treatment of hypoplastic left heart syndrome. *Pediatrics*, 119(1):109–117.

Armour, J. and Randall, W. (1970). Structural basis for cardiac function. *The American journal of physiology*, 218(6):1517–1523.

Arts, T., Bovendeerd, P., Prinzen, F., and Reneman, R. (1991). Relation between left ventricular cavity pressure and volume and systolic fiber stress and strain in the wall. *Biophysical Journal*, 59(1):93–102.

Arts, T., Veenstra, P., and Reneman, R. (1982). Epicardial deformation and left ventricular wall mechanisms during ejection in the dog. *The American journal of physiology*, 243(3):H379–390.

Babuska, I. and Oden, J. (2004). Verification and validation in computational engineering and science: Basic concepts. *Computer Methods in Applied Mechanics and Engineering*, 193(36-38):4057–4066.

Bailey, L., Nehlsen-Cannarella, S., Doroshow, R., Jacobson, J., Martin, R., Allard, M., Hyde, M., Dang Bui, R., and Petry, E. (1986). Cardiac allotransplantation in newborns as therapy for hypoplastic left heart syndrome. *New England Journal of Medicine*, 315(15):949–951.

Baker, C., Corsini, C., Cosentino, D., Dubini, G., Pennati, G., Migliavacca, F., and Hsia, T.-Y. (2013). Effects of pulmonary artery banding and retrograde aortic arch obstruction on the hybrid palliation of hypoplastic left heart syndrome. *Journal of Thoracic and Cardiovascular Surgery*, 146(6):1341–1348.

Bardo, D., Frankel, D., Applegate, K., Murphy, D., and Saneto, R. (2001). Hypoplastic left heart syndrome. *Radiographics*, 21(3):705–717.

Baretta, A. (2014). *Patient-specific modeling of the cardiovascular system for surgical planning of single-ventricle defects*. PhD thesis, Department of Electronics, Information and Bioengineering, School of Bioengineering, Politecnico di Milano.

Baretta, A., Corsini, C., Marsden, A., Vignon-Clementel, I., Hsia, T.-Y., Dubini, G., Migliavacca, F., and Pennati, G. (2012). Respiratory effects on hemodynamics in patient-specific CFD models of the Fontan circulation under exercise conditions. *European Journal of Mechanics, B/Fluids*, 35:61–69.

Baretta, A., Corsini, C., Yang, W., Vignon-Clementel, I., Marsden, A., Feinstein, J., Hsia, T.-Y., Dubini, G., Migliavacca, F., and Pennati, G. (2011). Virtual surgeries in patients with congenital heart disease: A multi-scale modelling test case. *Philosophical Transactions of the Royal Society A: Mathematical, Physical and Engineering Sciences*, 369(1954):4316–4330.

Barnea, O., Santamore, W., Rossi, A., Salloum, E., Chien, S., and Austin, E. (1998). Estimation of oxygen delivery in newborns with a univentricular circulation. *Circulation*, 98(14):1407–1413.

Berg, K., Berg, W., and Graham, F. (1971). Infant heart rate response as a function of stimulus and state. *Psychophysiology*, 8(1):30–44.

Biglino, G., Giardini, A., Ntsinjana, H., Schievano, S., Hsia, T.-Y., and Taylor, A. (2014). Ventriculoarterial coupling in palliated hypoplastic left heart

syndrome: Noninvasive assessment of the effects of surgical arch reconstruction and shunt type. *Journal of Thoracic and Cardiovascular Surgery*, 148(4):1526–1533.

Biglino, G., Schievano, S., Steeden, J., Ntsinjana, H., Baker, C., Khambadkone, S., De Leval, M., Hsia, T.-Y., Taylor, A., and Giardini, A. (2012a). Reduced ascending aorta distensibility relates to adverse ventricular mechanics in patients with hypoplastic left heart syndrome: Noninvasive study using wave intensity analysis. *Journal of Thoracic and Cardiovascular Surgery*, 144(6):1307–1314.

Biglino, G., Steeden, J., Baker, C., Schievano, S., Taylor, A., Parker, K., and Muthurangu, V. (2012b). A non-invasive clinical application of wave intensity analysis based on ultrahigh temporal resolution phase-contrast cardiovascular magnetic resonance. *Journal of Cardiovascular Magnetic Resonance*, 14(1).

Bove, E., De Leval, M., Migliavacca, F., Guadagni, G., and Dubini, G. (2003). Computational fluid dynamics in the evaluation of hemodynamic performance of cavopulmonary connections after the Norwood procedure for hypoplastic left heart syndrome. *Journal of Thoracic and Cardiovascular Surgery*, 126(4):1040–1047.

Bovendeerd, P., Arts, T., Huyghe, J., van Campen, D., and Reneman, R. (1992). Dependence of local left ventricular wall mechanics on myocardial fiber orientation: A model study. *Journal of Biomechanics*, 25(10):1129–1140.

Bronzino, J. (2006). *Biomedical Engineering Fundamentals*. The Biomedical Engineering Handbook, Fourth Edition. CRC Press.

Brutsaert, D. and Sonnenblick, E. (1971). Nature of the force-velocity relation in heart muscle. *Cardiovascular Research*, 5(SUPP1):18–33.

Cheng, Y., Oertel, H., and Schenkel, T. (2005). Fluid-structure coupled CFD simulation of the left ventricular flow during filling phase. *Annals of Biomedical Engineering*, 33(5):567–576.

Clausen, H. (2015). Hypoplastic left heart syndrome. *Paediatrics and Child Health*, 25(1):18–22.

Corsini, C., Baker, C., Kung, E., Schievano, S., Arbia, G., Baretta, A., Biglino, G., Migliavacca, F., Dubini, G., Pennati, G., Marsden, A., Vignon-Clementel,

I., Taylor, A., Hsia, T.-Y., and Dorfman, A. (2014). An integrated approach to patient-specific predictive modeling for single ventricle heart palliation. *Computer Methods in Biomechanics and Biomedical Engineering*, 17(14):1572–1589.

Costa, K., Holmes, J., and McCulloch, A. (2001). Modelling cardiac mechanical properties in three dimensions. *Philosophical Transactions of the Royal Society A: Mathematical, Physical and Engineering Sciences*, 359(1783):1233–1250.

Danielsen, M. and Ottesen, J. (2001). Describing the pumping heart as a pressure source. *Journal of Theoretical Biology*, 212(1):71–81.

De Leval, M. and Deanfield, J. (2010). Four decades of Fontan palliation. *Nature Reviews Cardiology*, 7(9):520–527.

De Tombe, P. and Ter Keurs, H. (1990). Force and velocity of sarcomere shortening in trabeculae from rat heart. Effects of temperature. *Circulation Research*, 66(5):1239–1254.

De Vecchi, A., Gomez, A., Pushparajah, K., Schaeffter, T., Nordsletten, D., Simpson, J., Penney, G., and Smith, N. (2014). Towards a fast and efficient approach for modelling the patient-specific ventricular haemodynamics. *Progress in Biophysics and Molecular Biology*, 116(1):3–10.

De Vecchi, A., Nordsletten, D., Razavi, R., Greil, G., and Smith, N. (2013). Patient specific fluid-structure ventricular modelling for integrated cardiac care. *Medical and Biological Engineering and Computing*, 51(11):1261–1270.

De Vecchi, A., Nordsletten, D., Remme, E., Bellsham-Revell, H., Greil, G., Simpson, J., Razavi, R., and Smith, N. (2012). Inflow typology and ventricular geometry determine efficiency of filling in the hypoplastic left heart. *Annals of Thoracic Surgery*, 94(5):1562–1569.

De Zélicourt, D., Pekkan, K., Parks, J., Kanter, K., Fogel, M., and Yoganathan, A. (2006). Flow study of an extracardiac connection with persistent left superior vena cava. *Journal of Thoracic and Cardiovascular Surgery*, 131(4):785–791.

Demer, L. and Yin, F. (1983). Passive biaxial mechanical properties of isolated canine myocardium. *Journal of Physiology*, Vol. 339:615–630.

Dillman, J., Dorfman, A., Attili, A., Agarwal, P., Bell, A., Mueller, G., and Hernandez, R. (2010). Cardiovascular magnetic resonance imaging of hypoplastic left heart syndrome in children. *Pediatric Radiology*, 40(3):261–274.

Dokos, S., Smaill, B., Young, A., and LeGrice, I. (2002). Shear properties of passive ventricular myocardium. *American Journal of Physiology - Heart and Circulatory Physiology*, 283(6 52-6):H2650–H2659.

Dur, O., Lara, M., Arnold, D., Vandenberghe, S., Keller, B., Degroff, C., and Pekkan, K. (2009). Pulsatile in vitro simulation of the pediatric univentricular circulation for evaluation of cardiopulmonary assist scenarios. *Artificial Organs*, 33(11):967–976.

Fox, C. and Hutchins, G. (1972). The architecture of the human ventricular myocardium. *Johns Hopkins Medical Journal*, 130(5):289–299.

Gaca, A., Jaggers, J., Dudley, L., and Bisset III, G. (2008). Repair of congenital heart disease: A primer-part 1. *Radiology*, 247(3):617–631.

Galantowicz, M., Cheatham, J., Phillips, A., Cua, C., Hoffman, T., Hill, S., and Rodeman, R. (2008). Hybrid Approach for Hypoplastic Left Heart Syndrome: Intermediate Results After the Learning Curve. *Annals of Thoracic Surgery*, 85(6):2063–2071.

Gao, H., Carrik, D., Berry, C., Griffith, B., and Luo, X. (2014a). Dynamic finite-strain modelling of the human left ventricle in health and disease using an immersed boundary-finite element method. *IMA Journal of Applied Mathematics*, 79(5):978–1010.

Gao, H., Wang, H., Berry, C., Luo, X., and Griffith, B. (2014b). Quasi-static image-based immersed boundary-finite element model of left ventricle under diastolic loading. *International Journal for Numerical Methods in Biomedical Engineering*, 30(11):1199–1222.

Gemignani, V., Bianchini, E., Faita, F., Giannoni, M., Pasanisi, E., Picano, E., and Bombardini, T. (2008). Assessment of cardiologic systole and diastole duration in exercise stress tests with a transcutaneous accelerometer sensor. *Computers in Cardiology*, 35:153–156.

Gould, P., Ghista, D., Brombolich, L., and Mirsky, I. (1972). In vivo stresses in the human left ventricular wall: Analysis accounting for the irregular 3-dimensional geometry and comparison with idealised geometry analyses. *Journal of Biomechanics*, 5(5):521–522,IN13,523–539.

Greenbaum, R., Ho, S., Gibson, D., Becker, A., and Anderson, R. (1981). Left ventricular fibre architecture in man. *British Heart Journal*, 45(3):248–263.

Guadagni, G., Bove, E., Migliavacca, F., and Dubini, G. (2001). Effects of pulmonary afterload on the hemodynamics after the hemi-Fontan procedure. *Medical Engineering and Physics*, 23(5):293–298.

Guccione, J., Costa, K., and McCulloch, A. (1995). Finite element stress analysis of left ventricular mechanics in the beating dog heart. *Journal of Biomechanics*, 28(10):1167–1177.

Guccione, J., Salahieh, A., Moonly, S., Kortsmit, J., Wallace, A., and Ratcliffe, M. (2003). Myosplint decreases wall stress without depressing function in the failing heart: A finite element model study. *Annals of Thoracic Surgery*, 76(4):1171–1180.

Helm, P., Beg, M., Miller, M., and Winslow, R. (2005). Measuring and mapping cardiac fiber and laminar architecture using diffusion tensor MR imaging. *Annals of the New York Academy of Sciences*, 1047:296–307.

Hill, A. (1938). The Heat of Shortening and the Dynamic Constants of Muscle. *Proceedings of the Royal Society of London. Series B, Biological Science.*, 126:136–165.

Hill, A. (1970). *First and Last Experiments in Muscle Mechanics*. University Press, Cambridge.

Holzapfel, G. (2000). *Nonlinear Solid Mechanics: A Continuum Approach for Engineering*. Wiley, Chichester, UK.

Holzapfel, G. and Ogden, R. (2009). Constitutive modelling of passive myocardium: A structurally based framework for material characterization. *Philosophical Transactions of the Royal Society A: Mathematical, Physical and Engineering Sciences*, 367(1902):3445–3475.

Horowitz, A., Lanir, Y., Pin, F., Perl, M., Sheinman, I., and Strumpf, R. (1988). Structural three-dimensional constitutive law for the passive myocardium. *Journal of Biomechanical Engineering*, 110(3):200–207.

Hort, W. (1957). Mikrometrische Untersuchungen an verschieden weiten Meerschweinchenherzen. *Verhandlungen der Deutschen Gesellschaft für Kreislaufforschung*, 23(343-346).

Hsia, T.-Y., Migliavacca, F., Pittaccio, S., Radaelli, A., Dubini, G., Pennati, G., and De Leval, M. (2004). Computational fluid dynamic study of flow optimization in realistic models of the total cavopulmonary connections. *Journal of Surgical Research*, 116(2):305–313.

Huber, C., Tozzi, P., Corno, A., Marty, B., Ruchat, P., Gersbach, P., Nasratulla, M., and Von Segesser, L. (2004). Do valved stents compromise coronary flow? *European Journal of Cardio-thoracic Surgery*, 25(5):754–759.

Humphrey, J., Strumpf, R., and Yin, F. (1990a). Determination of a constitutive relation for passive myocardium: I. A new functional form. *Journal of Biomechanical Engineering*, 112(3):333–339.

Humphrey, J., Strumpf, R., and Yin, F. (1990b). Determination of a constitutive relation for passive myocardium: II. - Parameter estimation. *Journal of Biomechanical Engineering*, 112(3):340–346.

Hunter, P. (1975). *Finite Element Analysis of Cardiac Muscle Mechanics*. PhD thesis, University of Oxford.

Hunter, P., McCulloch, A., and ter Keurs, H. (1998). Modelling the mechanical properties of cardiac muscle. *Progress in Biophysics and Molecular Biology*, 69(2-3):289–331.

Huxley, A. (1957). Muscle Structure and Theories of Contraction. *Progress in Biophysics and Biophysical Chemistry*, 7:255–318.

Huyghe, J., Arts, T., Van Campen, D., and Reneman, R. (1992). Porous medium finite element model of the beating left ventricle. *American Journal of Physiology - Heart and Circulatory Physiology*, 262(4 31-4):H1256–H1267.

Janssen, P. and Hunter, W. (1995). Force, not sarcomere length, correlates with prolongation of isosarcometric contraction. *American Journal of Physiology - Heart and Circulatory Physiology*, 269(2 38-2):H676–H685.

Janz, R. and Grimm, A. (1972). Finite-element model for the mechanical behavior of the left ventricle. Prediction of deformation in the potassium-arrested rat heart. *Circulation Research*, 30(2):244–252.

Janz, R., Kubert, B., Moriarty, T., and Grimm, A. (1974). Deformation of the diastolic left ventricle. II. Nonlinear geometric effects. *Journal of Biomechanics*, 7(6):509–516.

Karlon, W., Covell, J., McCulloch, A., Hunter, J., and Omens, J. (1998). Automated measurement of myofiber disarray in transgenic mice with ventricular expression of ras. *Anatomical Record*, 252(4):612–625.

Katz, L. and Feil, H. (1923). Clinical observations on the dynamics of ventricular systole. I. auricular fibrillation. *Archives of Internal Medicine*, 32(5):672–692.

Kentish, J., Ter Keurs, H., Ricciardi, L., Bucx, J., and Noble, M. (1986). Comparison between the sarcomere length-force relations of intact and skinned trabeculae from rat right ventricle. Influence of calcium concentrations on these relations. *Circulation Research*, 58(6):755–768.

Kerckhoffs, R. (2012). Computational modeling of cardiac growth in the post-natal rat with a strain-based growth law. *Journal of Biomechanics*, 45(5):865–871.

Kerckhoffs, R., Bovendeerd, P., Kotte, J., Prinzen, F., Smits, K., and Arts, T. (2003a). Homogeneity of cardiac contraction despite physiological asynchrony of depolarization: A model study. *Annals of Biomedical Engineering*, 31(5):536–547.

Kerckhoffs, R., Bovendeerd, P., Prinzen, F., Smits, K., and Arts, T. (2003b). Intra- and interventricular asynchrony of electromechanics in the ventricularly paced heart. *Journal of Engineering Mathematics*, 47(3-4):201–216.

Kerckhoffs, R., Healy, S., Usyk, T., and McCulloch, A. (2006). Computational methods for cardiac electromechanics. *Proceedings of the IEEE*, 94(4):769–782.

Kerckhoffs, R., McCulloch, A., Omens, J., and Mulligan, L. (2009). Effects of biventricular pacing and scar size in a computational model of the failing heart with left bundle branch block. *Medical Image Analysis*, 13(2):362–369.

Kerckhoffs, R., Neal, M., Gu, Q., Bassingthwaighte, J., Omens, J., and McCulloch, A. (2007). Coupling of a 3D finite element model of cardiac ventricular mechanics to lumped systems models of the systemic and pulmonic circulation. *Annals of Biomedical Engineering*, 35(1):1–18.

Kerckhoffs, R., Omens, J., and McCulloch, A. (2012). A single strain-based growth law predicts concentric and eccentric cardiac growth during pressure and volume overload. *Mechanics Research Communications*, 42:40–50.

Kerckhoffs, R., Omens, J., McCulloch, A., and Mulligan, L. (2010). Ventricular dilation and electrical dyssynchrony synergistically increase regional mechanical nonuniformity but not mechanical dyssynchrony: A computational model. *Circulation: Heart Failure*, 3(4):528–536.

Khairy, P., Poirier, N., and Mercier, L.-A. (2007). Univentricular heart. *Circulation*, 115(6):800–812.

Khunatorn, Y., Mahalingam, S., DeGroff, C., and Shandas, R. (2002). Influence of connection geometry and SVC-IVC flow rate ratio on flow structures within the total cavopulmonary connection: A numerical study. *Journal of Biomechanical Engineering*, 124(4):364–377.

Klotz, S., Hay, I., Dickstein, M., Yi, G.-H., Wang, J., Maurer, M., Kass, D., and Burkhoff, D. (2006). Single-beat estimation of end-diastolic pressure-volume relationship: A novel method with potential for noninvasive application. *American Journal of Physiology - Heart and Circulatory Physiology*, 291(1):H403–H412.

Kortsmit, J., Davies, N., Miller, R., Macadangdang, J., Zilla, P., and Franz, T. (2013). The effect of hydrogel injection on cardiac function and myocardial mechanics in a computational post-infarction model. *Computer Methods in Biomechanics and Biomedical Engineering*, 16(11):1185–1195.

Krishnamurthy, A., Villongco, C., Chuang, J., Frank, L., Nigam, V., Belezzuoli, E., Stark, P., Krummen, D., Narayan, S., Omens, J., McCulloch, A., and Kerckhoffs, R. (2013). Patient-specific models of cardiac biomechanics. *Journal of Computational Physics*, 244:4–21.

Kung, E., Baretta, A., Baker, C., Arbia, G., Biglino, G., Corsini, C., Schievano, S., Vignon-Clementel, I., Dubini, G., Pennati, G., Taylor, A., Dorfman, A., Hlavacek, A., Marsden, A., Hsia, T.-Y., and Migliavacca, F. (2013). Predictive modeling of the virtual Hemi-Fontan operation for second stage single ventricle palliation: Two patient-specific cases. *Journal of Biomechanics*, 46(2):423–429.

Laganà, K., Balossino, R., Migliavacca, F., Pennati, G., Bove, E. L., de Leval, M. R., and Dubini, G. (2005). Multiscale modeling of the cardiovascular system: application to the study of pulmonary and coronary perfusions in the univentricular circulation. *Journal of Biomechanics*, 38(5):1129–1141.

Landesberg, A., Livshitz, L., and Ter Keurs, H. (2000). Effect of sarcomere shortening velocity on force generation, analysis, and verification of models

for crossbridge dynamics. *Annals of Biomedical Engineering*, 28(8):968–978.

Landesberg, A. and Sideman, S. (1994). Mechanical regulation of cardiac muscle by coupling calcium kinetics with cross-bridge cycling: A dynamic model. *American Journal of Physiology - Heart and Circulatory Physiology*, 267(2 36-2):H779–H795.

Lee, L., Ge, L., Zhang, Z., Pease, M., Nikolic, S., Mishra, R., Ratcliffe, M., and Guccione, J. (2014). Patient-specific finite element modeling of the Cardiokinetix Parachute® device: Effects on left ventricular wall stress and function. *Medical and Biological Engineering and Computing*, 52(6):557–566.

LeGrice, I., Hunter, P., and Smaill, B. (1997). Laminar structure of the heart: A mathematical model. *American Journal of Physiology - Heart and Circulatory Physiology*, 272(5 41-5):H2466–H2476.

LeGrice, I., Takayama, Y., and Covell, J. (1995). Transverse shear along myocardial cleavage planes provides a mechanism for normal systolic wall thickening. *Circulation Research*, 77(1):182–193.

Lemmon, J. and Yoganathan, A. (2000). Computational modeling of left heart diastolic function: Examination of ventricular dysfunction. *Journal of Biomechanical Engineering*, 122(4):297–303.

Lin, D. and Yin, F. (1998). A multiaxial constitutive law for mammalian left ventricular myocardium in steady-state barium contracture or tetanus. *Journal of Biomechanical Engineering*, 120(4):504–517.

Lumens, J., Delhaas, T., Kirn, B., and Arts, T. (2009). Three-wall segment (TriSeg) model describing mechanics and hemodynamics of ventricular interaction. *Annals of Biomedical Engineering*, 37(11):2234–2255.

Marsden, A. L., Bernstein, A. J., Reddy, V. M., Shadden, S. C., Spilker, R. L., Chan, F. P., Taylor, C. A., and Feinstein, J. A. (2009). Evaluation of a novel Y-shaped extracardiac Fontan baffle using computational fluid dynamics. *The Journal of Thoracic and Cardiovascular Surgery*, 137(2):394–403.

McQueen, D. and Peskin, C. (2000). A three-dimensional computer model of the human heart for studying cardiac fluid dynamics. *Computer Graphics (ACM)*, 34(1):56–60.

Meoli, A., Cutrì, E., Krishnamurthy, A., Dubini, G., Migliavacca, F., Hsia, T.-Y., and Pennati, G. (2015). A multiscale model for the study of cardiac biomechanics in the single ventricle surgeries: a clinical case. *Interface Focus*. Accepted for publication.

Migliavacca, F., Balossino, R., Pennati, G., Dubini, G., Hsia, T.-Y., De Leval, M., and Bove, E. (2006). Multiscale modelling in biofluidynamics: Application to reconstructive paediatric cardiac surgery. *Journal of Biomechanics*, 39(6):1010–1020.

Migliavacca, F., De Leval, M., Dubini, G., Pietrabissa, R., and Fumero, R. (1999). Computational fluid dynamic simulations of cavopulmonary connections with an extracardiac lateral conduit. *Medical Engineering and Physics*, 21(3):187–193.

Migliavacca, F., Dubini, G., Bove, E., and De Leval, M. (2003). Computational Fluid Dynamics Simulations in Realistic 3-D Geometries of the Total Cavopulmonary Anastomosis: The Influence of the Inferior Caval Anastomosis. *Journal of Biomechanical Engineering*, 125(6):805–813.

Migliavacca, F., Dubini, G., Pennati, G., Pietrabissa, R., Fumero, R., Hsia, T.-Y., and De Leval, M. (2000a). Computational model of the fluid dynamics in systemic-to-pulmonary shunts. *Journal of Biomechanics*, 33(5):549–557.

Migliavacca, F., Pennati, G., Dubini, G., Fumero, R., Pietrabissa, R., Urcelay, G., Bove, E., Hsia, T.-Y., and De Leval, M. (2001). Modeling of the Norwood circulation: Effects of shunt size, vascular resistances, and heart rate. *American Journal of Physiology - Heart and Circulatory Physiology*, 280(5 49-5):H2076–H2086.

Migliavacca, F., Yates, R., Pennati, G., Dubini, G., Fumero, R., and De Leval, M. (2000b). Calculating blood flow from Doppler measurements in the systemic-to-pulmonary artery shunt after the Norwood operation: A method based on computational fluid dynamics. *Ultrasound in Medicine and Biology*, 26(2):209–219.

Miller, R., Davies, N., Kortsmit, J., Zilla, P., and Franz, T. (2013). Outcomes of myocardial infarction hydrogel injection therapy in the human left ventricle dependent on injectate distribution. *International Journal for Numerical Methods in Biomedical Engineering*, 29(8):870–884.

Muthurangu, V., Taylor, A., Hegde, S., Johnson, R., Tulloh, R., Simpson, J., Qureshi, S., Rosenthal, E., Baker, E., Anderson, D., and Razavi, R. (2005).

Cardiac magnetic resonance imaging after stage I norwood operation for hypoplastic left heart syndrome. *Circulation*, 112(21):3256–3263.

Nash, M. and Hunter, P. (2000). Computational mechanics of the heart. From tissue structure to ventricular function. *Journal of Elasticity*, 61(1-3):113–141.

Nevo, E. and Lanir, Y. (1989). Structural finite deformation model of the left ventricle during diastole and systole. *Journal of Biomechanical Engineering*, 111(4):342–349.

Nickerson, D., Niederer, S., Stevens, C., Nash, M., and Hunter, P. (2006). A computational model of cardiac electromechanics. *Annual International Conference of the IEEE Engineering in Medicine and Biology - Proceedings*, pages 5311–5314.

Nickerson, D., Smith, N., and Hunter, P. (2005). New developments in a strongly coupled cardiac electromechanical model. *Europace*, 7(SUPPL. 2):S118–S127.

Niederer, S., Plank, G., Chinchapatnam, P., Ginks, M., Lamata, P., Rhode, K., Rinaldi, C., Razavi, R., and Smith, N. (2011). Length-dependent tension in the failing heart and the efficacy of cardiac resynchronization therapy. *Cardiovascular Research*, 89(2):336–343.

Niederer, S. and Smith, N. (2009). The Role of the Frank-Starling Law in the Transduction of Cellular Work to Whole Organ Pump Function: A Computational Modeling Analysis. *PLoS Computational Biology*, 5(4).

Nielsen, P., Le Grice, I., Smaill, B., and Hunter, P. (1991). Mathematical model of geometry and fibrous structure of the heart. *American Journal of Physiology - Heart and Circulatory Physiology*, 260(4 29/4):H1365–H1378.

Nordsletten, D., Mccormick, M., Kilner, P., Hunter, P., Kay, D., and Smith, N. (2011). Fluid-solid coupling for the investigation of diastolic and systolic human left ventricular function. *International Journal for Numerical Methods in Biomedical Engineering*, 27(7):1017–1039.

Norwood, W. (1991). Hypoplastic left heart syndrome. *The Annals of Thoracic Surgery*, 52(3):688–695.

Norwood, W., Kirklin, J., and Sanders, S. (1980). Hypoplastic left heart syndrome: Experience with palliative surgery. *The American Journal of Cardiology*, 45(1):87–91.

Norwood, W., Lang, P., and Hansen, D. (1983). Physiologic repair of aortic atresia-hypoplastic left heart syndrome. *New England Journal of Medicine*, 308(1):23–26.

Ogden, R. (1997). *Non-linear elastic deformations*. Dover Publications, New York, NY.

Palit, A., Bhudia, S., Arvanitis, T., Turley, G., and Williams, M. (2015). Computational modelling of left-ventricular diastolic mechanics: Effect of fibre orientation and right-ventricle topology. *Journal of Biomechanics*, 48(4):604–612.

Panda, S. and Natarajan, R. (1977). Finite-element method of stress analysis in the human left ventricular layered wall structure. *Medical & Biological Engineering & Computing*, 15(1):67–71.

Parker, K. (2009). An introduction to wave intensity analysis. *Medical and Biological Engineering and Computing*, 47(2):175–188.

Pekkan, K., Dasi, L., De Zélicourt, D., Sundareswaran, K., Fogel, M., Kanter, K., and Yoganathan, A. (2009). Hemodynamic performance of stage-2 univentricular reconstruction: Glenn vs. Hemi-fontan templates. *Annals of Biomedical Engineering*, 37(1):50–63.

Pekkan, K., Frakes, D., De Zelicourt, D., Lucas, C., Parks, W., and Yoganathan, A. (2005). Coupling pediatric ventricle assist devices to the Fontan circulation: Simulations with a lumped-parameter model. *ASAIO Journal*, 51(5):618–628.

Pennati, G., Migliavacca, F., Dubini, G., Pietrabissa, R., and De Leval, M. (1997). A mathematical model of circulation in the presence of the bidirectional cavopulmonary anastomosis in children with a univentricular heart. *Medical Engineering and Physics*, 19(3):223–234.

Pennati, G., Migliavacca, F., Dubini, G., Pietrabissa, R., Fumero, R., and De Leval, M. (2000). Use of mathematical model to predict hemodynamics in cavopulmonary anastomosis with persistent forward flow. *Journal of Surgical Research*, 89(1):43–52.

Pittaccio, S., Migliavacca, F., Dubini, G., Koçyildirim, E., and de Leval, M. (2005). On the use of computational models for the quantitative assessment of surgery in congenital heart disease. *Anadolu Kardiyoloji Dergisi*, 5(3):202–209.

Regnier, M., Morris, C., and Homsher, E. (1995). Regulation of the cross-bridge transition from a weakly to strongly bound state in skinned rabbit muscle fibers. *American Journal of Physiology - Cell Physiology*, 269(6 38-6):C1532–C1539.

Rice, J., Wang, F., Bers, D., and De Tombe, P. (2008). Approximate model of cooperative activation and crossbridge cycling in cardiac muscle using ordinary differential equations. *Biophysical Journal*, 95(5):2368–2390.

Rodriguez, E., Hoger, A., and McCulloch, A. (1994). Stress-dependent finite growth in soft elastic tissues. *Journal of Biomechanics*, 27(4):455–467.

Ryu, K., Healy, T., Ensley, A., Sharma, S., Lucas, C., and Yoganathan, A. (2001). Importance of accurate geometry in the study of the total cavopulmonary connection: Computational simulations and in vitro experiments. *Annals of Biomedical Engineering*, 29(10):844–853.

Sandler, H. and Dodge, H. (1963). Left ventricular tension and stress in man. *Circulation Research*, 130(2):91–104.

Sano, S., Ishino, K., Kawada, M., Arai, S., Kasahara, S., Asai, T., Masuda, Z.-I., Takeuchi, M., Ohtsuki, S.-I., Litwin, S., Mavroudis, C., Pozzi, M., Pizarro, C., and Lacour-Gayet, F. (2003). Right ventricle-pulmonary artery shunt in first-stage palliation of hypoplastic left heart syndrome. *Journal of Thoracic and Cardiovascular Surgery*, 126(2):504–510.

Sant'Anna, J., Kalil, R., Prates, P. R., Horowitz, E., Sant'Anna, R., Prates, P., and Nesralla, I. (2003). Computer dynamics to evaluate blood flow through the modified Blalock-Taussig shunt. *Revista Brasileira de Cirurgia Cardiovascular*, 18:253–260.

Schmid, H., Nash, M., Young, A., and Hunter, P. (2006). Myocardial material parameter estimation - A comparative study for simple shear. *Journal of Biomechanical Engineering*, 128(5):742–750.

Segers, P., Steendijk, P., Stergiopulos, N., and Westerhof, N. (2001). Predicting systolic and diastolic aortic blood pressure and stroke volume in the intact sheep. *Journal of Biomechanics*, 34(1):41–50.

Smaill, B. and Hunter, P. (1991). Structure and function of the diastolic heart. In L. Glass, P. J. H. and McCulloch, A. D., editors, *Theory of Heart: Biomechanics, Biophysics, and Nonlinear Dynamics of Cardiac Function*, pages 1–29. Springer-Verlag, New York.

Song, M.-H., Sato, M., and Ueda, Y. (2001). Three-dimensional simulation of the Blalock-Taussig shunt using computational fluid dynamics. *Surgery Today*, 31(8):688–694.

Spotnitz, H., Spotnitz, W., Cottrell, T., Spiro, D., and Sonnenblick, E. (1974). Cellular basis for volume related wall thickness changes in the rat left ventricle. *Journal of Molecular and Cellular Cardiology*, 6(4):317–322,IN1–IN3,323–331.

Stevens, C. and Hunter, P. (2003). Sarcomere length changes in a 3D mathematical model of the pig ventricles. *Progress in Biophysics and Molecular Biology*, 82(1-3):229–241.

Stevens, C., Remme, E., LeGrice, I., and Hunter, P. (2003). Ventricular mechanics in diastole: Material parameter sensitivity. *Journal of Biomechanics*, 36(5):737–748.

Streeter Jr., D. (1979). Gross morphology and fiber geometry of the heart. In Society, A. P., editor, *Handbook of Physiology (Section 2: The Cardiovascular System. Vol. 1: The Heart)*. Williams and Wilkins Company, Baltimore.

Streeter Jr., D. and Bassett, D. (1966). An engineering analysis of myocardial fiber orientation in pig's left ventricle in systole. *The Anatomical Record*, 155:503–511.

Streeter Jr., D., Spotnitz, H., Patel, D., Ross Jr., J., and Sonnenblick, E. (1969). Fiber orientation in the canine left ventricle during diastole and systole. *Circulation Research*, 24(3):339–347.

Suga, H., Sagawa, K., and Shoukas, A. (1973). Load independence of the instantaneous pressure-volume ratio of the canine left ventricle and effects of epinephrine and heart rate on the ratio. *Circulation Research*, 32(3):314–322.

Sun, K., Stander, N., Jhun, C.-S., Zhang, Z., Suzuki, T., Wang, G.-Y., Saeed, M., Wallace, A., Tseng, E., Baker, A., Saloner, D., Einstein, D., Ratcliffe, M., and Guccione, J. (2009). A computationally efficient formal optimization of regional myocardial contractility in a sheep with left ventricular aneurysm. *Journal of Biomechanical Engineering*, 131(11).

Sundareswaran, K., Pekkan, K., Dasi, L., Whitehead, K., Sharma, S., Kanter, K., Fogel, M., and Yoganathan, A. (2008). The total cavopulmonary connection resistance: A significant impact on single ventricle hemodynamics at rest and exercise. *American Journal of Physiology - Heart and Circulatory Physiology*, 295(6):H2427–H2435.

Tacy, T., Whitehead, K., and Cape, E. (1998). In vitro Doppler assessment of pressure gradients across modified Blalock-Taussig shunts. *American Journal of Cardiology*, 81(10):1219–1223.

Tang, D., Yang, C., Geva, T., and del Nido, P. (2010). Image-based patient-specific ventricle models with fluid-structure interaction for cardiac function assessment and surgical design optimization. *Progress in Pediatric Cardiology*, 30(1-2):51–62.

Trumble, D., McGregor, W., Kerckhoffs, R., and Waldman, L. (2011). Cardiac assist with a twist: Apical torsion as a means to improve failing heart function. *Journal of Biomechanical Engineering*, 133(10).

Ursino, M. (1998). Interaction between carotid baroregulation and the pulsating heart: A mathematical model. *American Journal of Physiology - Heart and Circulatory Physiology*, 44(5):H1733–H1747.

Usyk, T. and McCulloch, A. (2003a). Computational Methods for Soft Tissue Biomechanics. In *Biomechanics of Soft Tissue in Cardiovascular Systems*. Springer-Verlag, Wien.

Usyk, T. and McCulloch, A. (2003b). Electromechanical Model of Cardiac Resynchronization in the Dilated Failing Heart with Left Bundle Branch Block. *Journal of Electrocardiology*, 36(SUPPL.):57–61.

Usyk, T. and McCulloch, A. (2003c). Relationship between Regional Shortening and Asynchronous Electrical Activation in a Three-Dimensional Model of Ventricular Electromechanics. *Journal of Cardiovascular Electrophysiology*, 14(10 SUPPL.):S196–S202.

Van Haesdonck, J.-M., Mertens, L., Sizaire, R., Montas, G., Purnode, B., Daenen, W., Crochet, M., and Gewillig, M. (1995). Comparison by computerized numeric modeling of energy losses in different Fontan connections. *Circulation*, 92(9):II322–II326.

Vendelin, M., Bovendeerd, P., Engelbrecht, J., and Arts, T. (2002). Optimizing ventricular fibers: Uniform strain or stress, but not ATP consumption, leads to high efficiency. *American Journal of Physiology - Heart and Circulatory Physiology*, 283(3 52-3):H1072–H1081.

Vetter, F. and McCulloch, A. (2000). Three-Dimensional Stress and Strain in Passive Rabbit Left Ventricle: A Model Study. *Annals of Biomedical Engineering*, 28(7):781–792.

Vierendeels, J., Riemslagh, K., Dick, E., and Verdonck, P. (1999). Computer simulation of left ventricular filling flow: Impact study on echocardiograms. *Computers in Cardiology*, 26:177–180.

Vierendeels, J., Riemslagh, K., Dick, E., and Verdonck, P. (2000). Computer simulation of intraventricular flow and pressure gradients during diastole. *Journal of Biomechanical Engineering*, 122(6):667–674.

Walker, J., Ratcliffe, M., Zhang, P., Wallace, A., Fata, B., Hsu, E., Saloner, D., and Guccione, J. (2005). MRI-based finite-element analysis of left ventricular aneurysm. *American Journal of Physiology - Heart and Circulatory Physiology*, 289(2 58-2):H692–H700.

Walker, J., Ratcliffe, M., Zhang, P., Wallace, A., Hsu, E., Saloner, D., and Guccione, J. (2008). Magnetic resonance imaging-based finite element stress analysis after linear repair of left ventricular aneurysm. *Journal of Thoracic and Cardiovascular Surgery*, 135(5):1094–1102.e2.

Wang, H., Gao, H., Luo, X., Berry, C., Griffith, B., Ogden, R., and Wang, T. (2013). Structure-based finite strain modelling of the human left ventricle in diastole. *International Journal for Numerical Methods in Biomedical Engineering*, 29(1):83–103.

Wang, V., Lam, H., Ennis, D., Cowan, B., Young, A., and Nash, M. (2009). Modelling passive diastolic mechanics with quantitative MRI of cardiac structure and function. *Medical Image Analysis*, 13(5):773–784.

Waniewski, J., Kurowska, W., Mizerski, J., Trykozko, A., Nowiński, K., Brzezińska-Rajszys, G., and Kościesza, A. (2005). The effects of graft geometry on the patency of a systemic-to-pulmonary shunt: A computational fluid dynamics study. *Artificial Organs*, 29(8):642–650.

Watanabe, H., Hisada, T., Sugiura, S., Okada, J.-I., and Fukunari, H. (2002). Computer simulation of blood flow, left ventricular wall motion and their interrelationship by fluid-structure interaction finite element method. *JSME International Journal, Series C: Mechanical Systems, Machine Elements and Manufacturing*, 45(4):1003–1012.

Watanabe, H., Sugiura, S., Kafuku, H., and Hisada, T. (2004). Multiphysics simulation of left ventricular filling dynamics using fluid-structure interaction finite element method. *Biophysical Journal*, 87(3):2074–2085.

Wenk, J., Sun, K., Zhang, Z., Soleimani, M., Ge, L., Saloner, D., Wallace, A., Ratcliffe, M., and Guccione, J. (2011). Regional left ventricular myocardial contractility and stress in a finite element model of posterobasal myocardial infarction. *Journal of biomechanical engineering*, 133(4):044501.

Wong, A. and Rautaharju, P. (1968). Stress distribution within the left ventricular wall approximated as a thick ellipsoidal shell. *American Heart Journal*, 75(5):649–662.

Xia, L., Huo, M., Wei, Q., Liu, F., and Crozier, S. (2005). Analysis of cardiac ventricular wall motion based on a three-dimensional electromechanical biventricular model. *Physics in Medicine and Biology*, 50(8):1901–1917.

Yin, F., Strumpf, R., Chew, P., and Zeger, S. (1987). Quantification of the mechanical properties of noncontracting canine myocardium under simultaneous biaxial loading. *Journal of Biomechanics*, 20(6):577–589.

Yuan, S.-M., Shinfeld, A., and Raanani, E. (2009). The blalock-taussig shunt: Short communication. *Journal of Cardiac Surgery*, 24(2):101–108.

List of Figures

List of Tables

Publications

Papers

Meoli, A., Cutrì, E., Krishnamurty, A., Dubini, G., Migliavacca, F., Hsia, T.Y., Pennati, G. and the Modeling of Congenital Hearts Alliance (MOCHA) (2015). A multiscale model for the study of cardiac biomechanics in the single ventricle surgeries: a clinical case. *Interface Focus*, 6;5(2):20140079.

Meoli, A., Dordoni, E., Petrini, P., Migliavacca, F., Dubini, G., and Pennati, G. (2014). Computational Study of Axial Fatigue for Peripheral Nitinol Stents. *Journal of Materials Engineering and Performance*, 23(7):2606-2613.

Dordoni, E., **Meoli, A.**, Wu, W., Dubini, G., Pennati, G., Migliavacca, F., and Petrini, P., (2014). Fatigue behaviour of Nitinol peripheral stents: The role of plaque shape studied with computational structural analyses. *Medical Engineering and Physics*, 36(7):842-849.

Meoli, A., Dordoni, E., Petrini, P., Migliavacca, F., Dubini, G., and Pennati, G., (2013). Computational modelling of in vitro set-ups for peripheral self-expanding nitinol stents: the importance of stent-wall interaction in the assessment of the fatigue resistance. *Cardiovascular Engineering and Technology*, 4(4):474-484.

Petrini, P., Wu, W., Dordoni, E., **Meoli, A.**, Migliavacca, F. and Pennati, G., (2012). Fatigue behavior characterization of nitinol for peripheral stents. *Functional Materials Letters*, 5(1):125-129.

Proceedings

Migliavacca, F., **Meoli, A.**, Dordoni, E., Wu, W., Rochette, M., Petiot, F., Dubini, G., Petrini, L., and Pennati, G. (2013). Does the Plaque Geometry Influence the Fatigue Performance of Nitinol Peripheral Stents? - A Finite Element Study. *Proceedings of the International Conference on Shape Memory and Superelastic Technologies, SMST-2013*, Prague, Czech Republic, May 21st-24th, 2013.

Pennati, G., Dordoni, E., **Meoli, A.**, Wu, W., Rochette, M., Petiot, F., Petrini, L., Migliavacca, F., and Dubini, G. (2013). Computational Modelling of Fatigue Behaviour of Nitinol Peripheral Stents During in Vitro Tests. *Proceedings of the International Conference on Shape Memory and Superelastic Technologies, SMST-2013*, Prague, Czech Republic, May 21st-24th, 2013.

Petrini, L., Wu, W., Dordoni, E., **Meoli, A.**, Guala, C., Silvestro, C., Migliavacca, F., and Pennati, G. (2013). Development of an Ad Hoc Procedure for Nitinol Fatigue Characterization for Peripheral Stents. *Proceedings of the International Conference on Shape Memory and Superelastic Technologies, SMST-2013*, Prague, Czech Republic, May 21st-24th, 2013.

Dordoni, E., **Meoli, A.**, Wu, W., Dubini, G., Petrini, L., Pennati, G., and Migliavacca, F. (2013). Computer models of stented femoro-popliteal segment during knee-joint flexion. *Proceedings of the 8th European Symposium on Vascular Biomaterials, ESVB 2013*, Strasburg, France, May 10th-11th, 2013.

Dordoni, E., **Meoli, A.**, Wu, W., Petrini, L., Silvestro, C., Guala, C., Dubini, G., Migliavacca, F., and Pennati, G., (2013). A validated peripheral stent modeling to investigate the risk of fatigue fracture. *Proceedings of the 8th European Symposium on Vascular Biomaterials, ESVB 2013*, Strasburg, France, May 10th-11th, 2013.

Meoli, A., Petrini, L., Dordoni, E., Wu, W., Migliavacca, F., Dubini, G., and Pennati, G., (2012). Computational modeling of fatigue behavior of Nitinol peripheral stents during in vitro tests. *Proceedings of the10th International Symposium on Computational Methods in Biomechanics and Biomedical Engineering, CMBBE 2012*, Berlin, Germany, April 7th-11th, 2012.

Dordoni, E., Petrini, L., **Meoli, A.**, Wu, W., Migliavacca, F., Dubini, G., and Pennati, G., (2012). Finite element analyses of in vivo fatigue behavior: effect o f plaque features. *Proceedings of the10th International Symposium on Computational Methods in Biomechanics and Biomedical Engineering, CMBBE 2012*, Berlin, Germany, April 7th-11th, 2012.